

UC Riverside

UC Riverside Electronic Theses and Dissertations

Title

Optical Tuning and Application of Plasmonic Nanomaterials

Permalink

<https://escholarship.org/uc/item/6269j6x9>

Author

Yang, Fan

Publication Date

2021

Peer reviewed|Thesis/dissertation

UNIVERSITY OF CALIFORNIA
RIVERSIDE

Optical Tuning and Application of Plasmonic Nanomaterials

A Dissertation submitted in partial satisfaction
of the requirements for the degree of

Doctor of Philosophy

in

Chemistry

by

Fan Yang

March 2021

Dissertation Committee:

Dr. Yadong Yin, Chairperson

Dr. Pingyun Feng

Dr. Francisco Zaera

Copyright by
Fan Yang
2021

The Dissertation of Fan Yang is approved:

Committee Chairperson

University of California, Riverside

Acknowledgments

I would like to express my most profound gratitude to my advisor, Prof. Yadong Yin, for his academic advice and direction. I am grateful to him, and I appreciate the opportunity to work under his guidance. His insightful and knowledgeable guidance helps me explore the mystery of nanoworld, and his wise and enlightened insight helps me understand the real big world better.

I am also very thankful to my other committee members, Prof. Pingyun Feng and Prof. Francisco Zaera, for their time spent in my final defense and valuable comments on my dissertation.

The text of this dissertation, in part, is a reprint of the material as it appears in *Self-Aligned Anisotropic Plasmonic Nanostructures*, 2019. The coauthor Ji Feng helped develop the synthesis protocols which forms the basis for this dissertation.

I would like to thank my project collaborators: Dr. Jinxing Chen, Dr. Ji Feng, Dr. Zhiwei Li, Dr. Dawei Ding, Zuyang Ye. I learned a lot from them. I am much indebted to many past and current members of Yin group for providing a rich working experience, intellectual stimulation, and friendship: Dr. Rashed Aleisa, Dr. Yaocai Bai, Dr. Wenjing Xu, Dr. Xiaojing Wang, Qingsong Fan, Chaolumeng Wu, Chen Chen, Zepeng Cai, Dr. Shichuan Li, Dr. Yun Liu, Dr. Chunyu Zhou, Dr. Qianqian Fu, Dr. Aiqin Gao, Dr. Panpan Xu, Dr. Shuai Zhou, Dr. Lan Peng, Dr. Wenwen Yin, Dr. Bo Li, Dr. Xiaojun Zeng, Dr. Zhouhui Xia, Dr. Zhenyuan Liu *et al.* I would also like to thank the undergraduate and high school students who have worked and are working with me right now: Melinda Marin, Da Hae Jung, Yiyeon Lim, and Luis Aguilar. I thank Dr. Krassimir N. Bozhilov, Dr. Mathias

Rommelfanger, Dr. Michael Pigeon, Dr. Matthew Dickson, and Dr. Ilkuen Lee for assistance in using facilities in CFAMM; Dr. Dan Borchardt for assistance in using optical facilities in the Chemistry department. I also would like to thank Dr. Kevin Simpson for his help and guidance during my teaching.

I am incredibly grateful to my family for their support and understanding, which make this thesis possible. My thanks also go to my friends Dr. Tianyi Yu, Dr. Yangyang Wang, Yue Jin, and Fan Pu, for their valuable help.

ABSTRACT OF THE DISSERTATION

Optical Tuning and Application of Plasmonic Nanomaterials

by

Fan Yang

Doctor of Philosophy, Graduate Program in Chemistry

University of California, Riverside, March 2021

Dr. Yadong Yin, Chairperson

Plasmonic nanostructures have attracted significant attention due to their tunable optical properties and broad applications in chemical sensing, photothermal therapy, and energy conversions. The plasmonic properties of the nanoparticles are sensitive to the size, morphology, and composition of the metal nanoparticles. Although the wet chemistry synthesis of plasmonic nanoparticles with well-controlled geometries has been widely studied, the systematic tuning of novel plasmonic nanostructures can broaden the application scenarios. It brings more complexity to the optical responses of the plasmonic nanostructures. Besides, the synthesis of these novel structures deepens our understanding of the crystal growth mechanisms and light-matter interaction. In this dissertation, we discuss the tuning of optical properties of plasmonic nanoparticles through morphology control, magnetic manipulation, and exploring unconventional materials for the plasmonic solar-energy conversion.

In the aspect of morphology control, we achieved island growth of Au on Au nanostructures by introducing lattice mismatch through a thin layer of Pd coating on the substrate. The location of the islands can be controlled by changing the distribution of Pd, and the island features including size, distance and wetting degree of the islands can be systematically controlled.

In the aspect of the dynamic orientational control of anisotropic nanoparticles, plasmonic/magnetic nanocomposites were fabricated, and the magnetic tuning of the nanoparticles were achieved. In this dissertation, we broke the connection between the morphology of the plasmonic and the magnetic component, which was a major challenge in the synthesis of plasmonic/magnetic nanocomposites since it limited the choice of both plasmonic and magnetic components.

Furthermore, alternative plasmonic metals were explored, and we demonstrated the potential and advantages of Ni in the solar steam generation performance. A high energy conversion efficiency was achieved by combining the plasmonic property of Ni and broadband absorption of C. The magnetic response of Ni enabled the bottom-up fabrication of microstructures, further improving the solar steam generation performance of the device.

Table of Contents

Acknowledgments	iv
ABSTRACT OF THE DISSERTATION	vi
Table of Contents	viii
List of Figures	xiii
Chapter 1 Introduction	1
1.1 Plasmonic Nanoparticles	1
1.2 Optical Tuning via Morphology Control	3
1.2.1 Optical Tuning of Isotropic Plasmonic Nanoparticles	6
1.2.2 Optical Tuning of Anisotropic Plasmonic Nanoparticles	10
1.2.3 Introduction of “Hot Spots” Through Island Growth	14
1.3 Magnetic Tuning of Plasmonic Nanoparticles	19
1.4 Non-Noble Metal Plasmonic Nanoparticles	25
1.5 Focus of This Dissertation	30
1.6 Reference	32
Chapter 2 Site-Selective Island Growth on Au Nanoparticles	36
2.1 Introduction	36
2.2 Experimental	38
2.2.1 Chemicals	38

2.2.2 Synthesis of Au nanorods (AuNRs).....	39
2.2.3 Synthesis of Au Nanoplates (AuPLTs).....	39
2.2.4 Synthesis of Au Nanocubes (AuCBs) and Rhombic Dodecahedrons (AuRDs)	40
2.2.5 Synthesis of Au@Pd nanorods (Au@PdNRs).....	40
2.2.6 Ligand Exchange of Au@PdNRs	41
2.2.7 Island Growth on Au@PdNRs.....	42
2.2.8 Characterization	42
2.3 Results and Discussion	42
2.3.1 Controlling the Island Growth Modes on Au Nanorods by Changing Surface Strain Profiles.....	42
2.3.2 Tuning of the Structural Features of Islands.....	53
2.3.3 Site-Selective Island Growth on Other Au Nanostructures	65
2.4 Conclusion	70
2.5 Reference	71
Chapter 3 Magnetic Tuning of Plasmonic Nanoparticles.....	73
3.1 Magnetic Tuning of Au-Au/Au-Ag Dimers	73
3.1.1 Introduction.....	73
3.1.2 Experimental	75

3.1.2.1 Chemicals.....	75
3.1.2.2 Synthesis of Fe ₃ O ₄ @SiO ₂ Nanorods.....	75
3.1.2.3 Synthesis of Fe ₃ O ₄ @SiO ₂ /Au@SiO ₂ Nanocomposites	76
3.1.2.4 Synthesis of Fe ₃ O ₄ @SiO ₂ /Au-Au Nanocomposites	77
3.1.2.5 Synthesis of Fe ₃ O ₄ @SiO ₂ /Au-Au Nanocomposites	78
3.1.2.6 Fabrication of Anticounterfeiting Films	78
3.1.2.7 Characterizations.....	78
3.1.3 Results and Conclusion.....	79
3.1.4 Conclusion	95
3.2 Synthesis and Magnetic Manipulation of Au@Fe ₃ O ₄ and Ag@Fe ₃ O ₄ Nanostructures	95
3.2.1 Introduction.....	95
3.2.2 Experimental	96
3.2.2.1 Chemicals.....	96
3.2.2.2 Synthesis of Au Nanoparticles (AuNPs).....	97
3.2.2.3 Synthesis of Ag Nanowires (AgNWs).....	97
3.2.2.4 Synthesis of Ag Nanoplates (AgPLTs).....	97
3.2.2.5 Synthesis of Plasmonic@Fe ₃ O ₄ Core-Shell Nanoparticles	98
3.2.2.8 Characterization	99

3.2.3 Results and Conclusion.....	99
3.2.4 Conclusion	111
3.3 Reference	112
Chapter 4 Non-Noble Metal Magneto-Plasmonic Nanoparticles For Solar Steam Generation.....	114
4.1 Introduction.....	114
4.2 Experimental.....	116
4.2.1 Chemicals.....	116
4.2.2 Synthesis of Ni Nanoparticles (NiNPs)	116
4.2.3 Synthesis of Ni@C@SiO ₂ NPs.....	116
4.2.4 Synthesis of Ni@SiO ₂ NPs.....	117
4.2.5 Synthesis of C@SiO ₂ NPs	118
4.2.6 Fabrication of Ni@C@SiO ₂ /PVA Composite Film	118
4.2.7 Solar Steam Generation Measurement.....	118
4.2.8 Characterization	119
4.2.9 Calculation of Energy Loss.....	119
4.2.10 Calculation of Photothermal Efficiency of Nanoparticles in Solution	120
4.2.11 Calculation of Equivalent Vaporization Enthalpy	125
4.3 Results and Conclusion.....	126

4.3.1 Synthesis of Ni@C@SiO ₂ NPs and the Optimization of the Photothermal Performance	126
4.3.2 Enhancing the Solar Steam Generation Performance with Magnetically Actuated Microstructures.....	148
4.4 Conclusion	160
4.5 Reference	161
Chapter 5 Conclusion and Outlook.....	164
5.1 Conclusion of this Dissertation.....	164
5.2 Outlook and Future Work.....	167

List of Figures

- Figure 1.1 Schematics showing the three stages of crystal growth. Reproduced with permission from ref 15. Copyright © 1952, American Chemical Society. 5
- Figure 1.2 (a) Schematic of plasmon oscillation for a sphere, showing the displacement of the conduction electron charge cloud relative to the nuclei. Adapted with permission from ref. 4. Copyright © Royal Society of Chemistry 2015 (b) Simulated absorption, scattering, and extinction cross-sections of Au nanoparticles with different sizes. (c) Intensity plot of absorption efficiency as a function of diameter and wavelength for Au nanoparticles in water. (d) Dependence of the absorption efficiency of Au nanoparticles as a function of their radius. 8
- Figure 1.3 (a) Schematics showing the transverse (top) and longitudinal (bottom) plasmon resonance modes. (b) Simulated spectra of AuNRs with different aspect ratio with fixed particle volume. (c) The longitudinal LSPR peak position as a function of the aspect ratio of the nanorods..... 11
- Figure 1.4 Schematics showing the symmetry break induced by the UPD of Ag. Adapted with permission of ref 40. Copyright © 2017 American Chemical Society..... 13
- Figure 1.5 (a) Schematics showing tuning of growth modes by tuning relationship between the deposition rate and the diffusion rate. (b) Overgrowth of Pd on Pd nanocubes with different precursor injection rates. Adapted with permission of ref 16. Copyright 2013 National Academy of Sciences 16
- Figure 1.6 Schematic illustration of three different growth modes. Adapted with permission of ref 51. Copyright © 2008 Elsevier Ltd..... 18
- Figure 1.7 Schematics showing the magnetic response to external magnetic fields. 21
- Figure 1.8 (a) Simulated spectra of Au nanorods with incident light polarization aligned with the longitudinal and transverse axis of the nanorods. (b) TEM image showing the parallel attachment of AuNRs and Fe₃O₄@SiO₂ nanorods. (c) UV-vis spectra of the nanocomposite with different magnetic field directions. Adapted with permission of ref 57. 24
- Figure 1.9 Simulated extinction cross-section of metallic nanoparticles of 20 nm size in water..... 27
- Figure 1.10 (a) Joule numbers of Au, TiN, and ZrN. (b) Optical image and dielectric functions of metal nitride. Adapted with permission of Ref 63 Copyright © 2013 WILEY-VCH Verlag GmbH & Co. KGaA, Weinheim. 29

Figure 2.1 (a) Schematics showing the island growth modes on AuNRs controlled by anisotropic modification of PEGSH and selective deposition of Pd. (b) UV-vis spectra of AuNRs and Au@PdNRs with different PEGSH/Au ratios. (c) Simulated spectra of AuNRs and Au@PdNRs with different coverage of Pd. 45

Figure 2.2 (a) FTIR spectra of CTAB, TSC, and Au@PdNRs before and after ligand exchange. (b) Zeta potential of the CTAB-stabilized Au@PdNRs before ligand exchanged and after ligand exchanged with DEA and TSC. (c) UV-vis-NIR spectra of the overgrown Au@PdNRs. (d-f) TEM images of island growth on (d) Au@Pd₀PEGSHNRs, (e) Au@Pd_{0.01}PEGSHNRs, and (d) Au@Pd_{0.1}PEGSHNRs. The scale bars are 50 nm. 48

Figure 2.3 TEM images of island growth on Au@PdNRs using AuNRs modified with (a) cysteine, (b) mercaptoacetic acid, and (c) PEGNH₂. The scale bars are 50 nm. 50

Figure 2.4 TEM images of small islands grown on (a) Au@PEGSHNRs and (c) Au@Pd₀PEGSHNRs. Statistic analysis of the contact angle of the small islands grown on (b) Au@PEGSHNRs and (d) Au@Pd₀PEGSHNRs. 52

Figure 2.5 TEM images of island growth on Au@Pd₀PEGSHNRs with KI/HAuCl₄ ratio of (a) 10 and (b) 40 and on Au@Pd_{0.1}PEGSHNRs with KI/HAuCl₄ ratio of (c-d) 0, (e) 10 and (f) 40. Scale bars in (a-c) and (e-f) are 50 nm. Scale bar in (d) is 20 nm. 55

Figure 2.6 (a-d) TEM images of AuDBs synthesized with (a) 20 μL, (d) 40 μL, (c) 60 μL and (d) 80 μL of growth solution. Scale bars are 50 nm. (e) UV-vis-NIR spectra of AuDBs synthesized with different amounts of growth solution added. (f) Evolution of the size of islands and the longitudinal LSPR peak wavelength with respect to growth solution amount. 57

Figure 2.7 (a-d) TEM images of AuDBs synthesized with PEGSH/Au ratio of (a) 0.05, (b) 0.1, (c) 0.2 and (d) 0.3. Scale bars are 50 nm. (e) UV-vis-NIR spectra of AuDBs synthesized with different PEGSH/Au ratios. (f) Evolution of distance between islands, *d*, overall length, *l*, and the wavelength of longitudinal peaks with respect to PEGSH/Au ratio. Simulated results of (g) spectra and (h-k) electric field distribution of AuDBs with *d* ranging from 20 nm to 32 nm at their resonance wavelengths. 59

Figure 2.8 (a-d) TEM images of AuDBs synthesized with presence of (a) 0%, (b) 0.01%, (c) 0.1% and (d) 2.5% PVP. Scale bars are 50 nm. Insets are magnified images at the connection of the island and nanorods. Scale bars in insets are 20 nm. (e) UV-vis-NIR spectra of AuDBs synthesized with different PVP concentration. Simulated results of (f) spectra of AuDBs with curvature radius at the connection of 2, 10, and 18 nm, and electric field distribution of AuDBs with a curvature radius of (g) 2 nm and (h) 18 nm at their resonance wavelength. 62

Figure 2.9 (a-f) TEM images of Au seeds (a) before aging and after aging with presence of (b) 0%, (c) 0.001%, (d) 0.01%, (e) 0.1% and (f) 1% PVP for 1 h. (g) Size distribution and

(h) UV-vis spectra of Au seeds before and after aging with different PVP concentration.	63
Figure 2.10 Systematic tuning of LSPR peak of AuDBs at different tuning scales through the control of island size, distance, and wetting degree.....	64
Figure 2.11 (a) Schematics showing the tuning of island growth on the faces and the tips of AuCBs. TEM image of island growth on (b) the faces and (c) the tips of AuCBs, the dashed lines indicated the edges of the nanocubes.	66
Figure 2.12 (a) Schematics showing the Au@Pd seeds used for island growth. TEM images of island growth on (b-d) AuPLTs, (f-h) AuCBs and (j-l) AuRDs with KI/HAuCl ₄ ratio of (b, f, j) 5, (c, g, k) 10 and (d, h, l) 40. Scale bars are 50 nm. Insets in (f-h) and (j-l) are 3D models of corresponding particles. Statistic analysis of numbers of islands grown on (e) AuPLTs, (i) AuCBs, and (m) AuRDs with different KI/HAuCl ₄ ratio.	68
Figure 2.13 SEM images of overgrown Au@PdRDs. Scale bars are 100 nm.....	69
Figure 3.1 Schematics showing (a) the growth of self-aligned Au-Au dimers through partial surface passivation and (b) the control of overlapping degree with SiO ₂ coating thickness.	80
Figure 3.2 (a) Schematics showing the synthesis of Fe ₃ O ₄ @SiO ₂ /Au-Au nanocomposites with Au-Au dimers aligned perpendicular to the Fe ₃ O ₄ @SiO ₂ nanorods. (b-d) TEM images of (b) FeOOH nanorods, (c) Fe ₃ O ₄ @SiO ₂ /Au@SiO ₂ , and (d) Fe ₃ O ₄ @SiO ₂ /Au-Au nanocomposites. Scale bar in (b) is 1 μm. Scale bars in (c) and (d) are 50 nm. (e) UV-vis spectra of Fe ₃ O ₄ @SiO ₂ /Au@SiO ₂ and Fe ₃ O ₄ @SiO ₂ /Au-Au nanocomposites.	82
Figure 3.3 (a) Schematics showing the magnetic tuning of nanocomposites. (b-e) UV-vis spectra of (b-c) nanocomposites and (d-e) Fe ₃ O ₄ @SiO ₂ nanorods under z-polarized light with magnetic field changing in (b, d) xz plane and (c, e) xy plane. Insets in (b) and (c) are the digital images of the solutions. (f) UV-vis spectra of nanocomposites synthesized with 400-nm Fe ₃ O ₄ nanorods under different magnetic field directions.	86
Figure 3.4 TEM image of (a) Fe ₃ O ₄ @SiO ₂ /Au-Ag and (b) nanocomposites coated with another layer of SiO ₂ . UV-vis spectra of Fe ₃ O ₄ @SiO ₂ /Au-Ag under (c) unpolarized light and (d) z-polarized light.....	88
Figure 3.5 (a) Schematics showing the fabrication of the nanocomposite/solvogel film with different alignment in the two regions. (b-i) Polarized optical microscope image of solvogel films with (b-e) Fe ₃ O ₄ @SiO ₂ /Au-Au and (f-i) Fe ₃ O ₄ @SiO ₂ /Au-Ag nanocomposites with nanocomposite alignment indicated at the top of the images and polarization of incident light indicated at the bottom of the images. Scale bars are 200 μm.	91

Figure 3.6 (a) Schematics showing the alignment of nanocomposites in different regions. (b-g) Optical images of solvigel films with (b-d) $\text{Fe}_3\text{O}_4@\text{SiO}_2/\text{Au-Au}$ and (e-g) $\text{Fe}_3\text{O}_4@\text{SiO}_2/\text{Au-Ag}$ nanocomposites under (b, e) unpolarized light, (c, f) x-polarized and (d, g) y-polarized light. Scale bars are 1.5 mm. 93

Figure 3.7 TEM images of $\text{Au}@\text{Fe}_3\text{O}_4$ core-shell composites synthesized with AuNPs aged in growth solution for (a) 2h, (b) 0 min, (c) 30 min, and (d) 1 h after synthesis, and (e) AuNPs bubbled with air for 1h. Scale bars are 50 nm. (f) Digital image showing the magnetic separation of the nanocomposites. 101

Figure 3.8 TEM images of $\text{Au}@\text{Fe}_3\text{O}_4$ synthesized at various conditions. The volume of 2.5 M NaOH/DEG solution in (a), (b) and (c) were 1.5 mL, 1.75 mL and 2.7 mL, respectively. The amount of PAA added in the system in (d), (b), and (e) were 2 mmol, 4 mmol, and 8 mmol, respectively. A mixture of 4 mmol PAA and 4 mmol PAASS were added in (f) during synthesis. Scale bars are 20 nm. 104

Figure 3.9 TEM images of $\text{Au}@\text{Fe}_3\text{O}_4$ core-shell particles synthesized with different (a-d) AuNPs concentration and (f-j) AuNPs sizes. The final concentration of AuNPs in (a), (b), (c) and (d) were 15 μM , 7.5 μM , 3.75 μM and 1.88 μM , respectively. The AuNPs sizes in (f), (g), (h), and (i) were 20 nm, 33 nm, 45 nm and 70 nm, respectively. Scale bars are 100 nm. (e) The evolution of radius³ with respect to 1/mol(Au). (i) UV-vis spectra with $\text{Au}@\text{Fe}_3\text{O}_4$ synthesized with different AuNPs sizes..... 107

Figure 3.10 TEM images of (a) $\text{Ag}@\text{Fe}_3\text{O}_4\text{NWs}$ and (b) $\text{Ag}@\text{Fe}_3\text{O}_4\text{PLTs}$. (c) Schematics showing the magnetic tuning and the cross-section difference of $\text{Ag}@\text{Fe}_3\text{O}_4\text{PLTs}$. (d) UV-vis spectra of $\text{Ag}@\text{Fe}_3\text{O}_4\text{PLTs}$ with a magnetic field applied parallel and perpendicular to the incident light propagation direction. Digital images of (e) smart window above a letter “Y”, with a magnetic field applied in (top) out-of-plane and (bottom) horizontal direction and smart display device with a magnetic field applied (f) parallel and (g) perpendicular to incident light. 110

Figure 4.1 Linear time date vs. $-\ln(\theta)$ obtained from the cooling period of Ni40C20.... 124

Figure 4.2 (a) Synthetic scheme of $\text{Ni}@\text{C}@\text{SiO}_2$ core-shell nanoparticles and (b-f) corresponding TEM images of the particles at each stage. (g) HADDF-STEM image and (h) EDX elemental mapping of $\text{Ni}@\text{RF}@\text{SiO}_2$ core-shell nanoparticles. Scale bars are 100 nm. 128

Figure 4.3 XRD pattern of $\text{Ni}@\text{RF}$, $\text{Ni}@\text{RF}@\text{SiO}_2$ and $\text{Ni}@\text{C}@\text{SiO}_2$ 129

Figure 4.4 TEM of $\text{Ni}@\text{RF}$ nanoparticles treated with excessive KMnO_4 130

Figure 4.5 TEM of $\text{Ni}@\text{RF}@\text{SiO}_2$ nanoparticles without KMnO_4 treatment. 131

Figure 4.6 (a, c) Simulated spectra of Ni@C core-shell particles with (a) varying shell thickness and (c) core size, normalized by the number of moles of the substance. (b, d) Cross-section area and absorption ratio of particles corresponding to (a) and (c). (e) Extinction spectra of prepared samples with various Ni core size and carbon thickness in comparison to solar irradiation spectrum.....	134
Figure 4.7 TEM images of (a) Ni40, (b) Ni40C40, (c) Ni20C20, and (d) C80 nanoparticles. Scale bars are all 100 nm.	135
Figure 4.8 Reflectance spectra of the prepared samples.....	136
Figure 4.9 (a) Temperature change over time when different films were subjected to the illumination of the solar simulator. (b) Temperature variation over time of the nanostructure dispersion (1 $\mu\text{g/mL}$) in response to light irradiation. The light was turned off after 75 min of irradiation. (c) Maximum temperature elevation at equilibrium and photothermal efficiency of the prepared nanoparticles.....	139
Figure 4.10 (a) Schematic illustration of the solar steam generation process. (b) Digital photo of the solar evaporator. (c) Side and top view of IR thermal images of water beakers recorded by a thermal camera after being irradiated with a solar simulator for 15 min. (d) Time course of water evaporation performance with different samples. (e) Steam generation rate and efficiency of different samples.....	141
Figure 4.11 TEM image of Ni40C20 after 6 cycles of steam generation.	143
Figure 4.12 (a) Cycling performance of Ni40C20. (b) Steam generation performance of Ni40C20 with or without SiO ₂ shell. (c) Change of surface temperature of Ni40C20 with or without SiO ₂ shell.....	144
Figure 4.13 (a) Cycling performance of Ni40C20 in artificial seawater. (b) Steam generation performance of Ni40C20 in seawater under continuous solar illumination.	145
Figure 4.14 TEM image of Ni40C20 sample after 8 h of steam generation test in artificial seawater.....	146
Figure 4.15 Water contact angle of Ni40C20 (a) with and (b) without SiO ₂ layer.	147
Figure 4.16 Room temperature hysteresis loop of Ni40C20. Inset is the optical image showing the magnetic collection of Ni40C20, all particles will be attracted to one side within 10 s.....	149
Figure 4.18 SEM images of PVA/Ni40C20 composite film (a) without magnetic field, with (b) 100 mT, (c) 200 mT, and (d) 400mT magnetic field applied during gelation process.	152

Figure 4.19 (a) Evaporation rate of water and PVA hydrogel with different PVA content. (b) Equivalent vaporization enthalpy of water in bulk water and prepared PVA hydrogels.	154
Figure 4.20 Dependence of steam generation performance on the loading density of Ni40C20.....	155
Figure 4.21 Schematic illustration of the light reflection and active surface area difference of a rough surface and a smooth surface.....	158
Figure 4.22 Reflectance spectra of M-40 composite film and directly deposited Ni40C20 nanoparticles.	159

Chapter 1 Introduction

1.1 Plasmonic Nanoparticles

Surface plasmon resonance (SPR) is a physical phenomenon that describes the resonant oscillation of the electron cloud in metal with the incident electromagnetic field. The surface plasmon is a quasiparticle arising from the quantization of the coherent delocalized electron oscillations that exist at the surface of materials (typically metals) with a negative real part of their dielectric functions. Depending on the dielectric function of the material, the surface plasmon has an intrinsic oscillation frequency. When the frequency of the incident electromagnetic wave matches the surface plasmons' intrinsic frequency, the resonance of the surface plasmons and the incident wave will significantly enhance the amplitude of the near field around the particle surface. Typically, the SPR takes place in two forms, the surface plasmon polariton (SPP) and the localized surface plasmon resonance (LSPR). The LSPR phenomenon happens when the particle size is smaller or comparable to the wavelengths of the incident electromagnetic wave. The surface plasmon will be firmly bound on the surface of the particles, and the absorption and scattering of the incident field are greatly enhanced. The utilization of the LSPR phenomenon can date back to the 4th century, the Au and Ag were incorporated in glass for coloration. The Lycurgus cup is a well-known example of the utilization of the plasmonic phenomenon. The color of the cup can shift from red to green when the light source was moved from inside to the outside of the cup due to the Au nanoparticles incorporated in the glass. The Au nanoparticles have strong plasmonic resonance at 520 nm; therefore, depending on whether the light received is dominated by transmission or scattering, the color interpreted

by the viewers will switch between red and green. Despite the early utilization of plasmonic nanoparticles, this phenomenon only started to get noticed until the 19th century, when Faraday first prepared the pure colloidal Au suspension by reducing Au chloride solution with phosphorous and concluded that the red color originated from the small-sized particles.¹ With advances in both synthetic methods and theoretical studies in the optical properties, plasmonic nanoparticles quickly gained increasing interest due to the potential applications in sensing, biotherapies, and catalysis.²⁻⁵

The spectra of the plasmonic nanoparticles can be calculated by solving Maxwell equations. In the cases of nanoparticles with a size much smaller than the wavelength of the incident light, the electric field can be taken as constant. Under this quasistatic approximation, the Mie theory provides a description of the extinction cross-section (σ_{ext}) of the nanoparticles:⁶

$$\sigma_{ext} = \frac{24\pi^2 r^3}{\lambda} \epsilon_m^{3/2} \left[\frac{\epsilon_2}{(\epsilon_1 + 2\epsilon_m)^2 + \epsilon_2^2} \right] \quad (1.1)$$

where r is the radius of the nanoparticle, λ is the wavelength of light, ϵ_m is the dielectric constant of the surrounding medium, ϵ is the dielectric function of the nanoparticle defined by $\epsilon = \epsilon_1 + i\epsilon_2$ (ϵ_1 and ϵ_2 indicate the real and imaginary parts of the dielectric constant, respectively). According to this equation, when ϵ_1 is close to $-2\epsilon_m$, σ_{ext} reaches the maximum, and λ_{max} can be estimated based on the dielectric function of the metal.

Additionally, Gans⁷ modified this equation to include the anisotropy of the nanoparticles, and the absorption (σ_{abs}) and scattering cross-section (σ_{sca}) of plasmonic nanoparticles can be quantified as follows:

$$\sigma_{abs} = \frac{2\pi}{3\lambda} \varepsilon_m^{3/2} V \sum_i \frac{\varepsilon_2 / (n^{(i)})^2}{(\varepsilon_1 + [(1-n^{(i)})/n^{(i)}] \varepsilon_m)^2 + \varepsilon_2^2} \quad (1.2)$$

$$\sigma_{sca} = \frac{8\pi^3}{9\lambda^4} \varepsilon_m^2 V^2 \sum_i \frac{((\varepsilon_1 - \varepsilon_m)^2 + \varepsilon_2^2) / (n^{(i)})^2}{(\varepsilon_1 + [(1-n^{(i)})/n^{(i)}] \varepsilon_m)^2 + \varepsilon_2^2} \quad (1.3)$$

$$\sigma_{ext} = \sigma_{sca} + \sigma_{abs} \quad (1.4)$$

where V is the unit volume of the nanoparticle, and $n^{(i)}$ is the depolarization factor, which can be further expressed as following:

$$n^{(a)} = \frac{1}{R^2 - 1} \left[\frac{R}{2\sqrt{R^2 - 1}} \ln \frac{R + \sqrt{R^2 - 1}}{R - \sqrt{R^2 - 1}} - 1 \right] \quad (1.5)$$

$$n^{(b)} = n^{(c)} = (1 - n^{(a)})/2 \quad (1.6)$$

where a, b, and c indicate geometric factors (i.e., the three axes) of the nanoparticle and R is the aspect ratio. From the equation, we can see the composition, size, and shape of the plasmonic nanoparticles and the surrounding environment greatly influence the optical properties. By changing these factors, the optical properties of a plasmonic nanoparticle can be tuned.

1.2 Optical Tuning via Morphology Control

As shown above, the LSPR wavelength and cross-sections were greatly influenced by the size and morphologies of the nanoparticles. Although the dynamic tuning of the plasmonic properties of nanocrystals through deformation of specific structural features are feasible and have been demonstrated by many studies,⁸⁻⁹ the morphology control of nanocrystals through synthetic approaches is the focus in this section. As proposed in La Mer's crystal growth model (Figure 1.1),¹⁰⁻¹¹ the growth of crystals can be divided into three stages. In Stage I, the precursor is reduced to atoms, and the concentration of metal

atoms increases to above the saturation concentration. Stage II represents the nucleation stage, where the concentration of metal atoms surpasses the nucleation threshold, the supersaturated atoms aggregate to form nuclei in the solution. When the concentration of metal atoms drops below the nucleation threshold, the crystal reaches the growth stage (Stage III), characterized by rapid increase in crystal size, and the concentration of metal atoms gradually decreases to the saturation concentration until the precursor is completely depleted. Depending on whether the nucleation stage is carried out simultaneously with the crystal growth stage or not, the synthetic strategies of plasmonic nanocrystals can be generally classified into two categories, seedless growth, and seed-mediated growth.

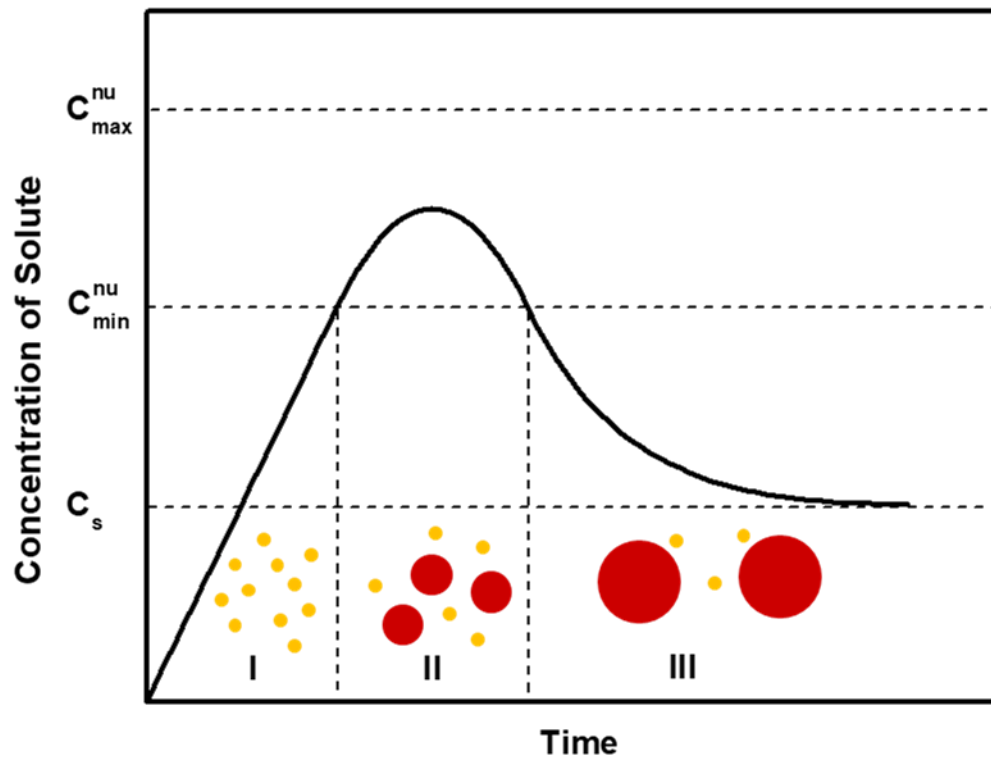


Figure 1.1 Schematics showing the three stages of crystal growth. Reproduced with permission from ref 15. Copyright © 1952, American Chemical Society.

In seedless growth methods, the growth of nanocrystals follows La Mer's model of crystal growth. In contrast, in seed-mediated growth schemes, the nanoparticle seeds are prepared separately and added into the growth solution later to initiate crystal growth. The seed solution is typically prepared by reducing the metal precursors with a strong reducing agent to increase the metal atom concentration beyond the nucleation threshold dramatically. The high concentration of metal atoms results in the predominance of nucleation in Stage II, and the metal atoms and precursors are quickly depleted, suppressing the following crystal growth stage. In the growth solution, on the other hand, the metal precursor is reduced under a mild reaction condition to keep the atom concentration between the saturation concentration and the nucleation threshold.¹² As a result, the seed-mediated growth method separates the Stage II and Stage III in La Mer's model. Thus it offers more uniform nanoparticles and more opportunities in the tuning of growth kinetics. In this section, the tuning of optical properties of plasmonic nanoparticles through synthetic strategies will be discussed in cases of isotropic, anisotropic, and complex nanoparticles. In each section, the factors that influence the optical properties will be discussed first, and the synthetic approaches to achieve the tuning of these features will be introduced.

1.2.1 Optical Tuning of Isotropic Plasmonic Nanoparticles

According to Equation 2, with spherical nanoparticles, which have an aspect ratio of 1, the optical properties are solely dependent on the size of the nanoparticles. As shown in Figure 1.2b, the extinction cross section increases dramatically with increasing particle sizes with increasing size. In the meantime, as shown in Equations 2 and 3, the absorption cross-section has a linear relationship with the volume of the particles. In contrast, the

scattering cross-section has a 2nd order relationship with the volume. This suggested that the ratio of scattering in the extinction spectrum of a particle will increase with increasing particle volume, as shown in Figure 1.2c and d. This gives us a basic guideline for the tailoring of the nanoparticles. In applications where a high absorption cross-section ratio is highly desired, such as photothermal conversion,¹³⁻¹⁴ the size of the particle should be reduced in order to obtain high photothermal efficiency. In scenarios where scattering is emphasized, for example, surface enhanced Raman spectroscopy (SERS), a more extensive feature will be preferred.

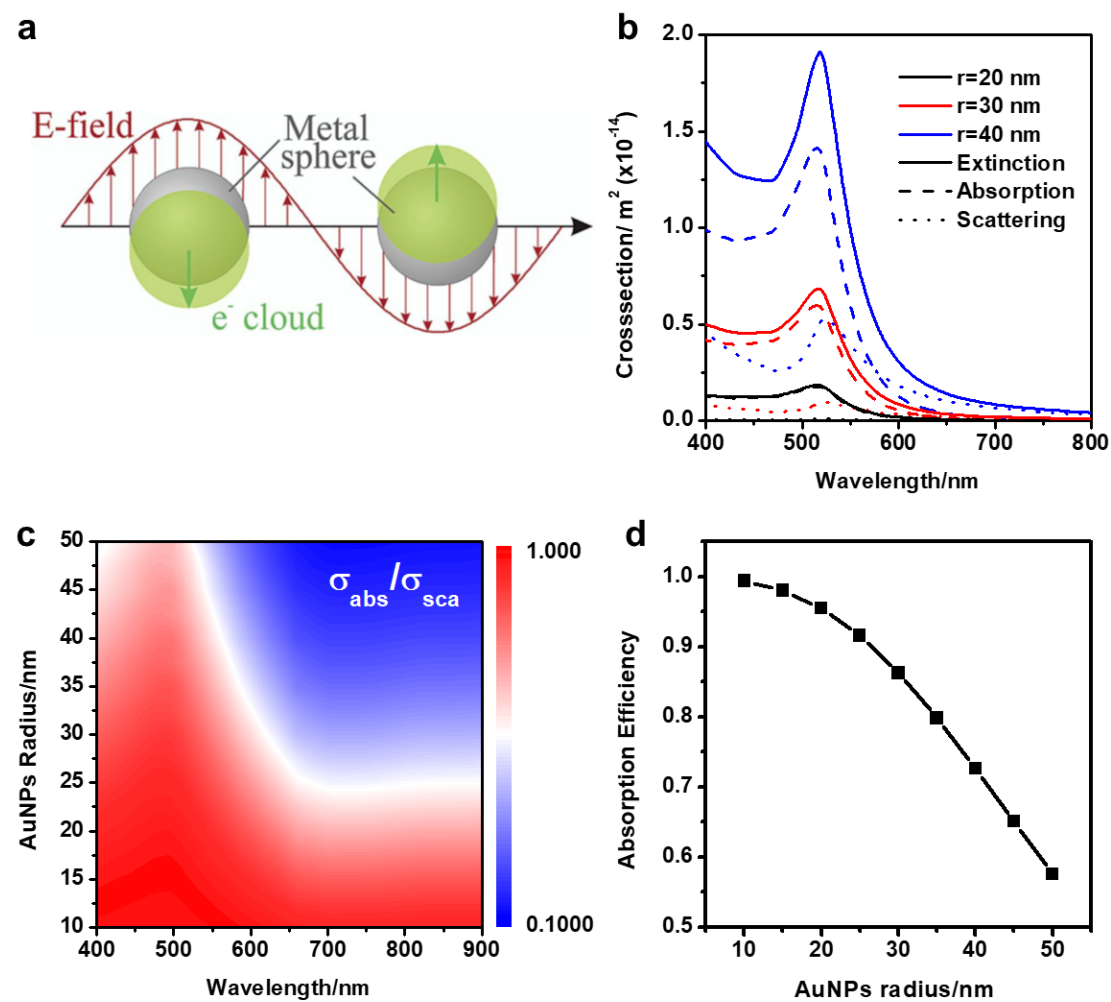


Figure 1.2 (a) Schematic of plasmon oscillation for a sphere, showing the displacement of the conduction electron charge cloud relative to the nuclei. Adapted with permission from ref. 4. Copyright © Royal Society of Chemistry 2015 (b) Simulated absorption, scattering, and extinction cross-sections of Au nanoparticles with different sizes. (c) Intensity plot of absorption efficiency as a function of diameter and wavelength for Au nanoparticles in water. (d) Dependence of the absorption efficiency of Au nanoparticles as a function of their radius.

Due to the limited amount of precursors, the total volume of the metal that can be produced is fixed; therefore, the tuning of particle size can be achieved by controlling the number of nuclei formed in Stage II. In seedless growth, the nucleation rate is determined by the concentration of the metal atoms. In the classic synthesis of citrate capped AuNPs,¹⁵⁻¹⁶ with high citrate concentration, the concentration of Au atoms increases rapidly and dramatically passes the nucleation threshold when the nucleation reaction occurs. In this case, the fast initial nucleation rate produces a larger number of nuclei, leading to smaller nanoparticles. When the citrate concentration is decreased, the nucleation starts at a concentration slightly above the threshold; therefore, the initial reaction rate will be significantly reduced, producing fewer nuclei and larger particles. In addition to the cross-section ratio change predicted by the Mie theory, the increase in particle size will also redshift the LSPR peak of the spherical nanoparticles.¹⁵ In sufficiently large particles, the appearance of a secondary peak is observed. This observation can be attributed to the quadrupole or higher-ordered modes of plasmonic resonance, which is neglected in the dipole approximation typically applied in Mie theories.¹⁷ In the seed-mediated methods, the particle size is controlled through the amount of seeds added to the growth solution. This makes nanoparticles' size predictable through numeric relationships between the total volume and numbers of particles, and the reproducibility is improved. Furthermore, due to the separation of the nucleation and crystal growth stages, the size of nanoparticles can be tuned in a larger range and avoid polydispersity caused by the nonsimultaneous formation of nuclei. As we previously reported,¹⁸ the seed-mediated growth method can produce quasi-spherical nanoparticles up to 100 nm in diameter. Γ is added in the growth solution

to form AuI_2^- complex and lower the reduction potential of the Au precursors to keep the concentration of Au atoms below the nucleation threshold.

1.2.2 Optical Tuning of Anisotropic Plasmonic Nanoparticles

According to Equations 2 and 3, the aspect ratio also has a great impact on the optical properties of the plasmonic nanoparticles. As shown in Figure 1.3a, the anisotropy of nanoparticles brings new dipole modes, allowing the appearance of a second LSPR peak, referred to as longitudinal mode, since it arises when the polarization of the incident light matches the longitudinal axis of the anisotropic nanoparticles. As plotted in Figure 1.3b, the longitudinal LSPR peak will redshift with increasing aspect ratio. The wide tunability of the LSPR wavelengths has inspired enormous research interests in the synthesis of anisotropic nanoparticles, especially nanorods, characterized by a sharp longitudinal peak within a wide spectral range. From Equation 2, an approximately linear relationship between the aspect ratio of nanorods and the maximum absorption wavelength can be derived, which can be described as $\lambda_{max} = (53.71R - 42.29) * \epsilon_m + 495.14$ regardless the radius of the nanorods.¹⁹⁻²⁰ (Figure 1.3c) This provided a convenient guideline for the design of nanorods. The above equations provided a general understanding of the optical properties of the plasmonic nanoparticles and their size and aspect ratio. However, these equations fail to represent more complicated morphologies and detailed features such as the sharpness of the tips. An accurate solution for the Maxwell equation is needed for the prediction of the optical properties of these complicated morphologies.²¹

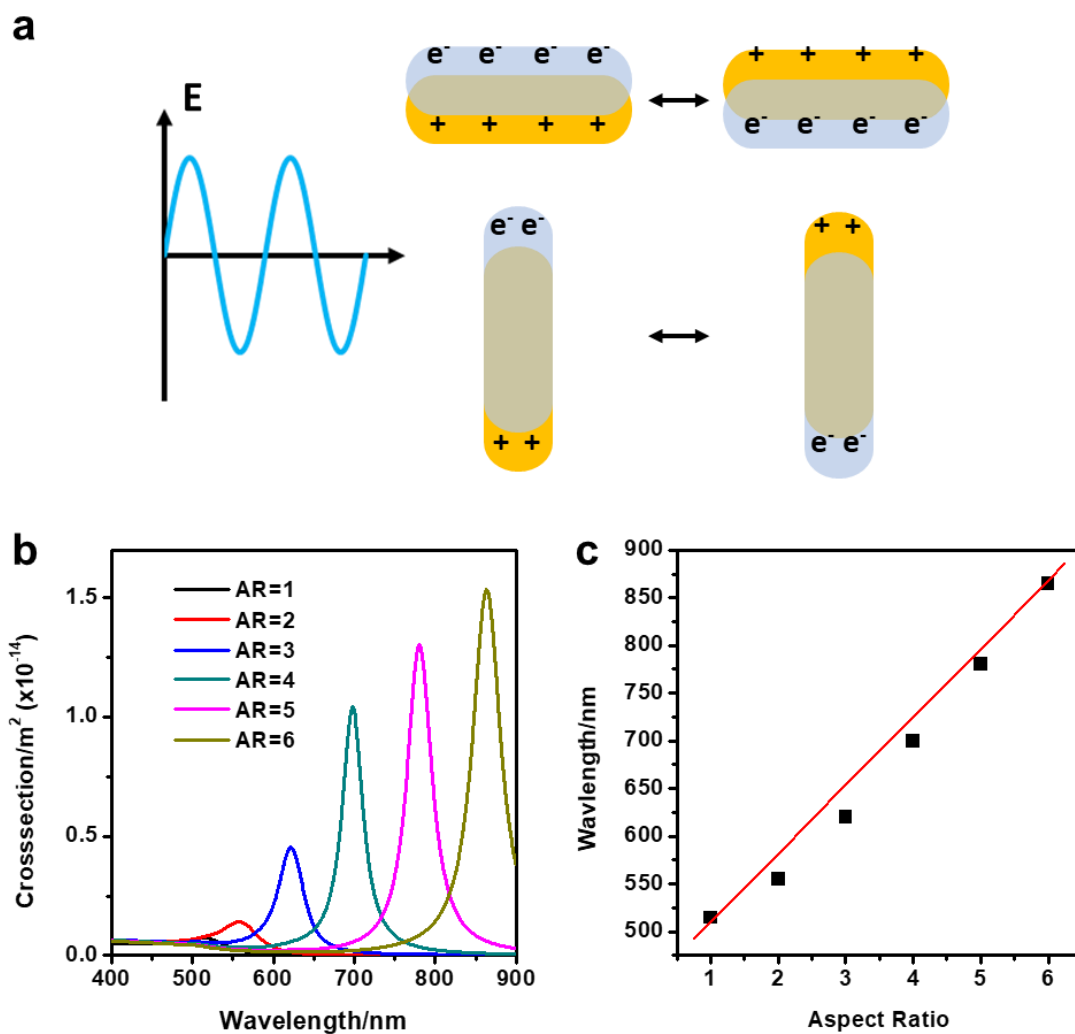


Figure 1.3 (a) Schematics showing the transverse (top) and longitudinal (bottom) plasmon resonance modes. (b) Simulated spectra of AuNRs with different aspect ratio with fixed particle volume. (c) The longitudinal LSPR peak position as a function of the aspect ratio of the nanorods.

The key to the synthesis of anisotropic nanoparticles is to break the symmetry of crystal growth. One strategy frequently used is to control the crystal growth kinetics. This strategy is highlighted in the synthesis of single-crystal Au nanorods using CTAB as a surfactant.²²⁻²³ The CTAB capped Au seeds are single-crystal cuboctahedral seeds enriched with {100} and {111} facets. CTAB selectively adsorbs on the {100} facets of the Au seeds, leading to the development of {100} facets and elimination of {111} facets.²⁴ Another key factor in the synthesis of the Au nanorods is the underpotential deposition (UPD) of Ag. As proposed in mechanism studies, the UPD of Ag plays an important role in the symmetry breaking of the crystal growth.²⁵ As shown in Figure 1.4, when the crystal size increases to beyond 4 nm, the {110} facets will start to develop to lower the energy of the edge atoms. The UPD of Ag preferentially happens on the newly grown {110} facets and passivate the growth of Au in this direction, therefore, breaking the symmetry of the crystal growth.

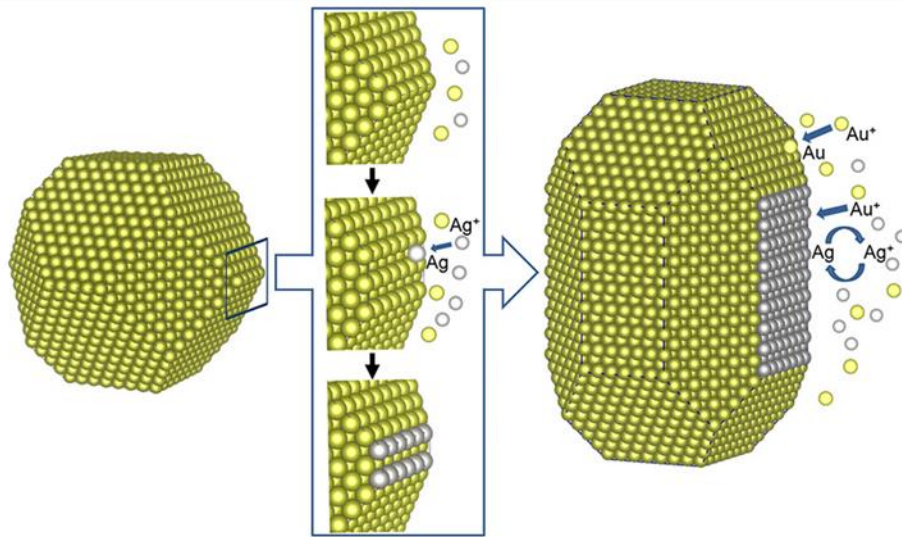


Figure 1.4 Schematics showing the symmetry break induced by the UPD of Ag. Adapted with permission of ref 40. Copyright © 2017 American Chemical Society

Another symmetry breaking strategy is to induce defects in seed crystals. For example, in another widely used method for the synthesis of Au nanorods, penta-twinned Au seeds are first synthesized in the presence of citrate ions.²⁶ The penta-twinned seeds are enclosed by {111} facets, which can be stabilized by citrate. The geometry of the penta-twinned seeds favors the crystal growth along the symmetry axis and prohibits lateral growth. In addition, the UPD of Ag preferentially happens on the newly grown {100} facets, further facilitating the uniaxial growth of Au nanorods.²⁷

1.2.3 Introduction of “Hot Spots” Through Island Growth

In addition to the spherical nanoparticles and anisotropic nanostructures such as nanorods and nanoplates, recent researches have shifted to the synthesis of more complex structures that may offer novel optical properties.²⁸⁻³¹ Seed mediated growth has proved to be a convenient method for the construction of these novel structures. The complex structures deviate from the quasi-static approximation applied in the Mie theory; therefore, the optical properties of these nanoparticles cannot be easily predicted with a simple equation. However, from empirical data and computational simulation obtained with accurately solved Maxwell equations, the structure-optical properties relationship can be gradually established.

An important feature that can be achieved through unconventional seed-mediated growth is the hot spots induced by sharp tips and concave edges. The synthesis of sharp edges also attracted interests in the synthesis point of view since sharp edges are not thermodynamically favored, and the formation of these structures can provide a deeper understanding of the growth kinetics of the plasmonic nanocrystals. Two typical strategies

were applied to induce the island growth on nanocrystals. As shown by Younan Xia *et al.*,¹² the island growth can be induced by controlling the ratio between deposition rate and diffusion rate of newly deposited metal atoms (Figure 1.5). During the crystal growth process, the atoms on the newly grown “islands” will diffuse onto the substrate surface to lower the surface energy, resulting in the decrease in the reduced aspect ratio of the “islands” and eventually the elimination of the sharp tips. By controlling the deposition rate, the overgrowth of nanocrystals can be tuned from island growth to thermodynamically favored products (Figure 1.5b). Our group has also reported the island growth on Au nanostructures by reducing the surface diffusion rate,²⁹ the island growth of Au on Au nanoplates can be induced by modification of PVP on the Au nanoplates. The PVP bound to the surface of Au nanoplates and reduced the surface diffusion of Au atoms from newly formed islands. As a result, the islands on the nanoplates produce abundant hot spots at the connection plane and greatly enhanced the SERS performance of the Au nanoplates.

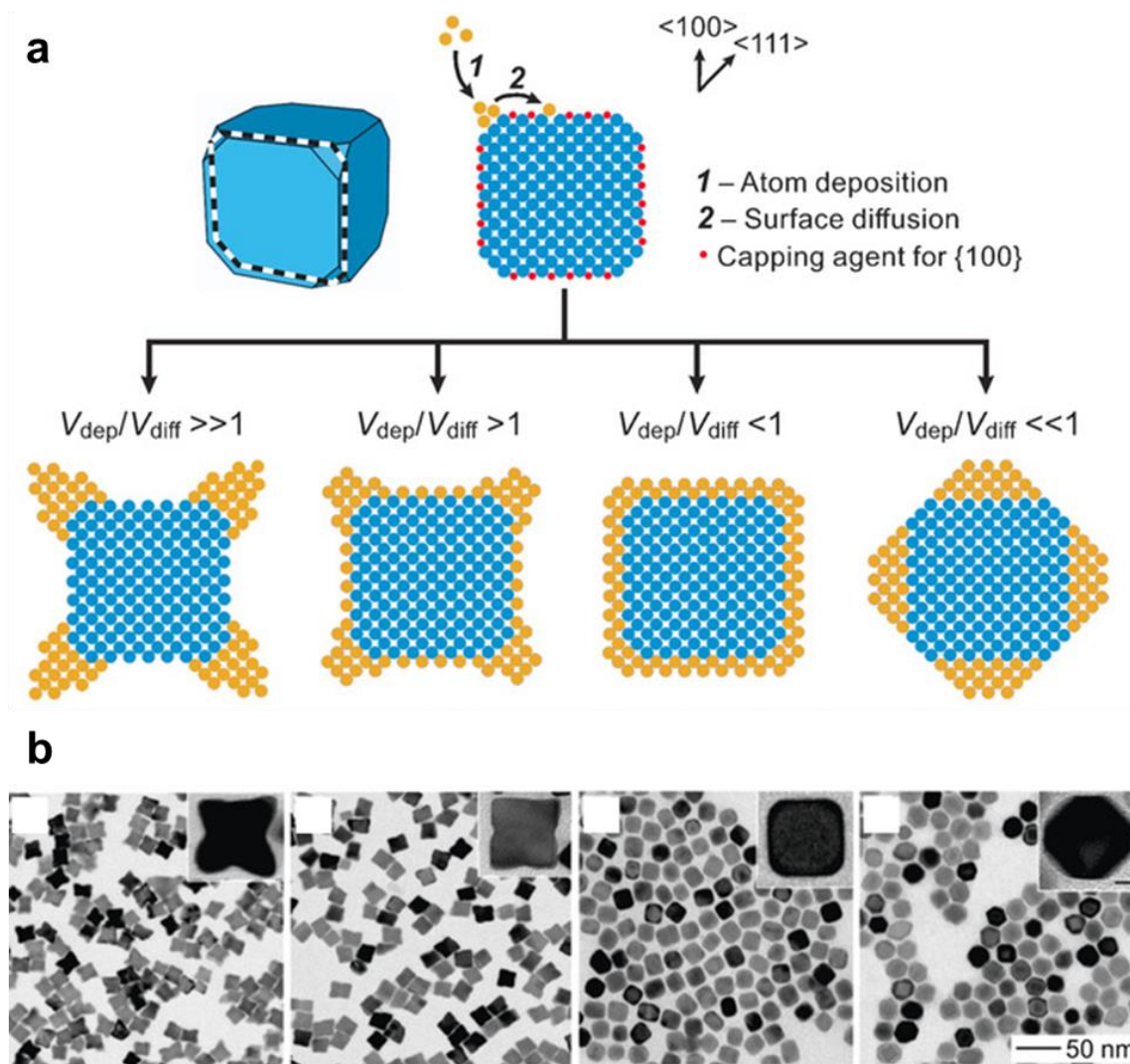


Figure 1.5 (a) Schematics showing tuning of growth modes by tuning relationship between the deposition rate and the diffusion rate. (b) Overgrowth of Pd on Pd nanocubes with different precursor injection rates. Adapted with permission of ref 16. Copyright 2013 National Academy of Sciences

In addition to the kinetic control of deposition rate and diffusion rate, the island growth can also be introduced by changing the growth modes of the depositing metals. As shown in Figure 1.6, the growth mode of a secondary metal B on the substrate A can be estimated by the overall excess energy $\Delta\gamma = \gamma_A + \gamma_{int} + \gamma_{strain} - \gamma_B$, where γ_A , γ_B , γ_{int} , and γ_{strain} represent the surface energy of metal A, metal B, A-B interface and the crystal strain induced by the lattice mismatch between the two metals, respectively.³² The $\Delta\gamma$ reflects the tendency of hetero-nucleation of metal A on B surface, and the growth mode of A can be categorized into three modes: Frank-van der Merwe (FM) or layer-by-layer mode, Volmer-Weber (VW) or island growth mode, and Stranski-Krastanov (SK) or island-on-wetting mode. When $\Delta\gamma < 0$, the two metals have a strong affinity, and the growth of B follows layer-by-layer deposition, while when $\Delta\gamma > 0$, the lattice mismatch between the two metals are large, and the growth of B follows island growth where the B metals deposits on a high surface energy spot and grow into islands. The SK mode describes the situation where the lattice mismatch is relatively high but the initial $\Delta\gamma$ is below 0, the deposition of B first follows layer-by-layer mode. With the atomic layers building up, the crystal strain gradually increases and $\Delta\gamma$ shifts to above 0, at which point the growth mode of B switch to island growth. Traditionally, the island growth is observed in bimetallic systems where the depositing metal and the substrate has a large lattice mismatch, and the growth behavior is determined by the crystal strain. Recent research has proposed to induce island growth between metals with a low lattice mismatch and monometallic systems by changing the interfacial energy between the metal and the substrate.

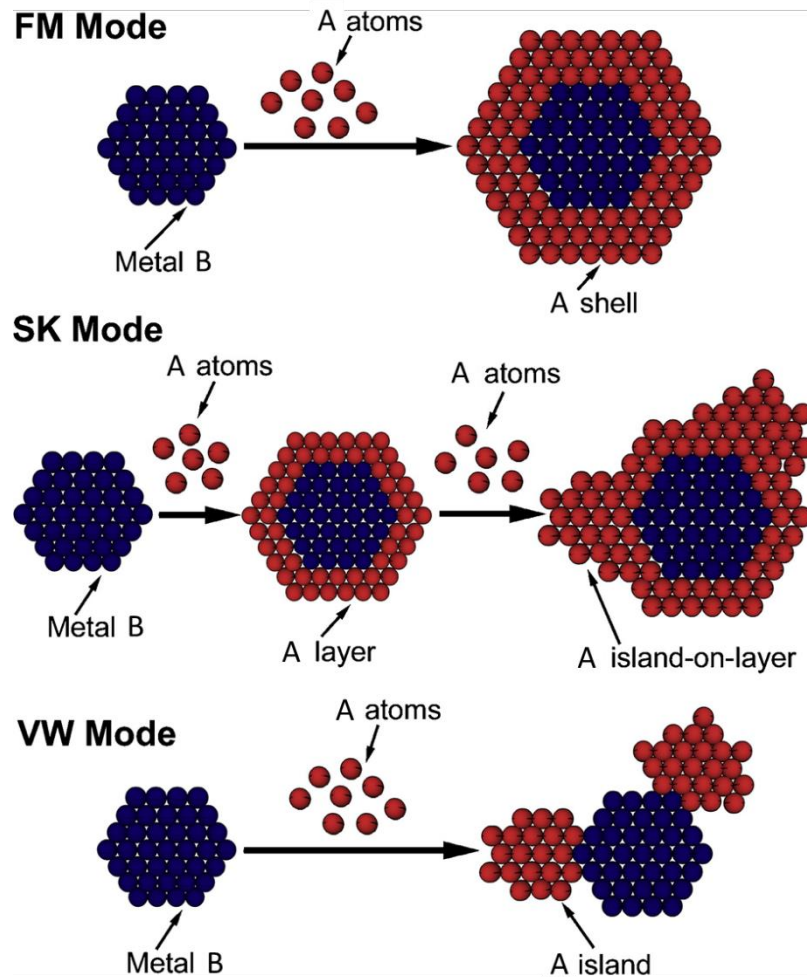


Figure 1.6 Schematic illustration of three different growth modes. Adapted with permission of ref 51. Copyright © 2008 Elsevier Ltd.

1.3 Magnetic Tuning of Plasmonic Nanoparticles

The morphology change in plasmonic nanoparticles results in an irreversible change in the optical properties. In some application scenarios, a reversible and dynamic tuning of the optical properties is preferred. The magnetic tuning appears to be an ideal solution as it can achieve the non-contact manipulation of nanoparticles at a large scale. Unlike electric field actuation and electrochemical tuning, the magnetic manipulation does not require the incorporation of electrodes in the system and has no effect in the surrounding media, which can affect the plasmonic properties, making the optical tuning unpredictable. Since most plasmonic materials do not show remarkable magnetic responses, the most common strategy is to form a composite of magnetic and plasmonic nanoparticles. It can be easily assumed that the choice of magnetic nanoparticles will determine the way the nanoparticles respond to the magnetic field. Generally, the common magnetic responsive nanoparticles can be classified as superparamagnetic and ferro/ferrimagnetic nanoparticles depending on the assembly behaviors and isotropic and anisotropic depending on the shape of the nanoparticles. As shown in Figure 1.7, due to the fast random flipping of the magnetizing direction, the magnetization of superparamagnetic nanoparticles appears to be average zero without an external magnetic field. With the magnetic field applied, the magnetization direction instantly changes to align with the external magnetic field and show a strong magnetic response, while when the external magnetic field is removed, the apparent magnetization will return to zero due to thermal fluctuations. When the magnetic field direction changes, the magnetization in each nanoparticle will rearrange, and the nanoparticles reassemble along the external field.

In isotropic ferromagnetic or ferrimagnetic nanoparticles, however, the nanoparticles will remain magnetized after the external magnetic field is removed. When the magnetic field changes, the nanoparticles will rotate to align the magnetic dipoles with the external field. In the case of anisotropic ferromagnetic nanoparticles, when the external magnetic field is first applied, the magnetization will follow the easy axis of the geometry, and the nanoparticles will rotate to align the easy axis with the external field. When the magnetic field changes direction, the orientation of the nanoparticles will change accordingly. The different responses of the magnetic nanoparticles greatly determine the tuning behavior and the application scenarios of the magnetic/plasmonic composites.

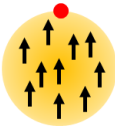
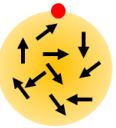
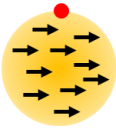
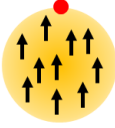
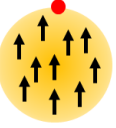
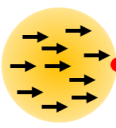


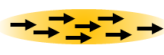
Magnetic Field Direction Type of Materials	↑	none	→
Isotropic Paramagnetic			
Isotropic Ferromagnetic			
Anisotropic Ferromagnetic			

Figure 1.7 Schematics showing the magnetic response to external magnetic fields.

The responses of the composite generally fall into two categories, magnetic separation and oriental control. Although the magnetic separation of plasmonic nanoparticles does not contribute to the optical properties, it is widely used for the magnetically guided movement of nanoparticles, especially in biomedical applications.³³⁻³⁴ One of the challenges in cancer therapy is the targeting of the cancer cells. Despite the usage of antibodies targeting the cancer cells, the injected particles are delivered by the blood flow and are significantly diluted when they reach the cancer cells, lowering the chance of combination. With the guidance of a magnetic field, the nanoparticles can be concentrated at the targeted area, improving the chance of the combination between cancer cells and the nanoparticles. The magnetic field guided spatial movement does not have specific structural requirements besides the combination of the magnetic response and plasmonic nanoparticles, and a wide variety of nanostructures are capable of this purpose. A typical structure used is Fe₃O₄@Au core-shell nanoparticles. As proposed by Halas *et al.*, the Au nanoshells have a strong plasmonic response in the NIR region,³¹ which is ideal for bio-related applications. By switching the core from SiO₂ to Fe₃O₄, the plasmonic/magnetic composite can be readily used for magnetic field-assisted photothermal therapies.

Another important magnetic tuning approach is the oriental control of the nanocomposites. As stated in the previous section, the anisotropy in the geometry of the plasmonic particles will induce a second resonance mode corresponding to the electron oscillation along the longitudinal axis of the particles. As shown in Figure 1.8a, the two plasmonic modes can be separately excited with linearly polarized light. When the

polarization of the incident light is perpendicular to the longitudinal axis of the nanorods, only the transverse mode will be excited, while when the polarization of the light is parallel to the longitudinal axis, the only longitudinal mode will be excited. The polarization-sensitive optical response opens new opportunities such as anticounterfeiting, data encryption, and light signal modulation.³⁵⁻³⁷ The polarization dependence of the plasmonic properties naturally associates with the magnetic response of the anisotropic nanoparticles. As shown in Figure 1.8b, we have shown that by attaching the Au nanorods on $\text{Fe}_3\text{O}_4@\text{SiO}_2$ nanorods modified with amino groups, the orientation of the Au nanorods can be tuned with the external magnetic field, thus allows selective excitation of the longitudinal and transverse plasmonic modes. This allows the modulation of optical signals at certain wavelengths by periodically rotating magnetic fields.

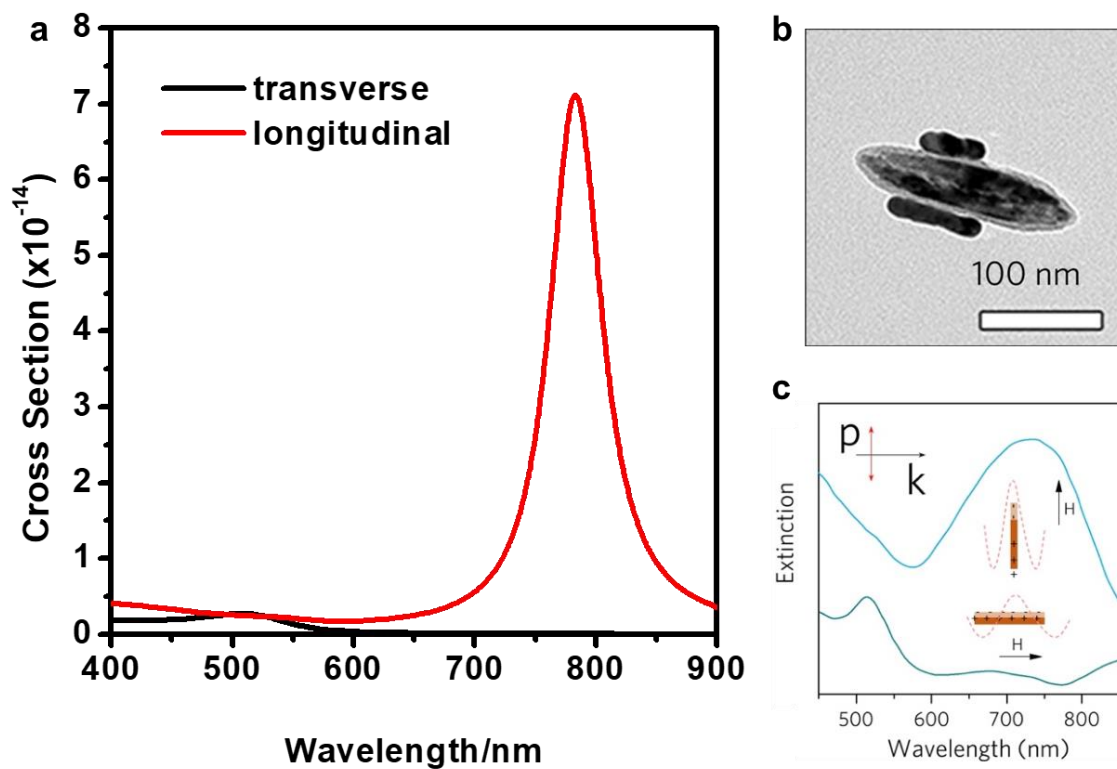


Figure 1.8 (a) Simulated spectra of Au nanorods with incident light polarization aligned with the longitudinal and transverse axis of the nanorods. (b) TEM image showing the parallel attachment of AuNRs and $\text{Fe}_3\text{O}_4@\text{SiO}_2$ nanorods. (c) UV-vis spectra of the nanocomposite with different magnetic field directions. Adapted with permission of ref 57.

1.4 Non-Noble Metal Plasmonic Nanoparticles

In the past few decades, the research in plasmonic nanoparticles has been focused on Au and Ag nanoparticles due to the pronounced optical response and the stability of noble metal nanoparticles. In recent years, the scope of research has been broadened to the search for alternative materials to make the plasmonic materials more accessible. In addition, the unique physical and chemical properties may add to the plasmonic nanoparticles and bring new potential applications of the plasmonic nanoparticles. According to Equation 1, the LSPR wavelengths and the extinction cross-sections of 20 nm nanoparticles of different metals are plotted in Figure 1.9. It can be seen that Au and Ag are not actually the most effective plasmonic materials. Since the plasmonic properties of metal nanoparticles are determined by charge carrier density and the attraction between the metal cations and the electrons, it can be easily assumed that the alkali and alkaline earth metals will exhibit excellent plasmonic performances. Among the main group metals, with increasing group number, the extinction cross-section will increase due to the increasing abundance of electrons, while the plasmonic peak will blue shift since the attraction to electrons greatly increases with higher valent cations. However, the high chemical activity of alkali and alkaline earth metals limited their applications as plasmonic materials. A potential main group metal that attracted great interest as an efficient plasmonic material is Al. As shown in the simulation results, Al has a much higher extinction cross-section than Ag with a similar size. One drawback of Al as plasmonic material is the fact that the resonance wavelength of Al is located in the deep UV region; however, the plasmonic peak can be redshifted to the visible range with the fabrication of

anisotropic nanoparticles or through coupling between particles. Although Al may suffer from the high reactivity similar to alkali and alkaline earth metals, the condensed nature of Al_2O_3 film on the Al nanoparticle surface will prevent the further oxidation of Al, and the influence from oxidation is limited. In transition metals, the trend is not as clear since the electron structures are more complicated. A few promising candidates for alternative materials for Au and Ag are Cu and Ni. Although both materials suffer from the plasmonic peak overlapping with the interband transition band, thus lowering the plasmonic quality of these metals, this can be avoided or minimized by shifting the plasmonic resonance wavelength away from the interband transition band. As shown in our previous work,³⁸ by forming Cu nanorods, the plasmonic peak of the nanostructure can be shifted away from the interband transition band, and the as-prepared Cu nanorods can exceed that of Au nanorods with similar dimensions.

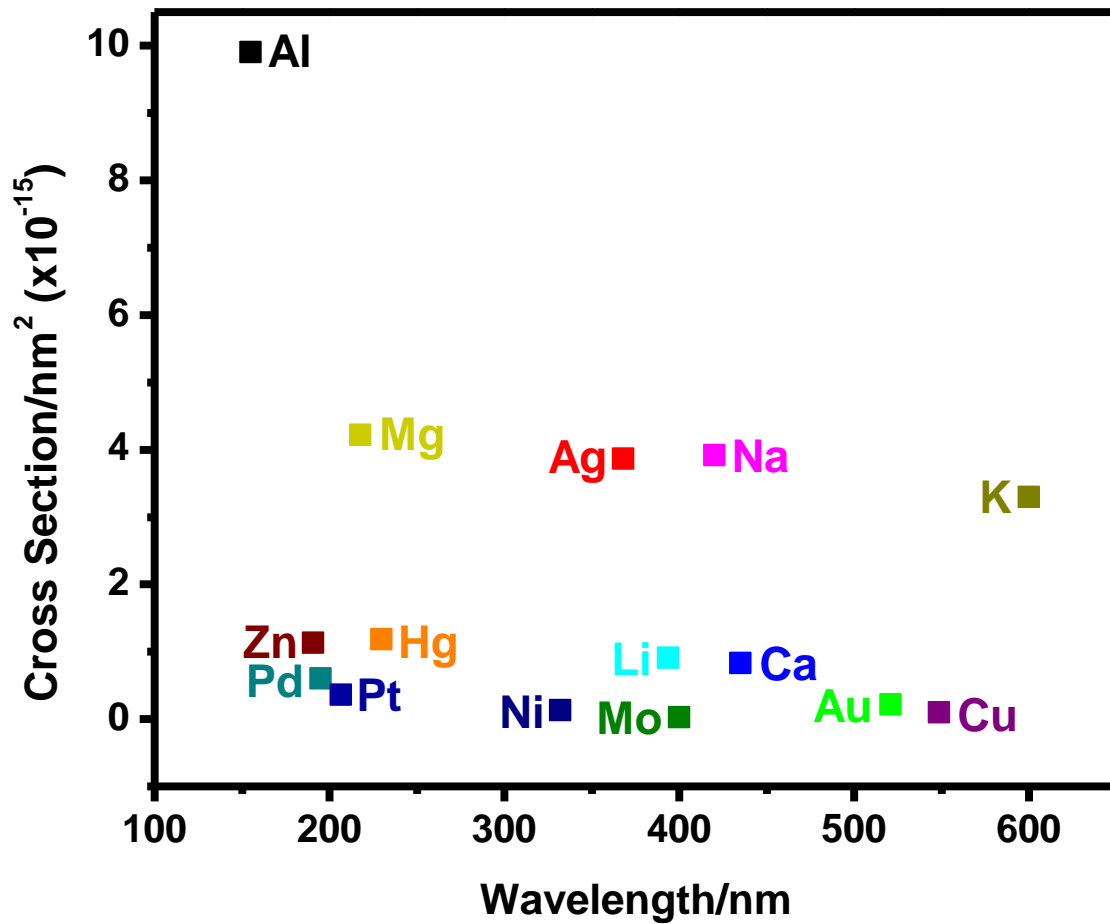


Figure 1.9 Simulated extinction cross-section of metallic nanoparticles of 20 nm size in water.

In addition to metals, recent research of plasmonic materials has also expanded to semiconductors. The plasmonic phenomenon originated from the oscillation of charge carriers. Therefore, in principle, the semiconductors can also possess plasmonic properties. The difference is that the density of free charge carriers is much lower than that in metals, resulting in the plasmonic wavelength in the IR region. However, the utilization of semiconductors as plasmonic materials brings new opportunities that are hard to achieve with noble metals. Because the charge carrier density can be changed by doping the semiconductor nanoparticles, it offers a wide tuning range of the resonance wavelengths. The typical LSPR wavelengths of semiconductors naturally locate in the IR region, which is promising in biotherapies. Small Cu_xS ,³⁹ MoO_{3-x} ⁴⁰ and CuTe ⁴¹ nanoparticles have been demonstrated as imaging and photothermal agents with LSPR peak in the NIR-II window, which typically requires a relatively large particle size and complicated structural design if Au nanoparticles are used. Furthermore, due to the different surface chemistry, semiconductor nanoparticles have a different affinity towards functional groups from Au surface, therefore provide a wider choice of chemicals that can be detected through SERS methods.⁴¹ In addition, semiconductors typically have a higher melting point and thermal stability compared with metals, therefore allows the applications of plasmonic materials in high-temperature photothermal devices, such as solar thermal power generation. As shown in Figure 1.10, ZrN and TiN are promising candidates for high-temperature plasmonic applications as they are refractory with photothermal efficiency comparable to Au in the visible region.⁴²

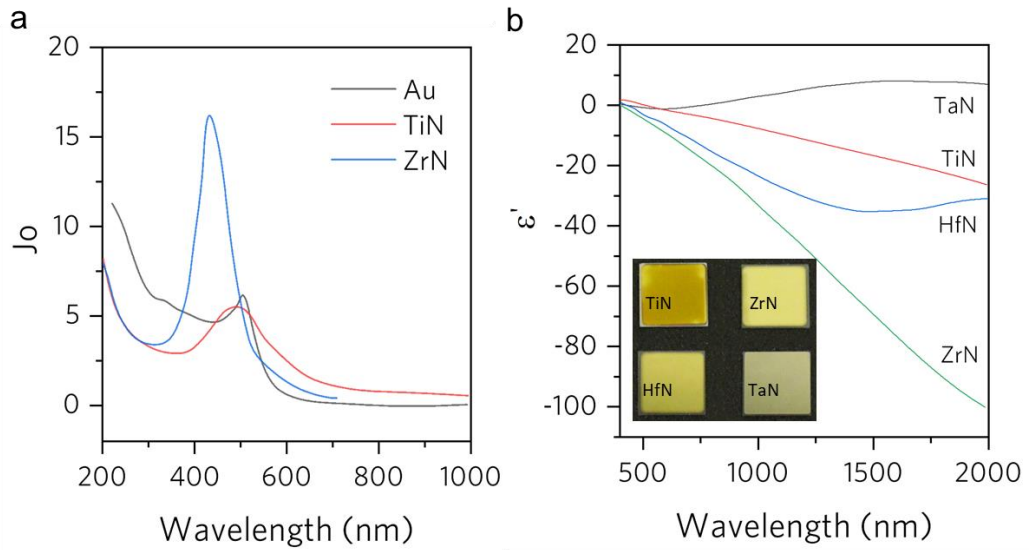


Figure 1.10 (a) Joule numbers of Au, TiN, and ZrN. (b) Optical image and dielectric functions of metal nitride. Adapted with permission of Ref 63 Copyright © 2013 WILEY-VCH Verlag GmbH & Co. KGaA, Weinheim.

1.5 Focus of This Dissertation

The fundamental of the optical tuning of plasmonic nanoparticles, including the morphology control, magnetic tuning, and choices of alternative materials has been discussed. The focus of this dissertation is related to the controlling of the optical properties and the application of plasmonic nanoparticles and can be divided into three topics: (1) the morphology control of Au nanostructures via selective island growth on Au nanostructures; (2) dynamic tuning of the optical properties of plasmonic nanostructures by the formation of plasmonic/magnetic composites; (3) Ni as non-noble metal plasmonic material with magnetic properties.

In Chapter 2, the site-selective island growth on Au nanorods will be demonstrated by controlling the surface strain profile on the Au nanorods. The relative surface strain can be changed by anisotropic PEG-SH modification, affecting the deposition location of Pd on Au nanorods. The Pd coating introduced lattice mismatch between the nanorods with the newly grown Au domains, inducing island growth on Au nanorods. The controlled distribution of Pd on Au nanorods produced a template with a surface strain profile, which further directed the growth of Au islands. We will also demonstrate the fine-tuning of the structural features of the overgrown islands and build the relationship between the features and the optical properties.

In Chapter 3, we demonstrated the dynamic tuning of plasmonic nanostructures through the formation of plasmonic/magnetic composites. Two strategies will be demonstrated in this chapter. In the first part, we demonstrate the fabrication of self-aligned Au-Au and Au-Ag dimers on Fe₃O₄ nanorods. The selective excitation of the longitudinal

mode of the dimers can be achieved at a large scale, and the application of these nanocomposites for visible anti-counterfeiting devices will be demonstrated as well. In the second part of this chapter, we focus on the fabrication of Au@Fe₃O₄ and Ag@Fe₃O₄ core-shell nanostructures to achieve a straightforward strategy towards the manipulation of pre-synthesized plasmonic nanoparticles. The magnetic manipulation of the plasmonic nanoparticles can be achieved, and we demonstrated the application of Ag@Fe₃O₄ as a magnetically actuated display.

In Chapter 4, we further explore the non-noble metal plasmonic materials and demonstrate the use of Ni as a promising plasmonic material for solar energy harvesting. The combination of Ni and C in a core-shell nanoparticle enabled the highly efficient solar-thermal conversion and showed excellent performance in solar steam generation. Furthermore, the magnetic properties of Ni bring additional benefits to the structural design of the evaporator, allowing new designing strategies toward the solar steam generation devices.

1.6 Reference

1. Faraday, M., The Bakerian Lecture: Experimental Relations of Gold (and Other Metals) to Light. *Philosophical Transactions of the Royal Society of London* **1857**, 147, 145-181.
2. Kelly, K. L.; Coronado, E.; Zhao, L. L.; Schatz, G. C., The Optical Properties of Metal Nanoparticles: The Influence of Size, Shape, and Dielectric Environment. *The Journal of Physical Chemistry B* **2003**, 107 (3), 668-677.
3. Li, M.; Cushing, S. K.; Wu, N., Plasmon-enhanced optical sensors: a review. *Analyst* **2015**, 140 (2), 386-406.
4. Zhang, X.; Li, X.; Reish, M. E.; Zhang, D.; Su, N. Q.; Gutiérrez, Y.; Moreno, F.; Yang, W.; Everitt, H. O.; Liu, J., Plasmon-Enhanced Catalysis: Distinguishing Thermal and Nonthermal Effects. *Nano Letters* **2018**, 18 (3), 1714-1723.
5. Huang, X.; El-Sayed, M. A., Plasmonic photo-thermal therapy (PPTT). *Alexandria Journal of Medicine* **2011**, 47 (1), 1-9.
6. Mie, G., Beiträge zur Optik trüber Medien, speziell kolloidaler Metallösungen. *Annalen der Physik* **1908**, 330 (3), 377-445.
7. Gans, R., Über die Form ultramikroskopischer Silberteilchen. *Annalen der Physik* **1915**, 352 (10), 270-284.
8. Taylor, A. B.; Siddiquee, A. M.; Chon, J. W. M., Below Melting Point Photothermal Reshaping of Single Gold Nanorods Driven by Surface Diffusion. *ACS Nano* **2014**, 8 (12), 12071-12079.
9. Huang, W.; Qian, W.; El-Sayed, M. A., Photothermal reshaping of prismatic Au nanoparticles in periodic monolayer arrays by femtosecond laser pulses. *Journal of Applied Physics* **2005**, 98 (11), 114301.
10. LaMer, V. K.; Dinegar, R. H., Theory, Production and Mechanism of Formation of Monodispersed Hydrosols. *Journal of the American Chemical Society* **1950**, 72 (11), 4847-4854.
11. Mer, V. K. L., Nucleation in Phase Transitions. *Industrial & Engineering Chemistry* **1952**, 44 (6), 1270-1277.
12. Xia, Y.; Gilroy, K. D.; Peng, H.-C.; Xia, X., Seed-Mediated Growth of Colloidal Metal Nanocrystals. *Angewandte Chemie International Edition* **2017**, 56 (1), 60-95.

13. Moustaoui, H.; Saber, J.; Djeddi, I.; Liu, Q.; Diallo, A. T.; Spadavecchia, J.; Lamy de la Chapelle, M.; Djaker, N., Shape and Size Effect on Photothermal Heat Elevation of Gold Nanoparticles: Absorption Coefficient Experimental Measurement of Spherical and Urchin-Shaped Gold Nanoparticles. *The Journal of Physical Chemistry C* **2019**, *123* (28), 17548-17554.
14. Chang, C.; Yang, C.; Liu, Y.; Tao, P.; Song, C.; Shang, W.; Wu, J.; Deng, T., Efficient Solar-Thermal Energy Harvest Driven by Interfacial Plasmonic Heating-Assisted Evaporation. *ACS Applied Materials & Interfaces* **2016**, *8* (35), 23412-23418.
15. Turkevich, J.; Stevenson, P. C.; Hillier, J., A study of the nucleation and growth processes in the synthesis of colloidal gold. *Discussions of the Faraday Society* **1951**, *11* (0), 55-75.
16. Ojea-Jiménez, I.; Romero, F. M.; Bastús, N. G.; Puentes, V., Small Gold Nanoparticles Synthesized with Sodium Citrate and Heavy Water: Insights into the Reaction Mechanism. *The Journal of Physical Chemistry C* **2010**, *114* (4), 1800-1804.
17. Bastús, N. G.; Piella, J.; Puentes, V., Quantifying the Sensitivity of Multipolar (Dipolar, Quadrupolar, and Octapolar) Surface Plasmon Resonances in Silver Nanoparticles: The Effect of Size, Composition, and Surface Coating. *Langmuir* **2016**, *32* (1), 290-300.
18. Gao, C.; Vuong, J.; Zhang, Q.; Liu, Y.; Yin, Y., One-step seeded growth of Au nanoparticles with widely tunable sizes. *Nanoscale* **2012**, *4* (9), 2875-2878.
19. Link, S.; Mohamed, M. B.; El-Sayed, M. A., Simulation of the Optical Absorption Spectra of Gold Nanorods as a Function of Their Aspect Ratio and the Effect of the Medium Dielectric Constant. *The Journal of Physical Chemistry B* **1999**, *103* (16), 3073-3077.
20. Link, S.; El-Sayed, M. A., Simulation of the Optical Absorption Spectra of Gold Nanorods as a Function of Their Aspect Ratio and the Effect of the Medium Dielectric Constant. *The Journal of Physical Chemistry B* **2005**, *109* (20), 10531-10532.
21. Kahnert, M., Numerical solutions of the macroscopic Maxwell equations for scattering by non-spherical particles: A tutorial review. *Journal of Quantitative Spectroscopy and Radiative Transfer* **2016**, *178*, 22-37.
22. Carbó-Argibay, E.; Rodríguez-González, B.; Gómez-Graña, S.; Guerrero-Martínez, A.; Pastoriza-Santos, I.; Pérez-Juste, J.; Liz-Marzán, L. M., The Crystalline Structure of Gold Nanorods Revisited: Evidence for Higher-Index Lateral Facets. *Angewandte Chemie International Edition* **2010**, *49* (49), 9397-9400.

23. Scarabelli, L.; Sánchez-Iglesias, A.; Pérez-Juste, J.; Liz-Marzán, L. M., A “Tips and Tricks” Practical Guide to the Synthesis of Gold Nanorods. *The Journal of Physical Chemistry Letters* **2015**, *6* (21), 4270-4279.
24. Park, K.; Drummy, L. F.; Wadams, R. C.; Koerner, H.; Nepal, D.; Fabris, L.; Vaia, R. A., Growth Mechanism of Gold Nanorods. *Chemistry of Materials* **2013**, *25* (4), 555-563.
25. Tong, W.; Walsh, M. J.; Mulvaney, P.; Etheridge, J.; Funston, A. M., Control of Symmetry Breaking Size and Aspect Ratio in Gold Nanorods: Underlying Role of Silver Nitrate. *The Journal of Physical Chemistry C* **2017**, *121* (6), 3549-3559.
26. Jin, B.; Sushko, M. L.; Liu, Z.; Cao, X.; Jin, C.; Tang, R., Understanding Anisotropic Growth of Au Penta-Twinned Nanorods by Liquid Cell Transmission Electron Microscopy. *The Journal of Physical Chemistry Letters* **2019**, *10* (7), 1443-1449.
27. Seo, D.; Park, J. H.; Jung, J.; Park, S. M.; Ryu, S.; Kwak, J.; Song, H., One-Dimensional Gold Nanostructures through Directed Anisotropic Overgrowth from Gold Decahedrons. *The Journal of Physical Chemistry C* **2009**, *113* (9), 3449-3454.
28. Kim, W.; Kim, N.; Park, J. W.; Kim, Z. H., Nanostar probes for tip-enhanced spectroscopy. *Nanoscale* **2016**, *8* (2), 987-994.
29. Wang, G.; Liu, Y.; Gao, C.; Guo, L.; Chi, M.; Ijro, K.; Maeda, M.; Yin, Y., Island Growth in the Seed-Mediated Overgrowth of Monometallic Colloidal Nanostructures. *Chem* **2017**, *3* (4), 678-690.
30. Jia, J.; Liu, G.; Xu, W.; Tian, X.; Li, S.; Han, F.; Feng, Y.; Dong, X.; Chen, H., Fine-Tuning the Homometallic Interface of Au-on-Au Nanorods and Their Photothermal Therapy in the NIR-II Window. *Angewandte Chemie International Edition* **2020**, *59* (34), 14443-14448.
31. Prodan, E.; Radloff, C.; Halas, N. J.; Nordlander, P., A Hybridization Model for the Plasmon Response of Complex Nanostructures. *Science* **2003**, *302* (5644), 419.
32. Peng, Z.; Yang, H., Designer platinum nanoparticles: Control of shape, composition in alloy, nanostructure and electrocatalytic property. *Nano Today* **2009**, *4* (2), 143-164.
33. Xu, Z.; Hou, Y.; Sun, S., Magnetic Core/Shell Fe₃O₄/Au and Fe₃O₄/Au/Ag Nanoparticles with Tunable Plasmonic Properties. *Journal of the American Chemical Society* **2007**, *129* (28), 8698-8699.
34. Brennan, G.; Thorat, N. D.; Pescio, M.; Bergamino, S.; Bauer, J.; Liu, N.; Tofail, S. A. M.; Silien, C., Spectral drifts in surface textured Fe₃O₄-Au, core-shell nanoparticles

enhance spectra-selective photothermal heating and scatter imaging. *Nanoscale* **2020**, *12* (23), 12632-12638.

35. Zijlstra, P.; Chon, J. W. M.; Gu, M., Five-dimensional optical recording mediated by surface plasmons in gold nanorods. *Nature* **2009**, *459* (7245), 410-413.

36. Wang, M.; Gao, C.; He, L.; Lu, Q.; Zhang, J.; Tang, C.; Zorba, S.; Yin, Y., Magnetic Tuning of Plasmonic Excitation of Gold Nanorods. *Journal of the American Chemical Society* **2013**, *135* (41), 15302-15305.

37. Li, Z.; Jin, J.; Yang, F.; Song, N.; Yin, Y., Coupling magnetic and plasmonic anisotropy in hybrid nanorods for mechanochromic responses. *Nature Communications* **2020**, *11* (1), 2883.

38. Chen, J.; Feng, J.; Yang, F.; Aleisa, R.; Zhang, Q.; Yin, Y., Space-Confined Seeded Growth of Cu Nanorods with Strong Surface Plasmon Resonance for Photothermal Actuation. *Angewandte Chemie International Edition* **2019**, *58* (27), 9275-9281.

39. Gao, W.; Sun, Y.; Cai, M.; Zhao, Y.; Cao, W.; Liu, Z.; Cui, G.; Tang, B., Copper sulfide nanoparticles as a photothermal switch for TRPV1 signaling to attenuate atherosclerosis. *Nature Communications* **2018**, *9* (1), 231.

40. Bao, T.; Yin, W.; Zheng, X.; Zhang, X.; Yu, J.; Dong, X.; Yong, Y.; Gao, F.; Yan, L.; Gu, Z.; Zhao, Y., One-pot synthesis of PEGylated plasmonic MoO_{3-x} hollow nanospheres for photoacoustic imaging guided chemo-photothermal combinational therapy of cancer. *Biomaterials* **2016**, *76*, 11-24.

41. Li, W.; Zamani, R.; Rivera Gil, P.; Pelaz, B.; Ibáñez, M.; Cadavid, D.; Shavel, A.; Alvarez-Puebla, R. A.; Parak, W. J.; Arbiol, J.; Cabot, A., CuTe Nanocrystals: Shape and Size Control, Plasmonic Properties, and Use as SERS Probes and Photothermal Agents. *Journal of the American Chemical Society* **2013**, *135* (19), 7098-7101.

42. Naik, G. V.; Shalaev, V. M.; Boltasseva, A., Alternative Plasmonic Materials: Beyond Gold and Silver. *Advanced Materials* **2013**, *25* (24), 3264-3294.

Chapter 2 Site-Selective Island Growth on Au Nanoparticles

2.1 Introduction

Plasmonic nanoparticles have attracted great attention due to their unique optical properties and potentials in a wide range of applications such as catalysis,¹ sensing² and biomedicine.³⁻⁴ Over the past few decades, synthetic protocols of plasmonic nanoparticles with various sizes and morphologies have been heavily investigated, and the relationship between the particle morphologies and their optical properties has been established.⁵⁻⁸ Among the reported methods, seed-mediated growth has proved to be an efficient strategy to obtain monodispersed nanocrystals with well-controlled shapes through the seed crystal structure and growth kinetics control. In recent researches, the scope of this synthetic method has expanded from the facet-directed shape control to the creation of more complex nanostructures by exploring novel growth paths.⁹⁻¹⁴ Island growth, for example, could produce secondary features that are difficult to achieve in the traditional layer-by-layer deposition.

As discussed in Chapter 1, the island growth on metal nanoparticles can be typically induced by two strategies, growth kinetic control and growth mode control through surface strain and lattice mismatch. The kinetic control is typically applied in monometallic systems where the depositing metal and the substrate are the same. The two domains essentially have no lattice mismatch, and the island growth mode is not thermodynamically favored. By promoting the deposition of the metal, which develops the high energy sites and suppressing the surface diffusion that leads to the minimized overall surface energy, island growth can be induced in the monometallic systems.

On the other hand, the tuning of growth modes is commonly utilized in bimetallic systems. When the two metals have a relatively large lattice mismatch, it is easy to induce the island growth of the depositing metal since the crystal strain induced by the lattice mismatch to exceed the reduced surface energy by forming metal interfaces. However, the two most well-studied metals, Au and Ag, have almost neglectable lattice mismatch, and the epitaxial growth is favored in the seed-mediated synthesis. As proposed by Hongyu Chen *et al.*,¹⁵⁻¹⁶ the growth mode of the Ag on Au nanoparticles can be changed by inducing sufficiently large surface strain, which has been thoroughly discussed in Chapter 1. This strategy can be expanded to the monometallic systems, and as demonstrated by Yu Han *et al.*,¹⁰ island growth of Au on Au nanorods can be induced by modifying the Au nanorods with a strong binding hydrophobic ligand.

Previously in our group, we also proposed the island growth of Au on Au nanoparticles by introducing a thin layer of Pt. When the Au nanoparticles were coated with a thin layer of Pt, the substrate surface essentially became Pt without severely compromising the optical properties of the Au nanoparticles. The relatively large lattice mismatch between Pt and Au causes large crystal strain on newly deposited Au domains, leading to the growth of islands on Au nanoparticles. By controlling the Oswald ripening process, the number of islands deposited on the Au nanoparticles can be tuned.

In this work, we initiated the island growth on Au nanorods (AuNRs) by the introduction of a thin Pd layer, which greatly increases the surface strain due to the lattice mismatch between Pd and Au. The anisotropic modification of thiol terminated poly(ethylene glycol) (PEGSH) changed the interfacial energy profile on AuNRs, limiting

the deposition of Pd on AuNRs. The strain difference in PEGSH modified, and Pd coated regions created a robust template to guide the deposition of Au islands in the overgrowth. By changing the synthesis parameters in the system, the number, size, distance, and wetting degree of islands can be systematically tuned to achieve precise tailoring of the LSPR properties of obtained nanostructures. Furthermore, this method can be extended to other Au nanostructures such as nanoplates, nanocubes, and rhombic dodecahedrons, showing the versatility of the site-selective island growth strategy.

2.2 Experimental

2.2.1 Chemicals

Gold chloride (AuCl_3), diethylamine (DEA), potassium iodide (KI), and sodium hydroxide (NaOH) were purchased from Fisher Scientific. Sodium borohydride (NaBH_4) was purchased from MP biomedical, LLC. Hexadecyl-trimethylammonium bromide (CTAB, > 99%), L-ascorbic acid (AA, >99.0%), poly(ethylene glycol) methyl ether thiol (PEGSH, Mw. ~2000), palladium (II) chloride (PdCl_2 , 99%), polyvinylpyrrolidone (PVP, Mw. 10000), sodium citrate tribasic dihydrate (TSC, > 99.0%), L-cysteine (>99%), mercapto-acetic acid (>99%), tannic acid and cetyltrimethylammonium chloride (CTAC, 25 wt.% in water) were purchased from Sigma-Aldrich, Inc. Silver nitrate (AgNO_3 , 99.9+%) was purchased from Alfa Aescar. Poly(ethylene glycol) methyl ether amine (PEGNH₂, Mw. ~2000) was purchased from Laysen Bio, Inc. Potassium bromide was purchased from Matheson Coleman & Bell, Inc.

2.2.2 Synthesis of Au nanorods (AuNRs)

The Au nanorods were synthesized with a method published by Jianfang Wang with slight modification.¹⁷ A seed solution was first prepared with the addition of 60 μL of freshly prepared 0.1 M NaBH_4 solution into 10 mL of a solution containing 0.1 M CTAB and 0.25 mM HAuCl_4 . The mixture was stirred vigorously for 30 s, then aged at 25 °C without disturbance for at least 30 min to remove unreacted NaBH_4 . The growth solution was prepared by combining 40 mL 0.1 M CTAB, 2 mL 0.01 M HAuCl_4 , 0.4 mL 0.01 M AgNO_3 , 0.8 mL 1 M HCl and 0.32 mL 0.1 M AA in sequence. The growth of AuNRs was initiated by adding 96 μL seed solution into the growth solution. The mixture was vigorously stirred for 30 s and kept undisturbed at 25 C for 12 h. The synthesized AuNRs were separated by centrifugation at 9000 rpm for 30 min. The AuNRs were washed with water twice and redispersed in 20 mL 0.01 M CTAB solution to make the AuNRs concentration equal to 1 mM.

2.2.3 Synthesis of Au Nanoplates (AuPLTs)

The CTAC-capped Au nanoplates were synthesized with a previously reported method by Qiao Zhang.¹⁸ In a 50 mL flask, 20 mL of water and 4 mL 0.1 M CTAC solution was added, followed by the addition of 375 μL 0.01 M KI. A mixture of 400 μL 25 mM HAuCl_4 and 100 μL of 0.1 M NaOH was added sequentially to make a yellowish color. After injecting 400 μL of 0.064 M AA under moderate stirring, the solution turned colorless. The Au nanoplate growth was initiated with the injection of 50 μL 0.1 M NaOH. The solution was vigorously stirred for 10 s and leave undisturbed for 10 min. The

nanoplates were separated with centrifugation at 9000 rpm for 10 min and redispersed in 10 mL of 0.01 M CTAB solution.

2.2.4 Synthesis of Au Nanocubes (AuCBs) and Rhombic Dodecahedrons (AuRDs)

The Au nanocubes and rhombic dodecahedrons were synthesized with a method reported by Michael Huang.¹⁹ In a 20 mL flask, 10 mL 0.1 M CTAC was added, followed by the addition of 250 μ L 10 mM HAuCl₄ solution. Into the mixture, 0.45 mL of freshly prepared 0.2 M NaBH₄ solution was quickly injected under vigorous stirring. The seed solution was aged for 1 h at 30 °C before using.

For the growth of Au nanocubes, two vials were labeled A and B. A growth solution was prepared in each of the two vials. In each vial, 10 mL of 0.1 M CTAC was added, followed by the addition of 250 μ L of 0.01 M HAuCl₄, and 10 μ L of 0.01 M KBr were added. Finally, 90 μ L of 0.04 M AA was added. To initiate the crystal growth, 45 μ L seed solution was added to vial A under vigorous stirring. After 10 s, solution A turned pink, and 45 μ L of solution A was injected into vial B. The mixture was stirred for 10 s and left undisturbed for 15 min. The Au nanocubes were separated by centrifugation at 7000 rpm for 15 min and redispersed in 2.5 mL 0.01 M CTAB solution. For the synthesis of Au rhombic dodecahedrons, 150 μ L of 0.04 M AA instead of 90 μ L was added to each growth solution.

2.2.5 Synthesis of Au@Pd nanorods (Au@PdNRs)

The AuNRs were first modified with PEGSH before Pd deposition. Into 5 mL of AuNRs solution, 0.5 mL of 1 mM PEGSH solution was added. The solution was stirred for 2 h for the selective modification of PEGSH on Au nanorods. The modified AuNRs

were centrifuged and redispersed in 5 mL of 2 mM CTAB solution. Various amount of PEGSH solution was added to obtain AuNRs modified with different PEGSH/Au ratios. To initiate the Pd deposition, 500 μ L 0.1 M AA and 50 μ L 0.02 M H_2PdCl_4 solution were added under stirring. The mixture was stirred for 30 min before centrifugation. The Au@PdNRs were centrifuged at 9000 rpm for 10 min to remove unreacted chemicals and redispersed in 1 mL of water.

The selective Pd deposition on other Au nanostructures (AuPLTs, AuCBs, AuRDs) was carried out with the same procedure, with slight modifications of PEGSH/Au and Pd/Au ratio, and the amount of AA was adjusted proportionally according to the amount of H_2PdCl_4 added. More specifically, for AuPLTs, PEGSH/Au ratio = 0.05 and Pd/Au ratio = 0.1 was used, while for AuNBs and AuRDs, PEGSH/Au ratio = 0.05 and Pd/Au ratio = 0.2 was used.

2.2.6 Ligand Exchange of Au@PdNRs

Before island growth, the ligand of Au@PdNRs was changed from CTAB into citrate with a previously reported ligand exchange process. Generally, 1 mL of Au@PdNRs solution was added into 3 mL of ethanol. Into the mixture, 100 μ L of 5% PVP solution was added and stirred for 4 h. The Au@PdNRs were then centrifuged and redispersed in 1 mL of water. Into the Au@PdNRs solution, 50 μ L of DEA was added and stirred for 2 h to exchange the ligand into DEA. To finally exchange the ligand into citrate, the Au@PdNRs were centrifuged and redispersed in 1 mL of water, and 20 μ L 10 mg/mL TSC and 40 μ L 10 mg/mL tannic acid were added. The solution was stirred for 1 h then centrifuged to remove supernatant. The collected Au@PdNRs were redispersed in 5 mL of water.

The same ligand exchange processes were performed on other Au@Pd nanostructures (Au@PdPLTs, Au@PdCBs, and Au@PdRDs).

2.2.7 Island Growth on Au@PdNRs

The growth solution used for island growth was first prepared. Into 0.5 mL of water, 20 μ L 5 wt.% PVP solution, 50 μ L 0.01 M HAuCl₄, 25 μ L 0.2 M KI and 5 μ L 0.1 M AA were added. The above growth solution was injected into 0.5 mL of Au@PdNRs dispersion, and the mixture was stirred for 30 min. The overgrown Au@PdNRs were separated by centrifuging at 8000 rpm for 5 min and redispersed in water for characterization. The same processes were carried out for the site-selective island growth on other Au@Pd nanostructures.

2.2.8 Characterization

The sample morphology was characterized by a Tecnai 12 TEM. The morphology of the overgrown Au rhombic dodecahedrons was characterized by an FEI Nova NanoSEM 450 SEM. UV-Vis spectra were measured with an Ocean Optics HR2000 CG-UV-NIR spectrometer. The UV-vis-NIR spectra were measured with a Cary 5000 double beam UV-Vis-NIR spectrometer. FTIR spectra were measured with a Thermo Nicolet 6700 FTIR spectrometer.

2.3 Results and Discussion

2.3.1 Controlling the Island Growth Modes on Au Nanorods by Changing Surface Strain Profiles

The site-selective island growth on AuNRs was performed by first modifying AuNRs with thiol-terminated poly(ethylene glycol) (PEGSH), after which a layer of Pd

was coated on the PEGSH modified AuNRs. The as-prepared Au@PdNRs were used as seeds for island growth. It has been reported that at a moderate concentration, PEGSH can be selectively modified on the tips of AuNRs because the packing density of CTAB on the tips of AuNRs is lower than it is on the sides.²⁰⁻²² Here, we took advantage of anisotropic modification of PEGSH to limit the deposition of Pd on the AuNRs, which further influenced the growth of Au islands. Figure 2.1a shows the scheme to tune the growth modes of islands on AuNRs through anisotropic PEGSH modification and Pd deposition. As discussed in Chapter 1, the growth behavior of a secondary metal on a metal substrate can be determined by the overall surface excess energy $\Delta\gamma$:

$$\Delta\gamma = \gamma_A + \gamma_{interfacial} + \gamma_{strain} - \gamma_B \quad (2.1)$$

where γ_A and γ_B are the surface energy of metal A and B in solution respectively, $\gamma_{interfacial}$ is the interfacial energy between metal A and B, and γ_{strain} is the energy introduced by crystal strain due to the crystal mismatch between metal A and B. It is well known that Pd and Au has a moderate lattice mismatch (~5.3%), and the deposition mode of Pd can be changed by changing the interfacial energy and the growth kinetics of Pd.²³ As shown in Figure 2.1a, the modification of PEGSH could limit the growth of Pd at different regions by increasing local interfacial strain. With no PEGSH modification, because the packing density of CTAB on the tips of AuNRs was lower than it was on the sides, the tips of the AuNRs had higher surface energy. Therefore, Pd preferentially deposited on the tips of AuNRs (denoted as Au@Pd₀PEGSHNRs). When AuNRs were modified with PEGSH, the strong bonding between Au and thiol groups increased the interfacial strain between Au and Pd. Due to the lattice mismatch between Au and Pd, increasing interfacial strain, even

to a small extent, will influence the deposition of Pd. At a low PEGSH/Au ratio, the strain induced by the Au-S bond compensated the strain difference originated from different packing densities of CTAB; therefore, Pd deposit universally on AuNRs surface (denoted as Au@Pd_{0.01}PEGSHNRs). When PEGSH/Au ratio was further increased, the interfacial strain between Pd and Au was greatly increased, and the surface strain profile was switched. The excess surface energy $\Delta\gamma$ on the tips was positive, while $\Delta\gamma$ negative in the middle. The deposition of Pd was limited in the middle of the AuNRs (denoted as Au@Pd_{0.1}PEGSHNRs), where there was no PEGSH modification. Although the thin Pd layer was not visible in the TEM images, the UV-vis spectra of the three Au@Pd nanorods showed a great difference. As shown in Figure 2.1b, the longitudinal peak of the Au@Pd₀PEGSHNRs redshifted comparing to the original AuNRs, and with increasing PEGSH/Au ratio, the plasmonic peak of the Au@PdNRs gradually blue shift. The computational simulation result (Figure 2.1c) showed the same blue shifting trend with decreasing Pd coverage, confirming our theory of limited Pd deposition on the sides.

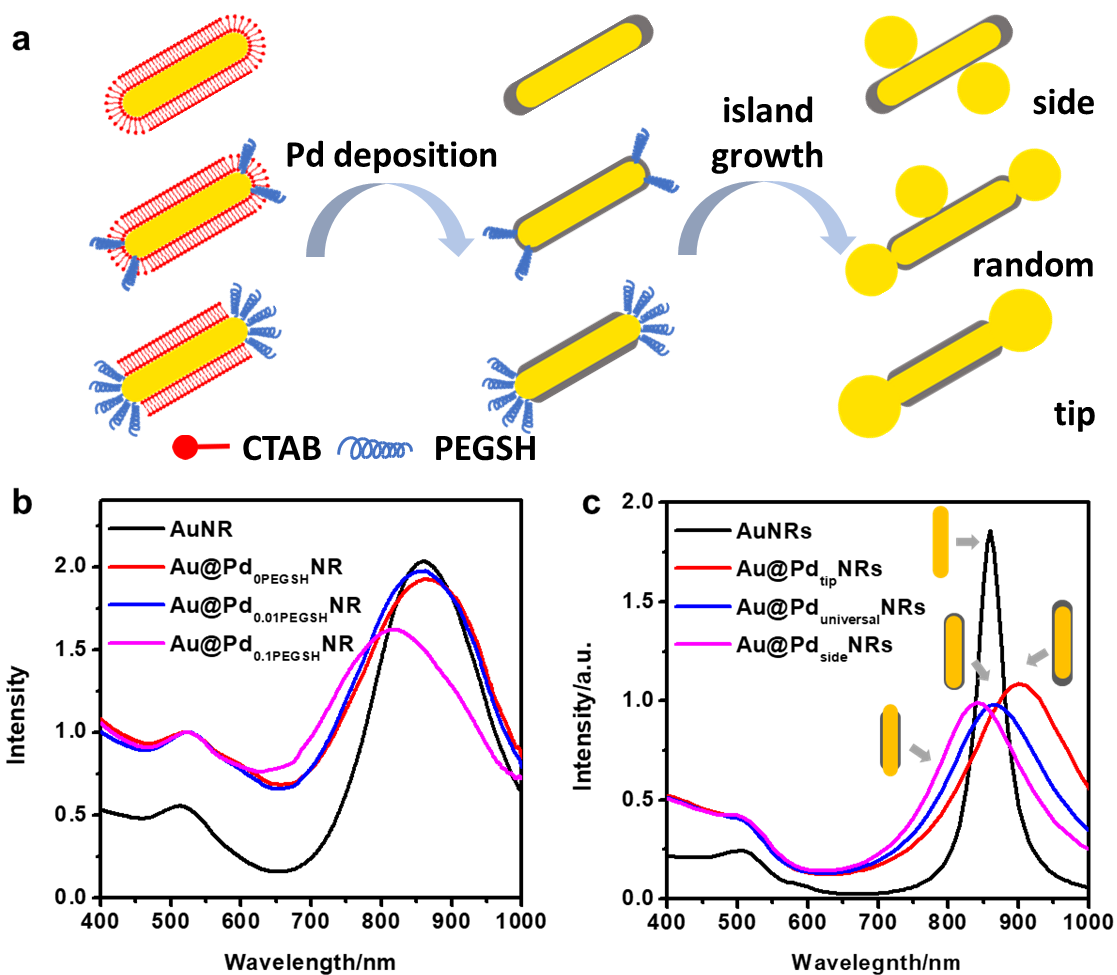


Figure 2.1 (a) Schematics showing the island growth modes on AuNRs controlled by anisotropic modification of PEGSH and selective deposition of Pd. (b) UV-vis spectra of AuNRs and Au@PdNRs with different PEGSH/Au ratios. (c) Simulated spectra of AuNRs and Au@PdNRs with different coverage of Pd.

The island growth on as-prepared Au@PdNRs was initiated with the addition of a growth solution containing H₂AuCl₄, AA, and KI in the presence of PVP as the surfactant. To eliminate the influence of CTAB during island growth, a ligand exchange was performed according to previously reported procedures to change the ligands on Au@PdNRs into citrate, and the FTIR spectrum (Figure 2.2a) and zeta-potential of Au@PdNRs (Figure 2.2b) confirmed the successful ligand exchange. The ripening promoted by the addition of KI played an important role in the site selectivity of the island growth. Briefly, the ripening process eliminated the unstable small islands through oxidative etching and promoted the growth of remaining islands to reduce surface area and overall surface energy. When the Au@Pd₀PEGSHNRs were used as seeds, the tips of the nanorods had a higher crystal strain due to the thicker Pd coating. As a result, the island on the tips was highly strained and etched during ripening. The growth of islands mainly happened on the side of the nanorods, as shown in the TEM images (Figure 2.2d). When Au @Pd_{0.01}PEGSHNRs were subjected to overgrowth, due to the universal distribution of Pd, the island growth showed no preference, and random deposition of islands on both sides and tips of the Au@Pd_{0.01}PEGSH NRs can be observed (Figure 2.2e). In the case of Au@Pd_{0.1}PEGSHNRs, the preferential deposition of Pd in the middle created two areas with significant strain difference. Although the Au-S bond also increased the interfacial energy between the newly deposited islands and the original Au surface, the crystal strain introduced by the lattice mismatch between Pd and Au was far more significant. As a result, the islands grown on the sides were etched during the ripening process and then redeposited onto islands on the tips. After overgrowth, Au@Pd_{0.1}PEGSHNRs islands deposited on the

exposed tips and formed dumbbell-like structures (Figure 2.2f). As shown in the UV-vis-NIR spectra (Figure 2.2c), the island growth modes had great influences on the optical properties of the overgrown nanorods. In the case of Au@Pd₀PEGSHNRs, the islands grew on the side of the nanorods, decreasing the aspect ratio of the nanorods. Therefore, a blue shift of the longitudinal peak was observed after island growth. When the islands were randomly deposited on the nanorods, the longitudinal peak of the overgrown nanorods was greatly broadened due to the non-uniform distance between islands. As for Au@Pd_{0.1}PEGSHNRs, the tip island growth increased the overall length of the nanorods; therefore, it resulted in a redshift of the longitudinal peak.

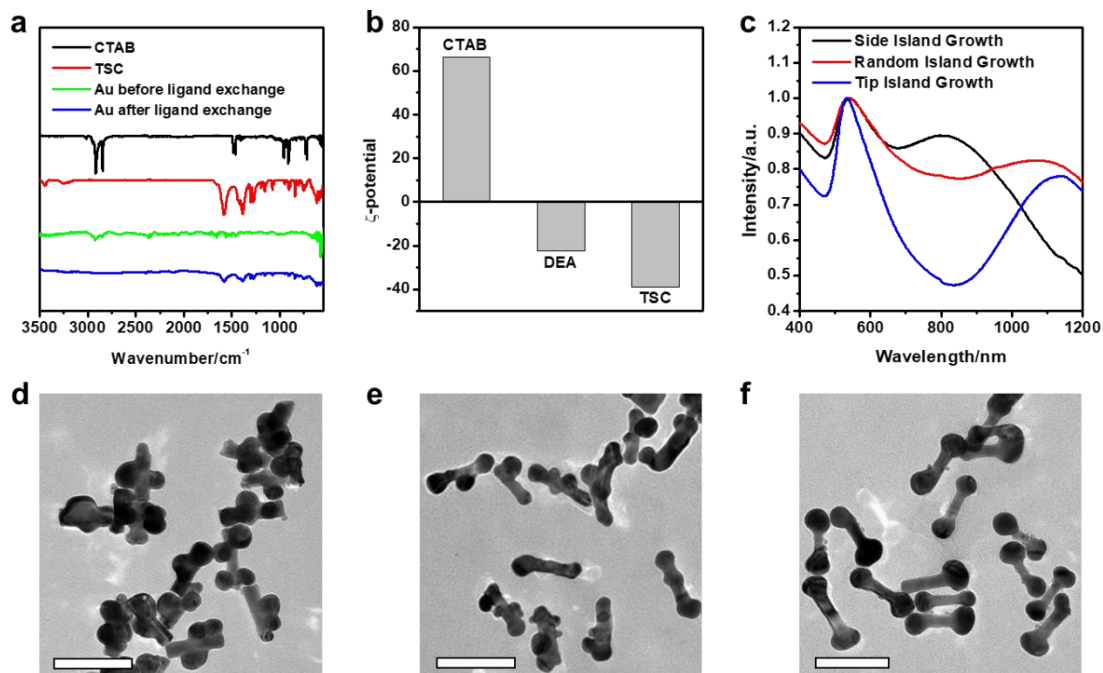


Figure 2.2 (a) FTIR spectra of CTAB, TSC, and Au@PdNRs before and after ligand exchange. (b) Zeta potential of the CTAB-stabilized Au@PdNRs before ligand exchanged and after ligand exchanged with DEA and TSC. (c) UV-vis-NIR spectra of the overgrown Au@PdNRs. (d-f) TEM images of island growth on (d) Au@Pd₀PEGSHNRs, (e) Au@Pd_{0.01}PEGSHNRs, and (f) Au@Pd_{0.1}PEGSHNRs. The scale bars are 50 nm.

To verify whether the selective Pd deposition originated from the thiol to Au binding or the steric hindrance provided by the polymers, we performed the selective island growth with modification of cysteine and mercaptoacetic acid, both of which are small molecules with thiol groups. As shown in Figure 2.3a and b, the dumbbell-like structures were obtained with modification of either cysteine or mercaptoacetic acid. This result showed that the selective Pd deposition could be achieved with thiol-containing chemicals, regardless of the molecule size. Therefore, the site-selective island growth should be attributed to the Au-S bond instead of the steric hindrance of the polymer. To further confirm our conclusion, we modified AuNRs with PEG terminated with an amino group (PEGNH₂) and performed Pd coating and overgrowth. As a result, only side island growth was observed in the TEM images (Figure 2.3c), suggesting that the distribution of Pd was not affected by PEGNH₂. Although PEGNH₂ has the same bulky polymer as PEGSH, the weak interaction between the amino group and Au surface cannot induce enough surface strain to influence the deposition of Pd; therefore, we can only obtain the same result as the case where AuNRs were not modified with any polymers.

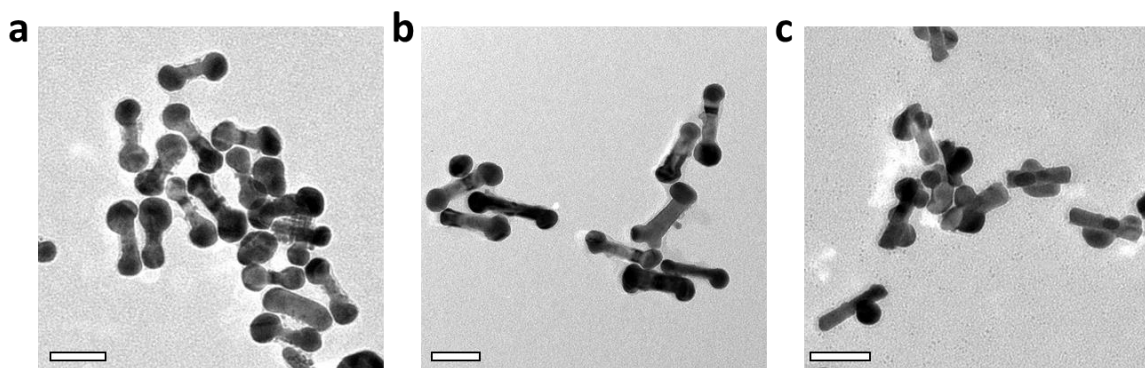


Figure 2.3 TEM images of island growth on Au@PdNRs using AuNRs modified with (a) cysteine, (b) mercaptoacetic acid, and (c) PEGNH₂. The scale bars are 50 nm.

To further investigate the surface strain difference induced by thiol group and Pd deposition, we prepared AuNRs completely modified with PEGSH (Au@PEGSHNRs) and Au@Pd₀PEGSHNRs and grew a small amount of Au on both nanorods (Figure 2.4a and c). Due to the increased overall surface stain, Au grew into small islands on both Au@PEGSHNRs and Au@Pd₀PEGSHNRs. The contact angle of small islands on Au@PEGSHNRs and Au@Pd₀PEGSHNRs showed distinct differences. As indicated in the statistic results in Figure 2.4c, the Au islands on Au@PEGSHNRs had relatively small contact angles (from 10° to 20°), while the typical contact angles of the small islands on Au@Pd₀PEGSHNRs ranged from 66° to 115°, with an average of 84.7° (Figure 2.4d). In an analog to wetting of liquids on a solid surface, the contact angle θ can be calculated by the equation:

$$\gamma_{sub} = \gamma_{interfacial} + \gamma_{island} \cos\theta \quad (2.2)$$

where γ_{sub} , $\gamma_{interfacial}$ and γ_{island} are the surface energies of the substrate, between the substrate and the islands and the islands, respectively. The higher contact angle indicates higher interfacial energy between the nanorod surface and the newly deposited Au islands. The contact angle difference between the small islands on both surfaces showed the strain difference induced by thiol modification and Pd coating.

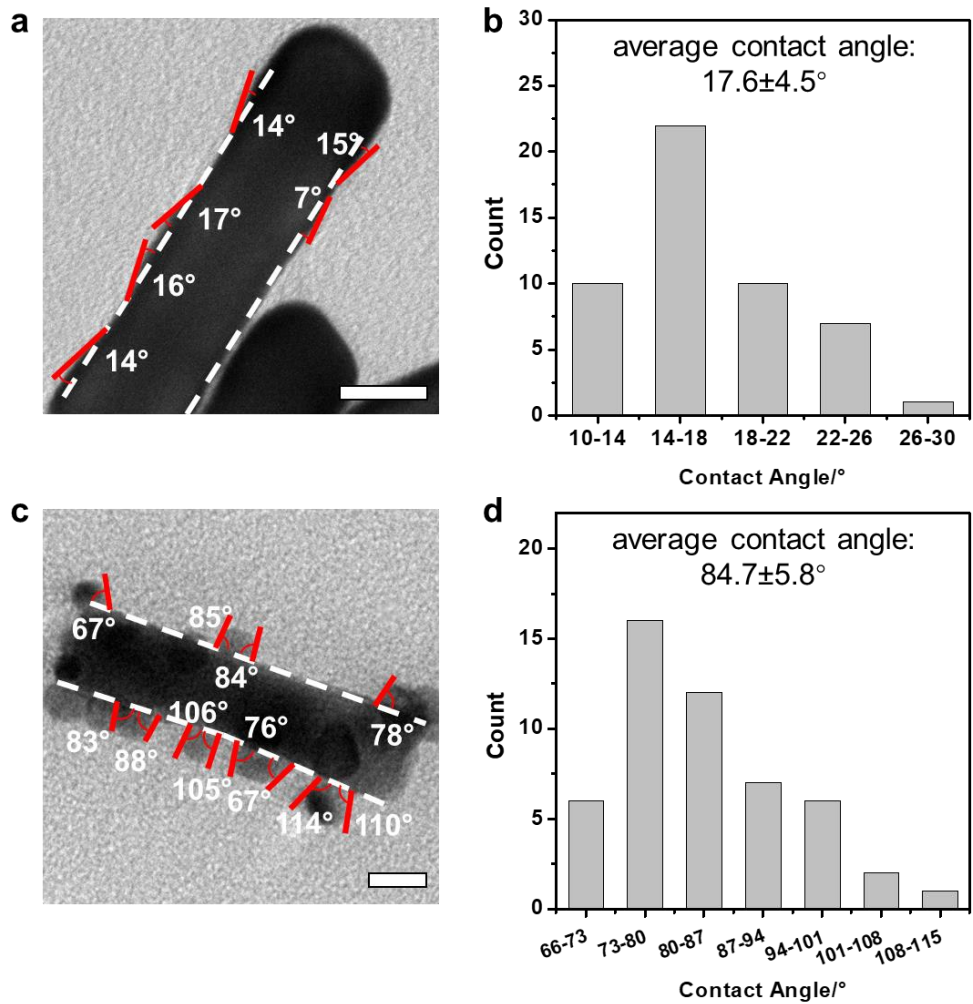


Figure 2.4 TEM images of small islands grown on (a) Au@PEGSHNRs and (c) Au@Pd₀PEGSHNRs. Statistic analysis of the contact angle of the small islands grown on (b) Au@PEGSHNRs and (d) Au@Pd₀PEGSHNRs.

2.3.2 Tuning of the Structural Features of Islands

As mentioned above, the I^- can promote the Ostwald ripening of small Au nanoparticles in seed-mediated synthesis by forming I_3^- to oxidize Au nanoparticles according to reactions below:



In this work, we varied the I^- to $HAuCl_4$ ratio in the growth solution to control the number of islands grown on a single nanorod. As shown in Figure 2.5a and b, we achieved the growth of multiple islands or a single island on each $Au@Pd_{0.1}PEGSHNR$ by controlling the KI to $HAuCl_4$ in the growth solution. With a high KI ratio, the oxidative etching of small islands with higher surface energies was greatly accelerated, and fewer islands would survive from the etching. Once Au redeposited on one of the islands, it became a preferred deposition site, and Au would further deposit on the same island, resulting in the growth of a single island on the nanorod. In the cases with anisotropic PEGSH modification, due to the overall excess energy on the PEGSH modified tips, the deposition of Au on the tips will be preferred. With a $KI/HAuCl_4$ ratio of 10, islands would grow on both sites with an equal chance, and the typical dumbbell-like structures could be obtained (Figure 2.2f). When the overgrowth was performed without the addition of KI , an overall overgrowth of $Au@Pd_{0.1}PEGSHNRs$ can be observed (Figure 2.5c). It is interesting to find in the magnified images of overgrown $Au@Pd_{0.1}PEGSHNRs$ without KI addition (Figure 2.5d) that the overgrown nanorods can be clearly divided into two regions; the tips modified with PEGSH

grew into smooth crystals and showed clear facets. On the other hand, the overgrown crystal in the middle had rough surfaces, showing the characteristics of island growth. The different crystal growth behavior on tips and sides of the nanorods is another evidence of the surface strain difference between the PEGSH modified tips and Pd covered side. When a low KI ratio was added in the growth solution ($KI/HAuCl_4=5$), the etching of small islands was relatively slow, giving a higher chance to preserve more growth sites. As a result, the appearance of a third island can be observed in the middle of the nanorods, as shown in Figure 2.5e. When KI to $H AuCl_4$ ratio was increased to 40, the oxidative etching was greatly promoted, we started to see island growth on only one tip of the nanorods (Figure 2.5f).

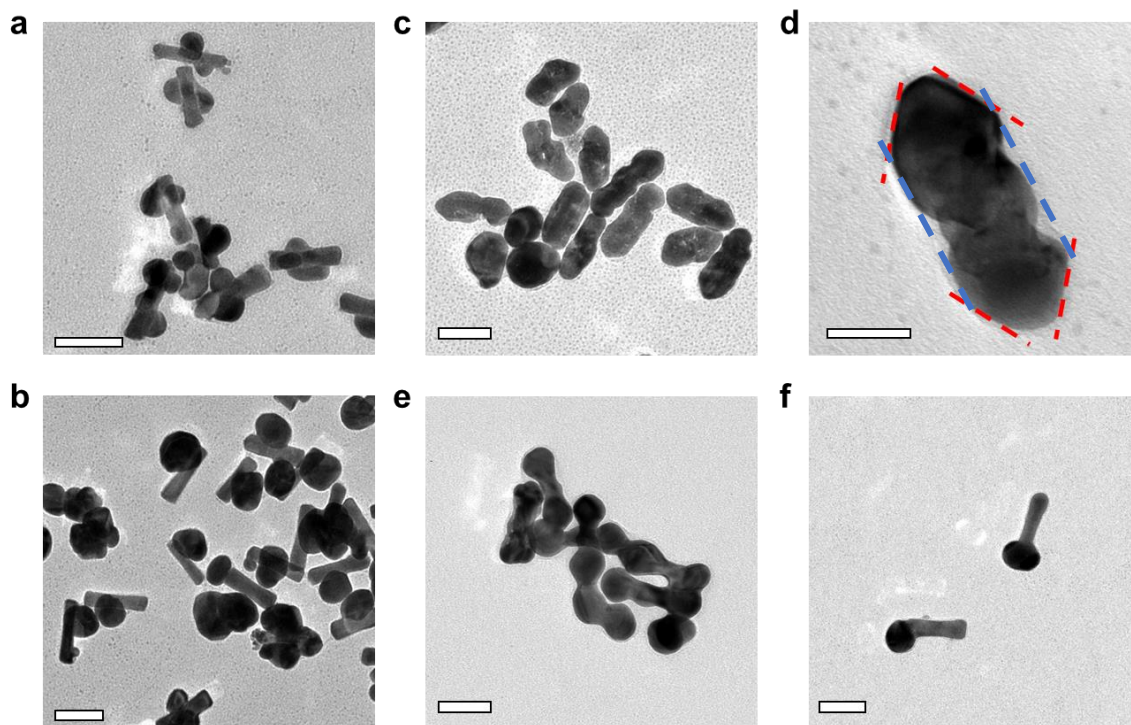


Figure 2.5 TEM images of island growth on Au@Pd₀PEGSHNRs with KI/HAuCl₄ ratio of (a) 10 and (b) 40 and on Au@Pd_{0.1}PEGSHNRs with KI/HAuCl₄ ratio of (c-d) 0, (e) 10 and (f) 40. Scale bars in (a-c) and (e-f) are 50 nm. Scale bar in (d) is 20 nm.

From the UV-vis-NIR spectra, we can see the LSPR peak of as-prepared dumbbell-like Au nanorods (AuDBs) located at 1144 nm, falling in the NIR-II window for the photothermal therapy applications. Although the synthesis of dumbbell-like structures has been reported before and the potential in photothermal therapies has been proved,²⁴ the fine-tuning of plasmonic resonance wavelength to match the laser wavelength is still hard to achieve due to the lack of tuning parameters in the kinetically controlled synthesis. Our selective PEGSH modification and Pd deposition strategy greatly amplified the surface strain difference between tips and sides originated from the packing density difference of CTAB, therefore, creating a robust template similar to hard templates such as SiO₂. The main difference between the two strategies is that instead of physical blockage, which results in a fixed structure, the surface strain difference offers more flexibility since the surface strain of each region can be changed to produce more complex results. There are several morphology features of prepared AuDBs that can be tuned to change the optical properties at different levels. For example, the size of the overgrown tips contributed greatly to the peak position of the longitudinal peak of the AuDBs. By adjusting the amount of growth solution added into the system, the size of the overgrown tips can be varied (Figure 2.6a-d). And as seen in the UV-vis-NIR spectra (Figure 2.6e), the longitudinal peaks of the AuDBs redshifted with increasing tip sizes. The peak of the AuDBs was very sensitive to the size of the tips and showed a nearly linear increase with increasing tip sizes (Figure 2.6f). The LSPR peak can be tuned in a wide range from 930 nm to 1144 nm by simply changing the growth solution amount.

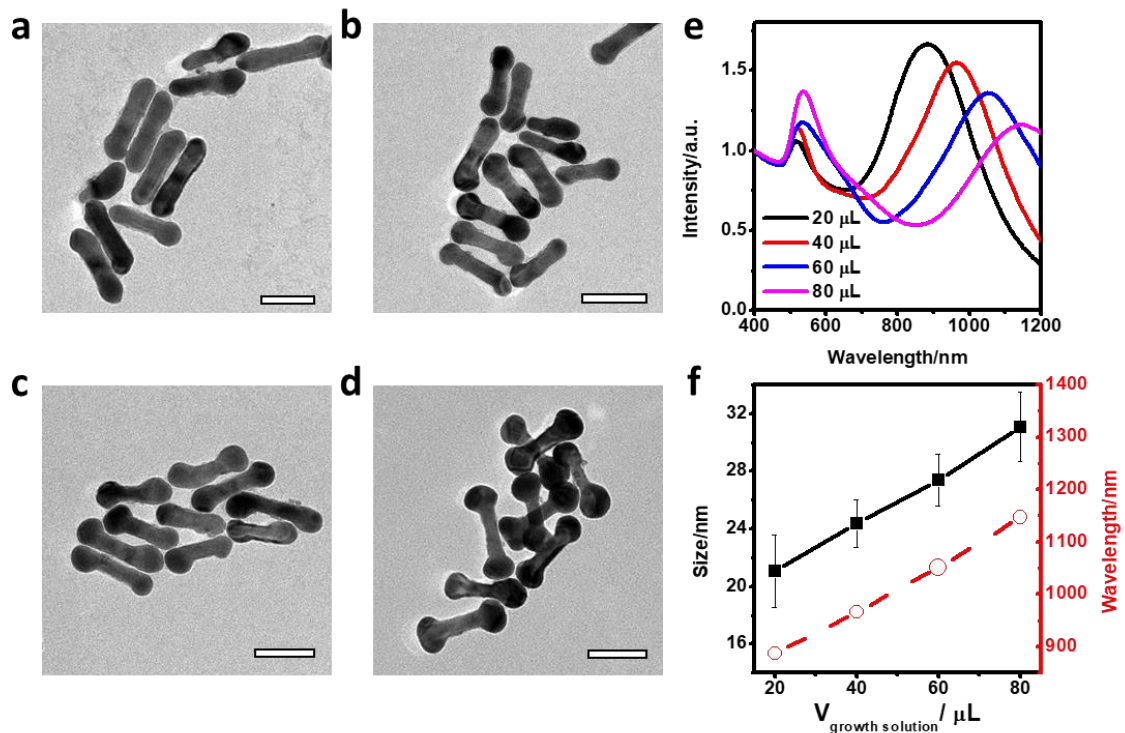


Figure 2.6 (a-d) TEM images of AuDBs synthesized with (a) 20 μL , (d) 40 μL , (c) 60 μL and (d) 80 μL of growth solution. Scale bars are 50 nm. (e) UV-vis-NIR spectra of AuDBs synthesized with different amounts of growth solution added. (f) Evolution of the size of islands and the longitudinal LSPR peak wavelength with respect to growth solution amount.

The next level of optical tuning comes from the distance between the two islands. The PEGSH/Au ratio can be used to control the coverage of Pd on AuNRs, thus influences the distance between the two overgrown tips. More specifically, with increasing PEGSH/Au ratio during the anisotropic modification, more areas will be modified with PEGSH. Therefore, the area available for Pd deposition was smaller. As a result, during overgrowth, the distance between two overgrown tips was reduced. The TEM images (Figure 2.7a-d) confirmed the decreasing tip distances between with increasing PEGSH ratio. As demonstrated in Figure 2.7e, the distance between islands showed a steady decreasing trend proportional to the PEGSH ratio, while the overall length of the AuDBs showed a smaller decrease. The UV-vis-NIR spectra of the as-prepared AuDBs blueshifted with increasing PEGSH ratio due to the decreased distance between two islands, as shown in Figure 2.7f. Simulation results (Figure 2.7g) also confirmed that, with the same overall length, a decrease in island distance would result in a blue shift of the longitudinal peak of AuDBs. By comparing the simulated electric field distribution around AuDBs (Figure 2.7h-k) with different distances between two islands, we hypothesized that blue shift resulted from the decrease in effective dipole distance with decreasing island distances. The island distance on overgrown nanorods offered another tuning wedge at a finer scale, and the longitudinal peak of AuDBs can be tuned from 1095 nm to 1151 nm with the same growth solution amount.

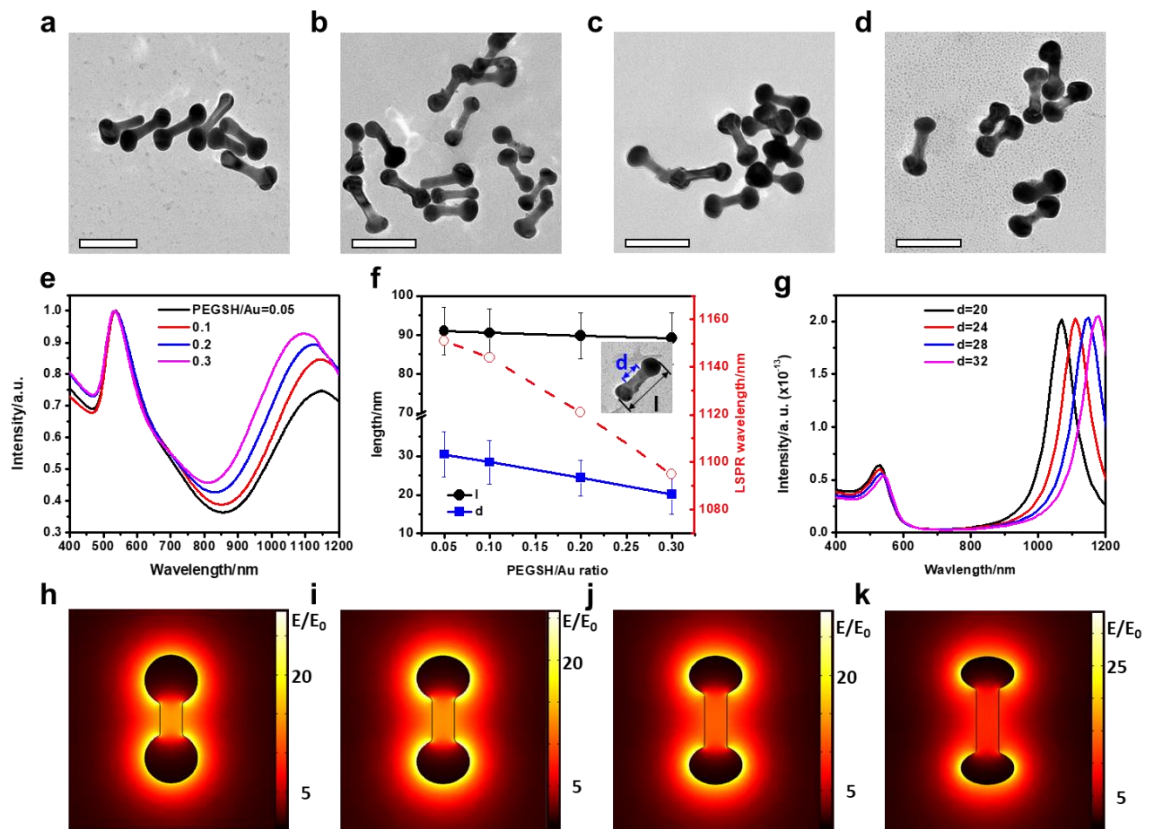


Figure 2.7 (a-d) TEM images of AuDBs synthesized with PEGSH/Au ratio of (a) 0.05, (b) 0.1, (c) 0.2 and (d) 0.3. Scale bars are 50 nm. (e) UV-vis-NIR spectra of AuDBs synthesized with different PEGSH/Au ratios. (f) Evolution of distance between islands, d , overall length, l , and the wavelength of longitudinal peaks with respect to PEGSH/Au ratio. Simulated results of (g) spectra and (h-k) electric field distribution of AuDBs with d ranging from 20 nm to 32 nm at their resonance wavelengths.

The plasmonic peak of the AuDBs can be further tuned by controlling the wetting degree of the islands. As illustrated above, the site selectivity originated from the surface strain difference between the thiol modified tips and the Pd coated side. PVP as a surfactant can reduce the surface strain difference between the two regions, therefore, changing the wetting degree of the islands on the AuNRs. As shown in Figure 2.8a-d, with increasing PVP concentration, the curvature at the connection of the islands and the AuNRs gradually decreased. Interestingly, when there was no PVP added to the system (Figure 2.8a), island growth was only observed on one tip of the nanorods. The addition of PVP stabilized the newly grown small islands, therefore, reducing the oxidative etching process. As shown in Figure 2.9b, when KI was added into 2-3 nm Au seeds, the Au seeds ripened into large particles after stirring for 1 h, and a sharp peak corresponding to Au nanoparticles can be observed in the UV-vis spectrum (Figure 2.9h). With the addition of PVP, the ripening of the Au seeds was greatly reduced. The spectra of Au seeds were much broader than the Au seeds aged without PVP. Furthermore, the TEM images (Figure 2.9c-f) also showed that when PVP concentration was higher than 0.1%, the obtained particles after aging were much smaller in size. With increasing PVP concentration, the Au seeds showed a decreasing trend in size (Figure 2.9g), and the plasmonic peaks of aged Au seeds became much broader, proving the protecting role of PVP during the ripening process. Similar to lowering the KI ratio, the addition of PVP reduced the oxidative etching process, allowing the deposition of Au on both tips of the nanorods. As shown in the spectra of AuDBs synthesized with PVP concentration at 0.01%, 0.1%, and 2.5% (Figure 2.8e), the descending curvature resulted in a slight blue shift in the LSPR peak of AuDBs, which

matched with the simulation results obtained with the measured dimensions (Figure 2.8f). By comparing the electric field distribution of AuDBs with the radius of curvature at the connection of 2 nm and 18 nm, we found the enhanced electric field distributed more evenly toward the center of the dumbbell structure, resulting in a decrease in the distance between effective dipoles. The wetting degree of islands offered the tuning of plasmonic properties of AuDBs with higher precision. As shown in Figure 2.10, the island size, distance, and wetting degree offered the tuning of LSPR peaks of AuDBs at different levels. Our templating strategy combined the advantages of hard templates, which allowed highly reproducible products, and the flexibility of kinetically controlled synthesis, and achieved a precise morphology tuning of AuDBs. By combining the three key factors of AuDBs (tip size, distance, and wetting degree), the LSPR peak of the AuDBs can be tuned with high precision while maintaining a wide tuning range, which allowed the tailoring of AuDBs to match the laser wavelength for various applications.

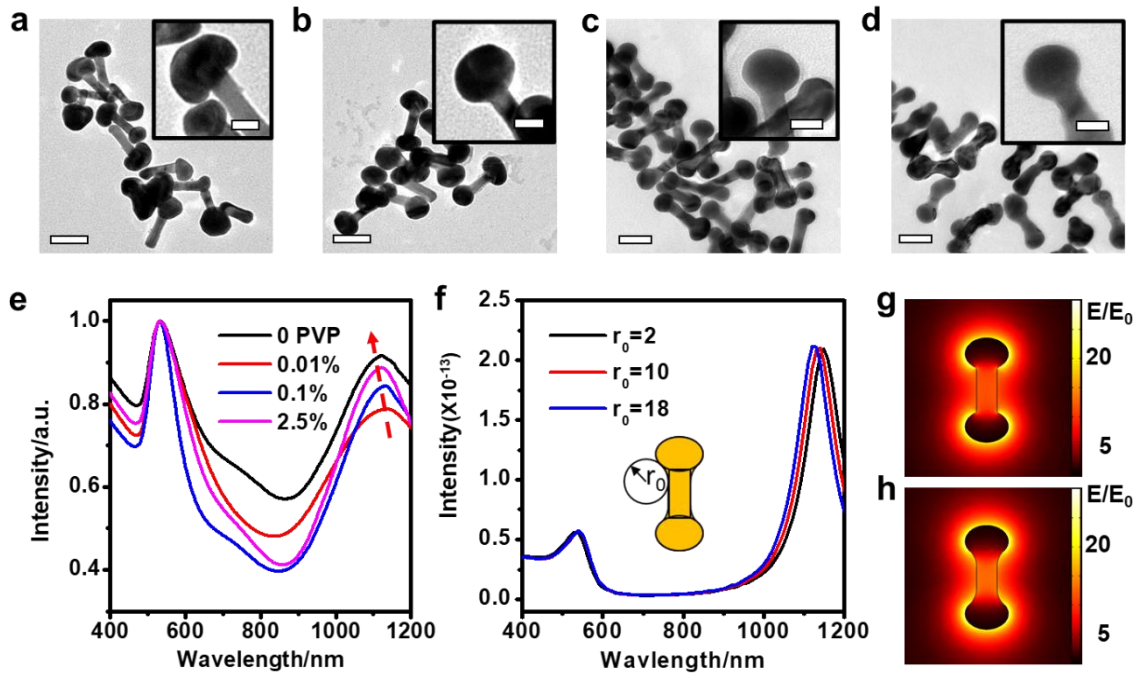


Figure 2.8 (a-d) TEM images of AuDBs synthesized with presence of (a) 0%, (b) 0.01%, (c) 0.1% and (d) 2.5% PVP. Scale bars are 50 nm. Insets are magnified images at the connection of the island and nanorods. Scale bars in insets are 20 nm. (e) UV-vis-NIR spectra of AuDBs synthesized with different PVP concentration. Simulated results of (f) spectra of AuDBs with curvature radius at the connection of 2, 10, and 18 nm, and electric field distribution of AuDBs with a curvature radius of (g) 2 nm and (h) 18 nm at their resonance wavelength.

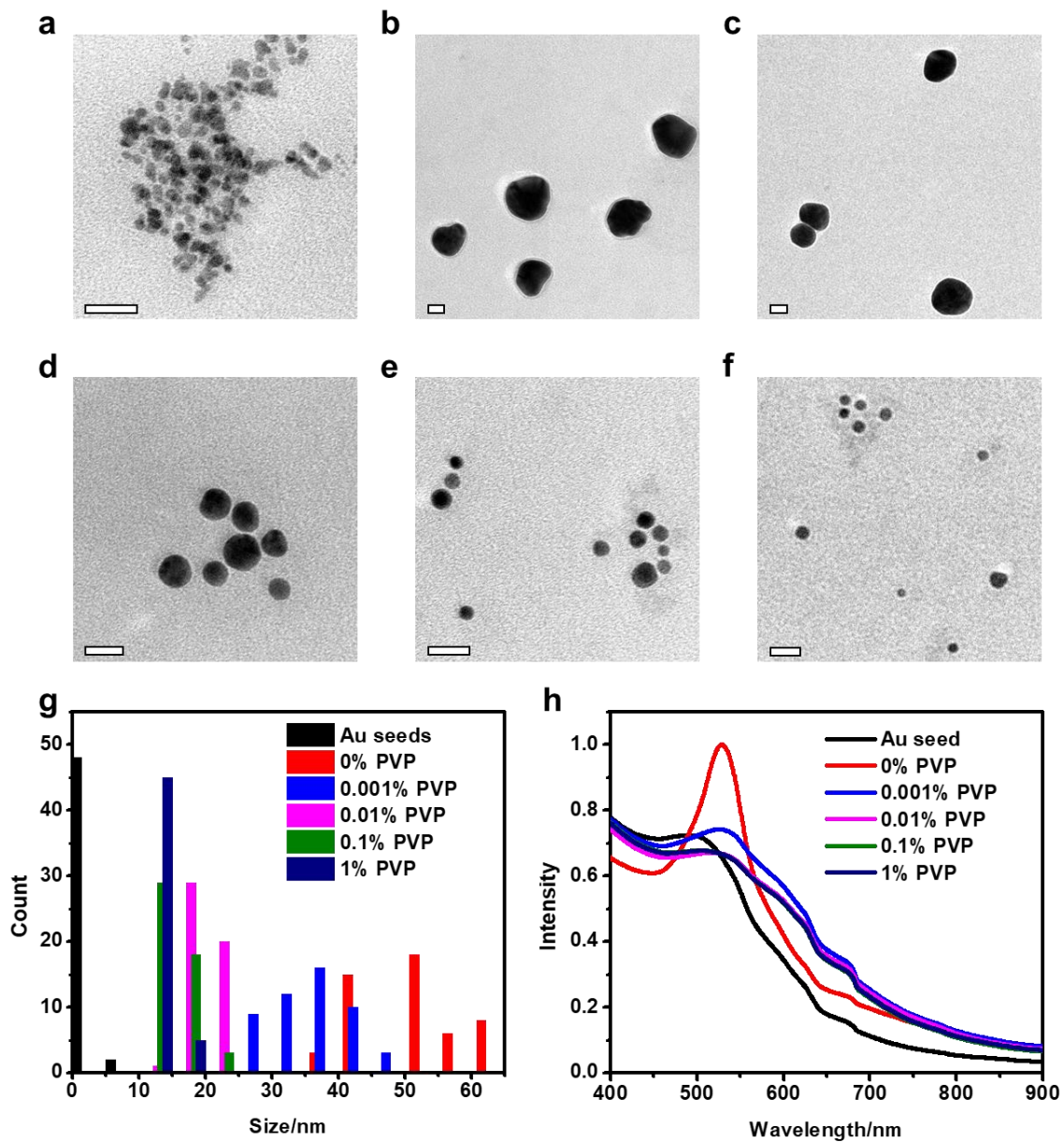


Figure 2.9 (a-f) TEM images of Au seeds (a) before aging and after aging with presence of (b) 0%, (c) 0.001%, (d) 0.01%, (e) 0.1% and (f) 1% PVP for 1 h. (g) Size distribution and (h) UV-vis spectra of Au seeds before and after aging with different PVP concentration.

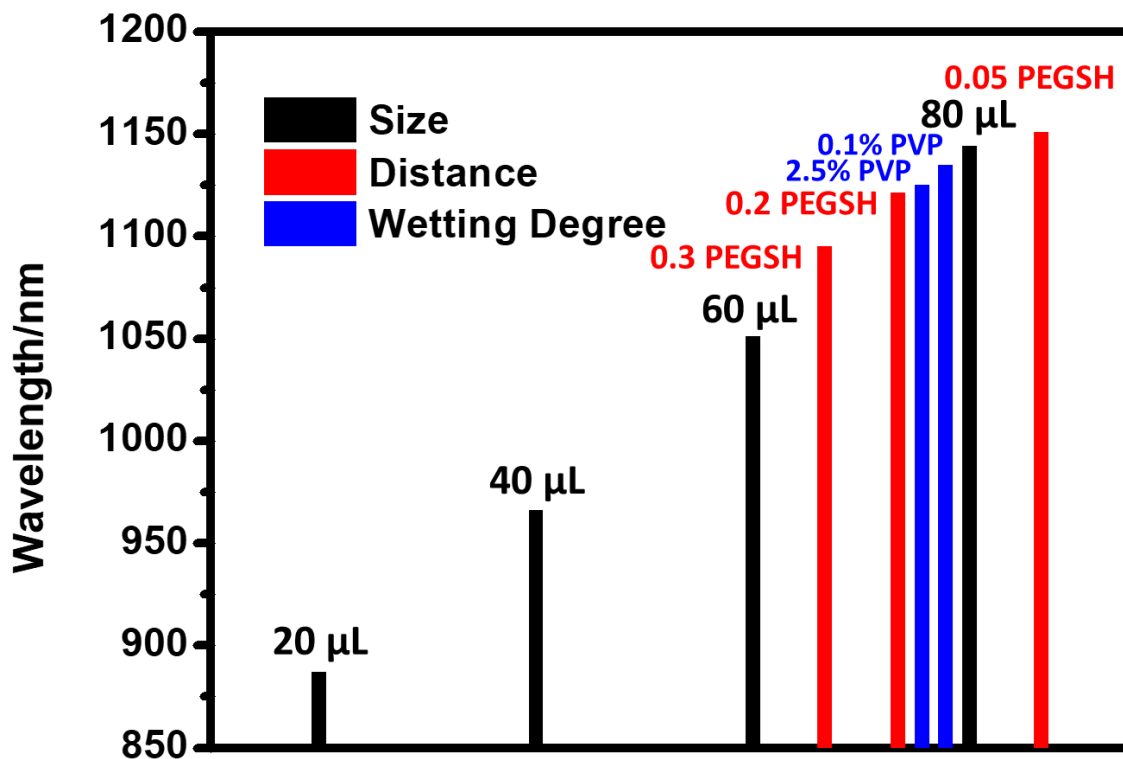


Figure 2.10 Systematic tuning of LSPR peak of AuDBs at different tuning scales through the control of island size, distance, and wetting degree.

2.3.3 Site-Selective Island Growth on Other Au Nanostructures

In addition to the spectral tuning of the AuDBs, we also explored the possibility of expanding the site-selective island growth strategy to other anisotropic Au nanostructures. It is reasonable to assume that the principle of the anisotropic modification of PEGSH based on packing density difference between the tips and the sides can be expanded to most halide capped Au nanostructures. Therefore, the site-selective island growth was carried out on other Au nanostructures (Au nanoplates [AuPLTs], nanocubes [AuCBs], and rhombic dodecahedrons [AuRDs]). As shown in Figure 2.11, the selective island growth on the faces and the corners of the AuCBs can be achieved with our proposed procedures. The AuCBs were synthesized with the presence of CTAC as a surfactant, and therefore, the packing density of CTAC on the sides of the AuCBs is higher than that on the tips and edges. Without PEGSH modification, the island growth would be limited on the faces of the AuCBs, while island growth on the tips was achieved with PEGSH modification at a PEGSH/Au ratio of 0.1.

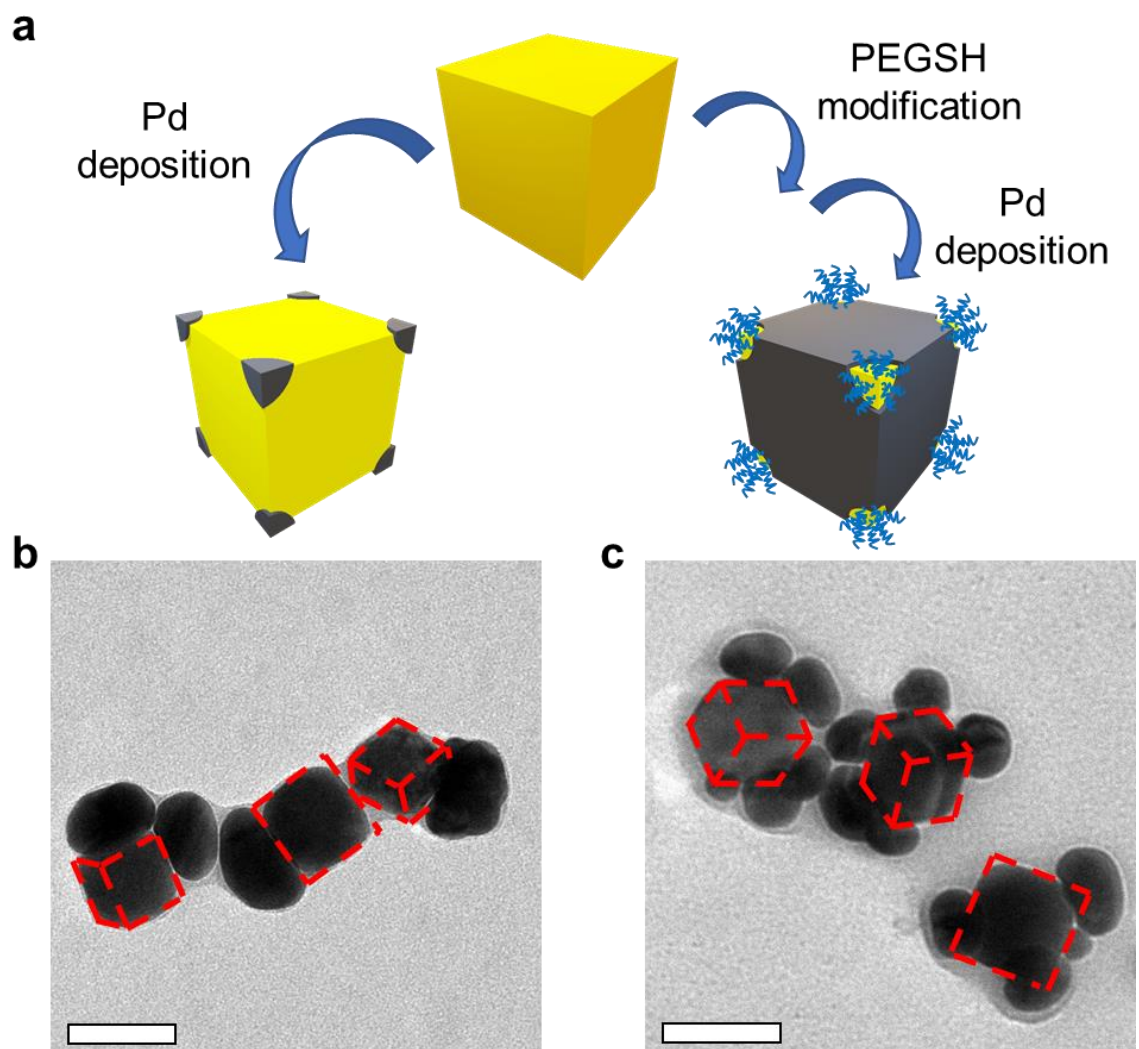


Figure 2.11 (a) Schematics showing the tuning of island growth on the faces and the tips of AuCBs. TEM image of island growth on (b) the faces and (c) the tips of AuCBs, the dashed lines indicated the edges of the nanocubes.

As shown in Figure 2.12, the site-selective island growth can be achieved in CTAC-capped AuPLTs (Figure 2.12b-d), AuCBs (Figure 2.12f-h), and AuRDs (Figure 2.12j-l). The number of islands can also be controlled by manipulating the ripening process of the small islands. Although the precise control of the numbers of islands was not obtained, the statistical results of the numbers of islands showed a clear decreasing trend with increasing KI/HAuCl₄ ratios (Figure 2.12e, i and m). Due to the difficulties of visualizing the islands on nanocubes and rhombic dodecahedrons, we built 3D models to match with the TEM projections from different viewing angles to better demonstrate the structures. The SEM images of overgrown rhombic dodecahedrons (Figure 2.13) also confirmed the proposed structures in the 3D models. The successful site-selective island growth on other Au nanostructures proved the versatility of our method, and the template design principle based on the surface strain opened more opportunities in the synthesis of novel nanostructures.

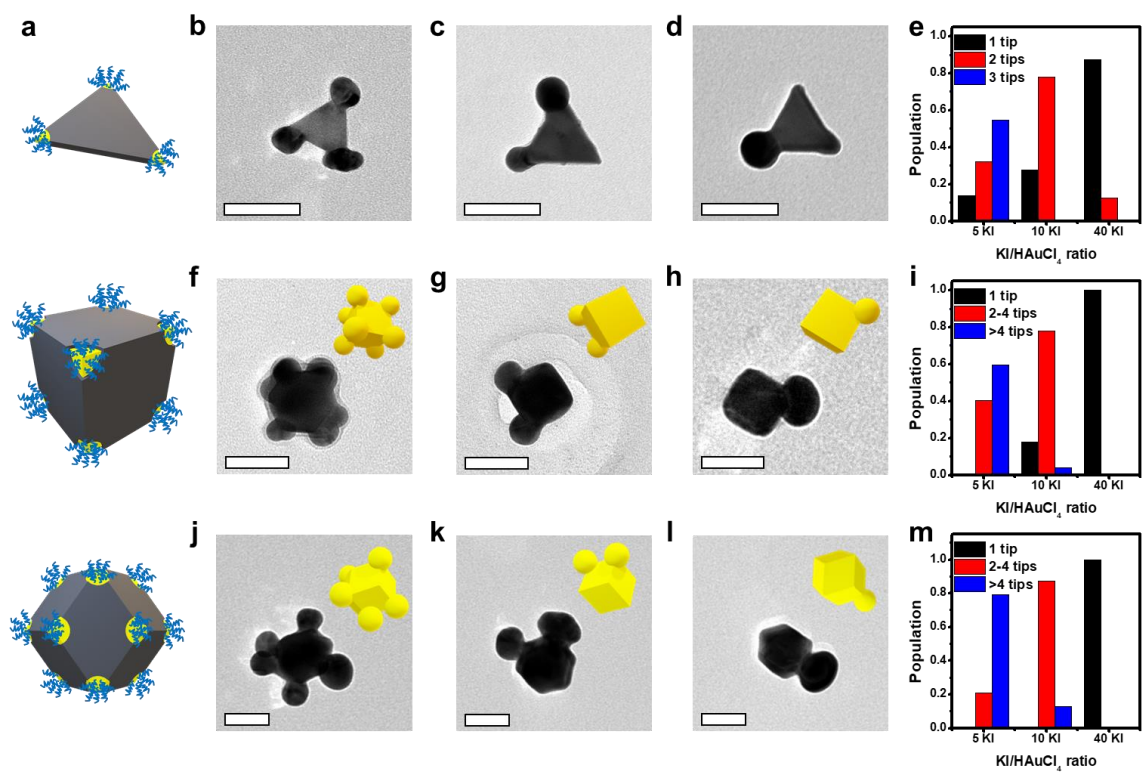


Figure 2.12 (a) Schematics showing the Au@Pd seeds used for island growth. TEM images of island growth on (b-d) AuPLTs, (f-h) AuCBs and (j-l) AuRDs with KI/HAuCl₄ ratio of (b, f, j) 5, (c, g, k) 10 and (d, h, l) 40. Scale bars are 50 nm. Insets in (f-h) and (j-l) are 3D models of corresponding particles. Statistic analysis of numbers of islands grown on (e) AuPLTs, (i) AuCBs, and (m) AuRDs with different KI/HAuCl₄ ratio.

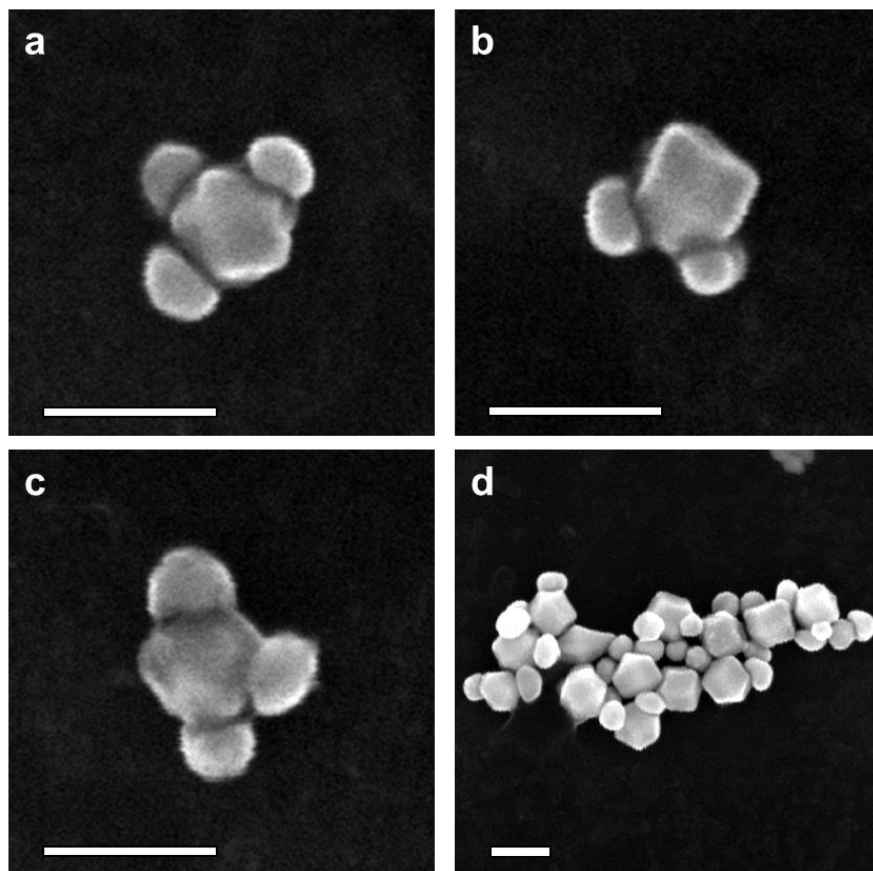


Figure 2.13 SEM images of overgrown Au@PdRDs. Scale bars are 100 nm.

2.4 Conclusion

In this work, we demonstrated a templating strategy by creating regions with different surface strains, which determined the location of island deposition on anisotropic Au nanostructures. The structural features of islands, including number, size, coverage, and wetting degree, can be systematically controlled thanks to the flexibility of the template created by surface strain difference. Our method established a comprehensive protocol for the fine-tuning of the island growth products, allowing the tailoring of novel Au nanostructures for specific requirements. In addition, we demonstrated that the site-selective island growth is versatile and can be extended to other Au nanostructures (nanoplates, nanocubes, and rhombic dodecahedrons), and the number of islands can also be controlled by controlling the ripening process. Furthermore, the principle of surface strain patterning could be employed in other crystal growth systems and bring new opportunities to the synthesis of novel nanocrystals.

2.5 Reference

1. Zhang, Z.; Zhang, C.; Zheng, H.; Xu, H., Plasmon-Driven Catalysis on Molecules and Nanomaterials. *Accounts of Chemical Research* **2019**, *52* (9), 2506-2515.
2. Li, M.; Cushing, S. K.; Wu, N., Plasmon-enhanced optical sensors: a review. *The Analyst* **2015**, *140* (2), 386-406.
3. Ibarra, M. R.; Khlebtsov, N. G., Magnetic and Plasmonic Nanoparticles for Biomedical Devices. *Journal of Applied Physics* **2019**, *126* (17), 170401.
4. Khlebtsov, N. G.; Dykman, L. A., Optical properties and biomedical applications of plasmonic nanoparticles. *Journal of Quantitative Spectroscopy and Radiative Transfer* **2010**, *111* (1), 1-35.
5. Tao, A. R.; Habas, S.; Yang, P., Shape Control of Colloidal Metal Nanocrystals. *Small* **2008**, *4* (3), 310-325.
6. Xia, Y.; Gilroy, K. D.; Peng, H.-C.; Xia, X., Seed-Mediated Growth of Colloidal Metal Nanocrystals. *Angewandte Chemie International Edition* **2017**, *56* (1), 60-95.
7. Huang, X.; Neretina, S.; El-Sayed, M. A., Gold Nanorods: From Synthesis and Properties to Biological and Biomedical Applications. *Advanced Materials* **2009**, *21* (48), 4880-4910.
8. Polte, J., Fundamental growth principles of colloidal metal nanoparticles – a new perspective. *CrystEngComm* **2015**, *17* (36), 6809-6830.
9. Jia, J.; Liu, G.; Xu, W.; Tian, X.; Li, S.; Han, F.; Feng, Y.; Dong, X.; Chen, H., Fine-Tuning the Homometallic Interface of Au-on-Au Nanorods and Their Photothermal Therapy in the NIR-II Window. *Angewandte Chemie International Edition* **2020**, *59* (34), 14443-14448.
10. Huang, J.; Zhu, Y.; Liu, C.; Shi, Z.; Fratolocchi, A.; Han, Y., Unravelling Thiol's Role in Directing Asymmetric Growth of Au Nanorod–Au Nanoparticle Dimers. *Nano Letters* **2016**, *16* (1), 617-623.
11. Lee, H.-E.; Kim, R. M.; Ahn, H.-Y.; Lee, Y. Y.; Byun, G. H.; Im, S. W.; Mun, J.; Rho, J.; Nam, K. T., Cysteine-encoded chirality evolution in plasmonic rhombic dodecahedral gold nanoparticles. *Nature Communications* **2020**, *11* (1), 263.
12. Ma, Y.; Cao, Z.; Hao, J.; Zhou, J.; Yang, Z.; Yang, Y.; Wei, J., Controlled Synthesis of Au Chiral Propellers from Seeded Growth of Au Nanoplates for Chiral Differentiation of Biomolecules. *The Journal of Physical Chemistry C* **2020**, *124* (44), 24306-24314.

13. Tan, R. L. S.; Chong, W. H.; Feng, Y.; Song, X.; Tham, C. L.; Wei, J.; Lin, M.; Chen, H., Nanoscrews: Asymmetrical Etching of Silver Nanowires. *Journal of the American Chemical Society* **2016**, *138* (34), 10770-10773.
14. Wang, Z.; He, B.; Xu, G.; Wang, G.; Wang, J.; Feng, Y.; Su, D.; Chen, B.; Li, H.; Wu, Z.; Zhang, H.; Shao, L.; Chen, H., Transformable masks for colloidal nanosynthesis. *Nature Communications* **2018**, *9* (1), 563.
15. Feng, Y.; He, J.; Wang, H.; Tay, Y. Y.; Sun, H.; Zhu, L.; Chen, H., An Unconventional Role of Ligand in Continuously Tuning of Metal–Metal Interfacial Strain. *Journal of the American Chemical Society* **2012**, *134* (4), 2004-2007.
16. Feng, Y.; Wang, Y.; He, J.; Song, X.; Tay, Y. Y.; Hng, H. H.; Ling, X. Y.; Chen, H., Achieving Site-Specificity in Multistep Colloidal Synthesis. *Journal of the American Chemical Society* **2015**, *137* (24), 7624-7627.
17. Ni, W.; Kou, X.; Yang, Z.; Wang, J., Tailoring Longitudinal Surface Plasmon Wavelengths, Scattering and Absorption Cross Sections of Gold Nanorods. *ACS Nano* **2008**, *2* (4), 677-686.
18. Chen, L.; Ji, F.; Xu, Y.; He, L.; Mi, Y.; Bao, F.; Sun, B.; Zhang, X.; Zhang, Q., High-Yield Seedless Synthesis of Triangular Gold Nanoplates through Oxidative Etching. *Nano Letters* **2014**, *14* (12), 7201-7206.
19. Kuo, B.-H.; Hsia, C.-F.; Chen, T.-N.; Huang, M. H., Systematic Shape Evolution of Gold Nanocrystals Achieved through Adjustment in the Amount of HAuCl₄ Solution Used. *The Journal of Physical Chemistry C* **2018**, *122* (43), 25118-25126.
20. Wang, F.; Cheng, S.; Bao, Z.; Wang, J., Anisotropic Overgrowth of Metal Heterostructures Induced by a Site-Selective Silica Coating. *Angewandte Chemie International Edition* **2013**, *52* (39), 10344-10348.
21. Sun, Z.; Ni, W.; Yang, Z.; Kou, X.; Li, L.; Wang, J., pH-Controlled Reversible Assembly and Disassembly of Gold Nanorods. *Small* **2008**, *4* (9), 1287-1292.
22. Liu, K.; Zhao, N.; Kumacheva, E., Self-assembly of inorganic nanorods. *Chemical Society Reviews* **2011**, *40* (2), 656-671.
23. DeSantis, C. J.; Weiner, R. G.; Radmilovic, A.; Bower, M. M.; Skrabalak, S. E., Seeding Bimetallic Nanostructures as a New Class of Plasmonic Colloids. *The Journal of Physical Chemistry Letters* **2013**, *4* (18), 3072-3082.
24. Yin, J.; Wu, H.; Wang, X.; Tian, L.; Yang, R.; Liu, L.; Shao, Y., Plasmonic nano-dumbbells for enhanced photothermal and photodynamic synergistic damage of cancer cells. *Applied Physics Letters* **2020**, *116* (16), 163702.

Chapter 3 Magnetic Tuning of Plasmonic Nanoparticles

3.1 Magnetic Tuning of Au-Au/Au-Ag Dimers

3.1.1 Introduction

As discussed in Chapter 1, the anisotropic nanoparticles such as nanorods and dimers have two plasmonic modes corresponding to the excitation along the longitudinal and the transverse axis. When the incident light is linearly polarized, the two modes can be individually excited when the polarization of the incident light aligns with the corresponding axis of the nanoparticle geometry. The angular dependence of the anisotropic plasmonic nanostructures can serve as an additional dimension in the optical responses of the plasmonic-based devices such as data encryption,¹ photothermal actuator²⁻³ signal modulation,⁴⁻⁵ and anti-counterfeiting devices.⁶ By forming a magnetic/plasmonic composite, the remote and large-scale control of nanoparticles can be achieved with an external magnetic field, thus allows the dynamic tuning of the optical properties.⁵⁻⁷ As demonstrated previously in our group,⁵ the AuNRs can be attached on Fe₃O₄@SiO₂ nanorods to achieve the selective excitation of the longitudinal and transverse mode of the AuNRs, and it was demonstrated that such phenomenon could be used to modulate the intensity of the linearly polarized light at the resonant wavelengths. However, as we pointed out, the surface of the AuNRs has to be negatively charged to have sufficient interaction with the amino group modified on the Fe₃O₄@SiO₂ nanorods' surface. In addition, the composites had to be kept at a low concentration to prevent the aggregation of the nanoparticles. These two factors limited the application of the plasmonic/magnetic composites. Furthermore, to ensure the side-by-side attachment of the plasmonic and the

magnetic component, the two parts should have similar size and morphology. However, due to the limited well-defined anisotropic magnetic nanoparticles, the choice of plasmonic nanoparticles was limited. Although the synthesis plasmonic/magnetic nanocomposites can be obtained by synthesizing $\text{Fe}_3\text{O}_4@Au$ core-shell nanoparticles,⁸ the size of the overall nanostructures were relatively large. In addition, the morphologies obtained from the core-shell structures were still limited by the shape of the magnetic components.

In this work, we demonstrated the synthesis of the self-registered Au-Au and Au-Ag dimer on $\text{Fe}_3\text{O}_4@SiO_2$ nanorods to achieve the dynamic magnetically controlled selective excitation of the longitudinal modes of the dimers. As pointed out in Chapter 1, the key in the synthesis of anisotropic nanoparticles is symmetry breaking. In this work, the Au-Au and Au-Ag dimers were synthesized with a partial passivation method, as shown in Figure 3.1a. The Au nanoparticles were first attached to the substrates modified with amino groups, and a layer of SiO_2 was coated on the substrate. Due to the low affinity between Au surface and SiO_2 , the SiO_2 will only coat on the SiO_2 substrates, and Au will be exposed for the following seed-mediated growth. The exposed area of the Au nanoparticles can be controlled with SiO_2 thickness. During the seed-mediated growth, SiO_2 serves as a symmetry breaker and prevents the growth of Au on the coated areas, resulting in the formation of a dimer structure and determined the overlapping degree of the two particles in the Au-Au or Au-Ag dimers. With a thicker SiO_2 coating, less Au will be exposed; therefore, the overlapping degree will be smaller, leading to a higher aspect ratio. Similar to AuNRs, Au dimers also exhibit two plasmonic modes corresponding to the longitudinal and transverse modes.⁹ Due to the unique synthetic strategy, the

longitudinal axis of the dimers was always perpendicular to the substrate surface, giving us a chance to tune the orientation of the dimers at a large scale. We also demonstrated the fabrication of the anti-counterfeiting films patterned with different nanocomposite orientations. In combination with the optical properties of the Fe₃O₄ nanorods, patterns with areas sensitive and insensitive to incident light polarization direction can be incorporated in one film, producing complex pattern designs suitable for anti-counterfeiting applications.

3.1.2 Experimental

3.1.2.1 Chemicals

Tetraethylorthosilicate (TEOS), poly(vinylpyrrolidone) (PVP, Mw=10,000), 3-amino-propyltriethoxysilane (APTES), potassium iodide (KI), L-ascorbic acid (AA), sodium borohydride (NaBH₄, 99%), sodium hydroxide (NaOH), chloroauric acid (HAuCl₄), polyacrylic acid (PAA, average M.W.=1800), trisodium citrate (TSC), acrylamide, 2-hydroxy-4'-(2-hydroxyethoxy)-2-methyl-propionophenone, and N,N'-methylene-bis(acrylamide) (purity 98%) were purchased from Sigma-Aldrich. Ammonium hydroxide (NH₃·H₂O, 28% by weight in water) and hydrochloric acid (HCl, 37%) were purchased from Fisher Scientific. Iron (III) chloride anhydrous (FeCl₃, 98%) was purchased from Alfa Aesar. Ethanol (200 proof) was purchased from Decon Laboratories Inc. All chemicals were directly used without further purification.

3.1.2.2 Synthesis of Fe₃O₄@SiO₂ Nanorods

The FeOOH nanorods were first synthesized with a previously published method.¹⁰ The synthesis of FeOOH nanorods was based on a previous report with some

modifications. Typically, 19.464 g of anhydrous FeCl_3 was dissolved in 80 mL of water. The solution was added into 1.166 mL of concentrated HCl and then centrifuged at 11000 rpm for 5 min for removal of insoluble precipitates. The purified solution was diluted to 200 mL and heated to 98 °C for 24 h. The solid product was collected by centrifugation and washed with water twice. The FeOOH nanorods were dispersed in 40 mL of DI water. The nanorods were modified with PAA before silica coating. A 40 mL dispersion of FeOOH nanorods was added to 160 mL of 0.1 M PAA solution. Ammonia was added to adjust the pH of the solution to 8-9. After overnight stirring, the nanorods were recovered by centrifugation and were redispersed in 200 mL H_2O . Silica coating on FeOOH nanorods was done by adding 150 μL TEOS to 10 mL FeOOH nanorods, 100 mL of ethanol, and 5 mL of ammonia. After stirring for 40 min, the products were centrifuged and washed with ethanol twice. FeOOH@SiO₂ nanorods were then heated at 330 °C for 2 h in a flow of forming gas to convert the nanorods to the magnetic phase.

3.1.2.3 Synthesis of Fe₃O₄@SiO₂/Au@SiO₂ Nanocomposites

The Fe₃O₄@SiO₂ nanorods were dispersed in 30 mL of ethanol and 1 mL of APTES to modify the surface of nanorods with amino groups. The suspension was heated at 80 °C for 3 h, isolated by centrifugation at 8000 rpm for 3 min, washed with ethanol three times and with water once, and redispersed in 40 mL H_2O .

The Au nanoparticles were synthesized with a previously reported method.¹¹ A seed solution was first prepared by a quick injection of 0.6 mL of freshly made NaBH₄ solution (0.1 M) into a mixture containing 1 mL of HAuCl₄ (5 mM), 1 mL of TSC (5 mM), and 18 mL of H_2O under vigorous stirring. The seed solution was stirred for 30 s then left

undisturbed for 4 h to allow the unreacted NaBH_4 to completely decompose. A growth solution was prepared by combining 5 mL of PVP (5 wt%), 2.5 mL of AA (0.1 M), 2 mL of KI (0.2 M), 600 μL of HAuCl_4 (0.25 M), and 10 mL of H_2O . Into the growth solution, 1 mL of seed solution was injected with vigorous stirring. The solution was stirred for 10 min to complete the particle growth and was used without purification.

The Au suspension was mixed with 10 mL of the APTES modified $\text{Fe}_3\text{O}_4@\text{SiO}_2$ nanorods to attach the Au nanoparticles onto the $\text{Fe}_3\text{O}_4@\text{SiO}_2$ nanorods. The mixture was sonicated for 30 min and shaken on a vortex overnight. The as-prepared $\text{Fe}_3\text{O}_4@\text{SiO}_2/\text{Au}$ composites were separated by centrifugation at 8000 rpm for 3 min, washed with water twice, and redispersed in 10 mL of water.

For silica coating, 2 mL of $\text{Fe}_3\text{O}_4@\text{SiO}_2/\text{Au}$ was added to 18 mL of ethanol, 2 mL of water, and 1 mL of $\text{NH}_3\cdot\text{H}_2\text{O}$ with sonication. 40 μL of TEOS was added to the above solution under sonication for 5 minutes and left on vortex for 40 minutes to achieve $\text{Fe}_3\text{O}_4@\text{SiO}_2/\text{Au}@\text{SiO}_2$. The nanocomposites were washed with ethanol twice and redispersed in 4 mL of water.

3.1.2.4 Synthesis of $\text{Fe}_3\text{O}_4@\text{SiO}_2/\text{Au}$ -Au Nanocomposites

For the growth of Au-Au dimers, a growth solution was prepared by mixing 1.5 mL of PVP (5 wt%), 375 μL of AA (0.1 M), 300 μL of KI (0.2 M), 90 μL of HAuCl_4 (0.25M), and 3 mL of H_2O . Then, 4 mL of $\text{Fe}_3\text{O}_4@\text{SiO}_2/\text{Au}@\text{SiO}_2$ was added to 4 mL of the Au growth solution and stirred for 10 minutes. The Au dimers-on-magnetic nanorods were collected by centrifugation at 8000 rpm for 3 min and washed with water twice.

3.1.2.5 Synthesis of Fe₃O₄@SiO₂/Au-Au Nanocomposites

For the growth of Ag, into 4 mL of Fe₃O₄@SiO₂/Au@SiO₂, 6 mL of H₂O, 10 mL of PVP (5 wt%), 50 μL of AgNO₃ (0.1 M), and 100 μL of AA (0.1 M) were added in sequence and stirred for 10 minutes. The same procedure was repeated 6 times. The nanocomposites were washed with water and ethanol to remove the excess reagents.

3.1.2.6 Fabrication of Anticounterfeiting Films

Polyacrylamide precursor was prepared by mixing 0.5 g of acrylamide, 7 mg of N,N'-methylenebis(acrylamide), and 2 mL of ethylene glycol. Then, one batch of nanorods/Au dimers composites was centrifuged and dispersed in 1 mL of the hydrogel precursor mixture, followed by sonication for 5 min. The dispersion was sandwiched between two clean glass slides to form a liquid film. The mixture was then solidified under UV irradiation (365 nm) with a magnetic field applied for 30 s. Patterns were created by blocking the UV light with pre-printed patterns.

3.1.2.7 Characterizations

Transmission electron microscopy (TEM) images were taken with a Philips Tecnai 12 transmission electron microscope operating at 120 kV. The samples for TEM observation were prepared by drop-casting a solution on a carbon film supported on a copper grid. UV-vis spectra were measured by using an Ocean Optics HR 2000CG-UV-NIR spectrometer. Optical microscopy was performed using a Zeiss Axio Imager A1m. Digital images were taken by using Canon EOS Rebel T2i 18.0 MP Digital SLR Camera.

3.1.3 Results and Conclusion

As shown in Figure 3.1b, the key to control the dimer structure was the thickness of the SiO₂ layer coated on the surface. An increase in the SiO₂ thickness would lead to a decrease in the overlapping degree of the dimers. When the SiO₂ thickness exceeded the diameter of AuNPs, the entire particle would be covered by SiO₂; therefore, no exposed site was available for further dimer growth. With decreased SiO₂ thickness, the overlapping degree of the dimers would gradually increase, leading to a decrease in the aspect ratio of the dimers. A lower aspect ratio resulted in the blue shift of the longitudinal peak of the dimers until the passivated area was too small, and the overgrown particle lost the dimer shape and took an oval morphology. As a result, the two modes were no longer distinguishable.

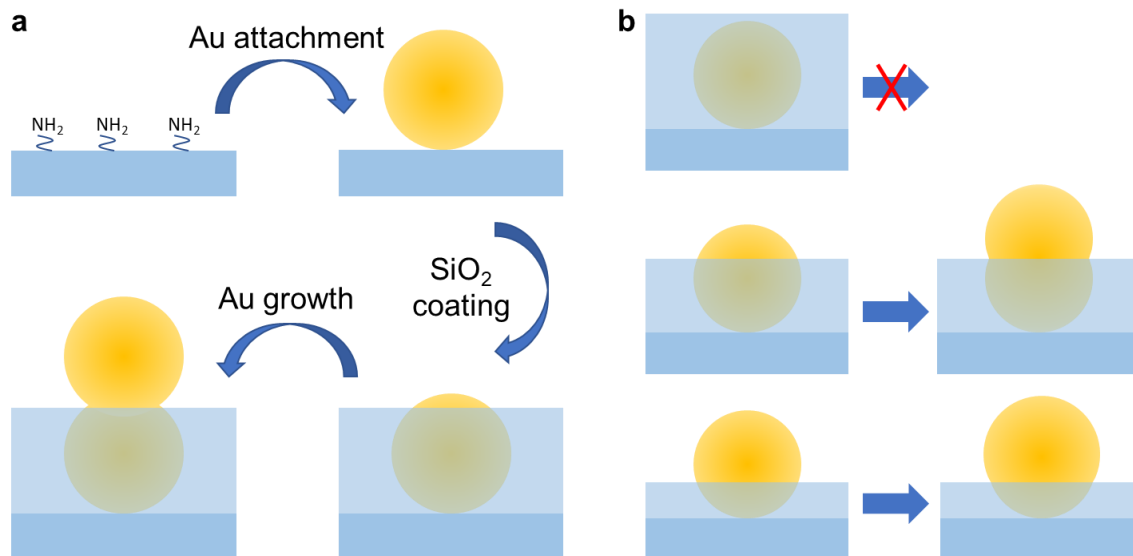


Figure 3.1 Schematics showing (a) the growth of self-aligned Au-Au dimers through partial surface passivation and (b) the control of overlapping degree with SiO₂ coating thickness.

An advantage of the proposed synthesis route is that the dimers were automatically aligned perpendicular to the substrates. Utilizing this phenomenon, when we used $\text{Fe}_3\text{O}_4@\text{SiO}_2$ nanorods as substrates, the orientation of the dimers can be controlled with external magnetic fields. The synthesis of the $\text{Fe}_3\text{O}_4@\text{SiO}_2/\text{Au-Au}$ nanocomposites was shown in Figure 3.2a. Since the growth direction of the dimers were fixed by the SiO_2 coating, it allowed the attachment of Au dimers at a high concentration without server aggregations. Thanks to the negatively charged SiO_2 , the aggregation between nanocomposites can be prevented. As shown in Figure 3.2b, the length of the nanorods we chose was around 3 μm , and the surface of the nanorods was abundant with AuNPs after attachment (Figure 3.2c). With well-controlled SiO_2 coating, only a small area was exposed for further growth, and the exposed Au served as seeds for the growth of the second Au domain. As shown in Figure 3.2d, the Au-dimers produced with this method had uniform morphology with similar overlapping degrees. The UV-vis spectra (Figure 3.2e) showed the evolution from $\text{Fe}_3\text{O}_4@\text{SiO}_2/\text{Au}$ to $\text{Fe}_3\text{O}_4@\text{SiO}_2/\text{Au-Au}$ with the appearance of a second peak at around 660 nm, corresponding to the longitudinal mode of the Au-Au dimers. The distinctive longitudinal peak also indicated the uniform overlapping degrees of the Au-Au dimers, as polydisperse overlapping degrees would result in a severely broadening of the plasmonic peak.

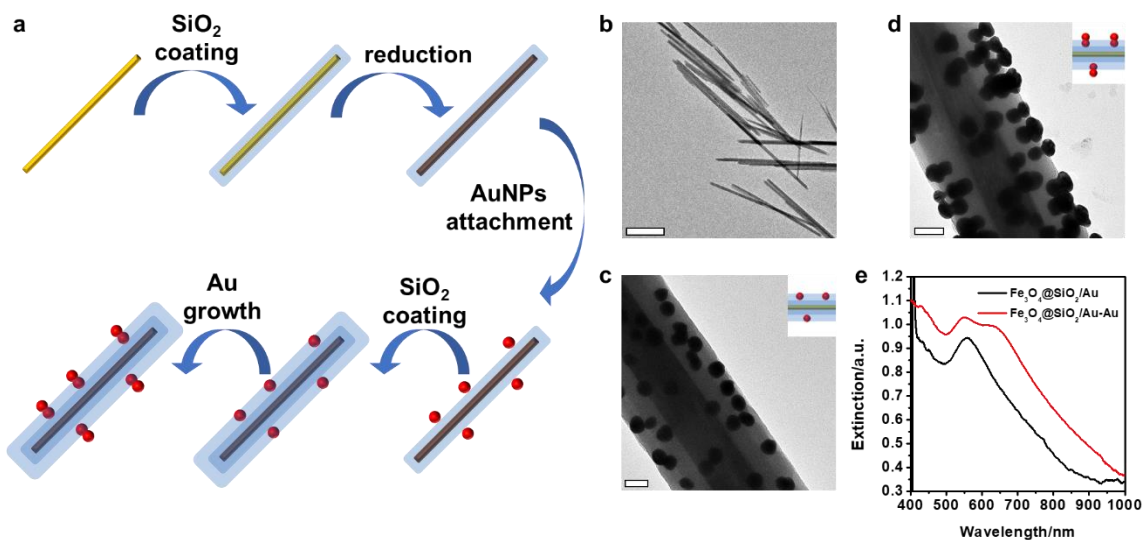


Figure 3.2 (a) Schematics showing the synthesis of Fe₃O₄@SiO₂/Au-Au nanocomposites with Au-Au dimers aligned perpendicular to the Fe₃O₄@SiO₂ nanorods. (b-d) TEM images of (b) FeOOH nanorods, (c) Fe₃O₄@SiO₂/Au@SiO₂, and (d) Fe₃O₄@SiO₂/Au-Au nanocomposites. Scale bar in (b) is 1 μ m. Scale bars in (c) and (d) are 50 nm. (e) UV-vis spectra of Fe₃O₄@SiO₂/Au@SiO₂ and Fe₃O₄@SiO₂/Au-Au nanocomposites.

The formation of the self-aligned dimers on the magnetic nanorods allowed the oriental control of Au-Au and Au-Ag dimers with an external magnetic field. As shown in Figure 3.3a, by changing the relationship between the orientation of nanocomposites to the polarization direction of the incident light, the longitudinal mode was selectively suppressed. To demonstrate the magnetic tuning more clearly, a Cartesian coordinate system was built using the propagation direction of the incident light as the y-axis, the vertical direction as the z-axis. Under unpolarized light, both longitudinal and transverse modes of the dimers were excited. Therefore, the plasmonic peak of all alignment directions was essentially the same, and the spectra of nanocomposites aligned in the x and z direction were the same. However, when the magnetic field was applied in the y direction (P_0B_y), a redshift and enhanced intensity in the longitudinal peak was observed in the UV-vis spectra (Figure 3.3b). This was not due to the selective plasmonic excitation of the Au-Au dimers and will be discussed later. When the orientation of the nanocomposites was perpendicular to the propagation direction of the incident light pointing out of the plane, the plasmonic peaks of the dimers showed angular dependence under polarized light. When the polarization of the incident light was fixed at z direction (P_z), and the magnetic direction gradually changed from x direction (B_x) to z direction (B_z), the peak corresponding to the longitudinal peak gradually decreased and was finally eliminated when the nanocomposites aligned parallel to the polarization direction of the incident light (Figure 3.3c). An obvious color change from purple to red could be seen under the polarizer. When the magnetic field direction changed in the xy plane, theoretically as demonstrated in Figure 3.3a, both the transverse and longitudinal modes of the dimers would be excited, and the spectra of the

nanocomposites should remain the same regardless of the magnetic field direction. However, as seen in the spectra, the extinction peak corresponding to the longitudinal mode redshifted as the magnetic field changed from x (B_x) to y direction (B_y). Although the spectra of the nanocomposites showed a redshift, human eyes are not sensitive to the color change between reddish-purple to blueish purple; therefore, it was not obvious in the digital images. Since the plasmonic excitation should not have a difference in these two alignments, we tuned to the other component of the composite, $Fe_3O_4@SiO_2$ nanorods. As shown in Figure 3.3e, the $Fe_3O_4@SiO_2$ indeed show different extinction profiles in different directions. When the magnetic field was changed from the x to y direction, the extinction at lower wavelengths dramatically decreased while the extinction at longer wavelengths, especially at around 700 nm, was greatly increased. Although the reason for the extinction profile change of the nanorods was not clear, it should be related to the anisotropic scattering behavior of nanorods. This hypothesis was also supported by the angular dependent spectra evolution of the nanocomposites using smaller nanorods as substrates. As shown in Figure 3.3f, when $Fe_3O_4@SiO_2$ with a length of 400 nm instead of 3 μm was used, the UV-vis spectra did not exhibit such a dramatic change as the 3 μm nanorods did. Therefore, the spectra profile change when the magnetic field was changing in the xy plane was not obvious. Under the z-polarized light, when the magnetic field applied changed from x direction ($P_z B_x$) to z direction ($P_z B_z$), the extinction of the nanorods gradually increased throughout the visible range (Figure 3.3d), which also explained the increase of baseline extinction of the nanocomposites observed in Figure 3.3b. This could be attributed to the cross-section changed due to the relative orientation of the nanorods.

When the nanorods were aligned perpendicular to the polarization direction, the cross-section of the nanorods in the polarization direction was minimized, while when the nanorods were oriented parallel to the polarization direction, the absorption cross-section was at the maximum. This phenomenon was also observed in the nanocomposites using smaller nanorods, except for a decrease in the intensity difference since the aspect ratio of the 400-nm nanorods were smaller than the 3- μm ones.

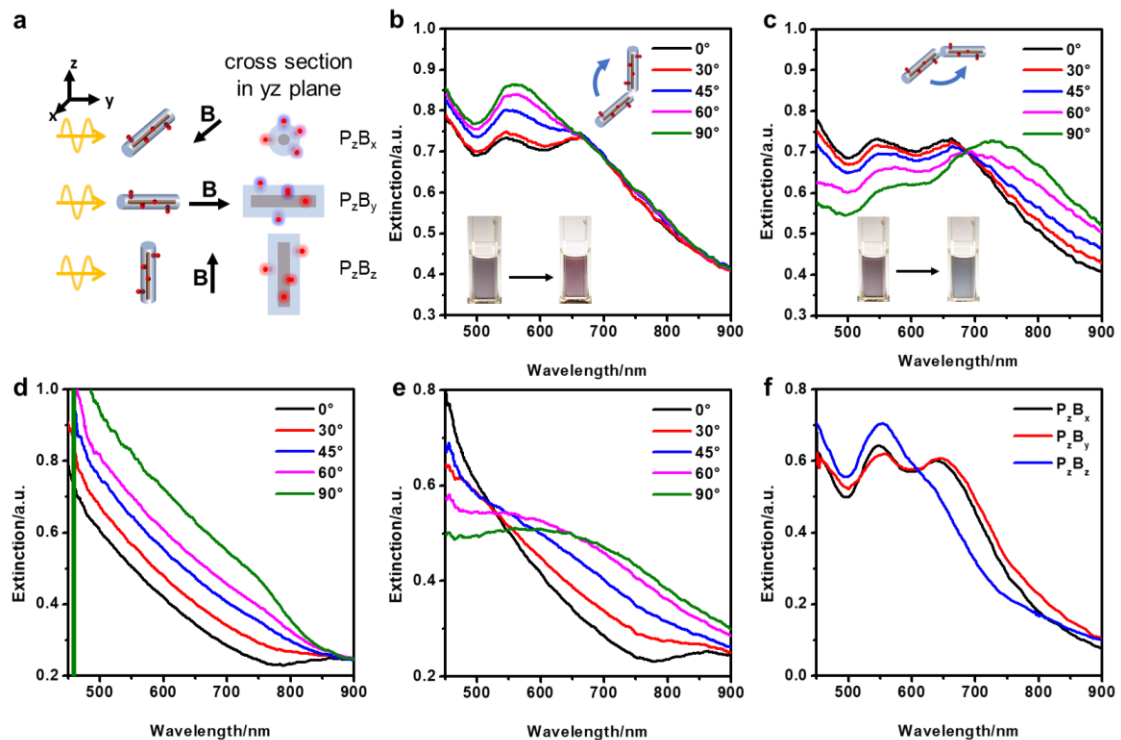


Figure 3.3 (a) Schematics showing the magnetic tuning of nanocomposites. (b-e) UV-vis spectra of (b-c) nanocomposites and (d-e) $Fe_3O_4@SiO_2$ nanorods under z-polarized light with magnetic field changing in (b, d) xz plane and (c, e) xy plane. Insets in (b) and (c) are the digital images of the solutions. (f) UV-vis spectra of nanocomposites synthesized with 400-nm Fe_3O_4 nanorods under different magnetic field directions.

As shown in Figure 3.4a, Ag can also grow on the exposed Au and formed Au-Ag dimers. When Ag instead of Au was deposited, the Au-Ag dimers showed three plasmonic peaks in the UV-vis spectra (Figure 3.4c). The peak located at around 630 nm corresponded to the longitudinal mode of the Au-Ag dimers, while the plasmonic peaks at around 400 nm and 520 nm represented the transverse plasmonic resonance of Ag and Au domains, respectively. The color of the solution appeared to be yellowish-green without any magnetic field applied. It was interesting to notice that when the magnetic field was tuned within the xy plane, the peak corresponding to the longitudinal mode dramatically redshifted, and an obvious color change from green to blue can be observed. Under z-polarized light, when the magnetic field changed from x (P_zB_x) to z direction (P_zB_z), the longitudinal peak was suppressed and the plasmonic peak corresponding to the transverse resonance mode of Au and Ag domains became more pronounced. As shown in the digital image, the color of the solution changed from green to red-orange (Figure 3.4d). The composites could be coated with another layer of SiO₂ to enhance the stability of the Au-Ag dimers, especially the Ag domain, and as shown in Figure 3.4b, the dimer structures were well preserved.

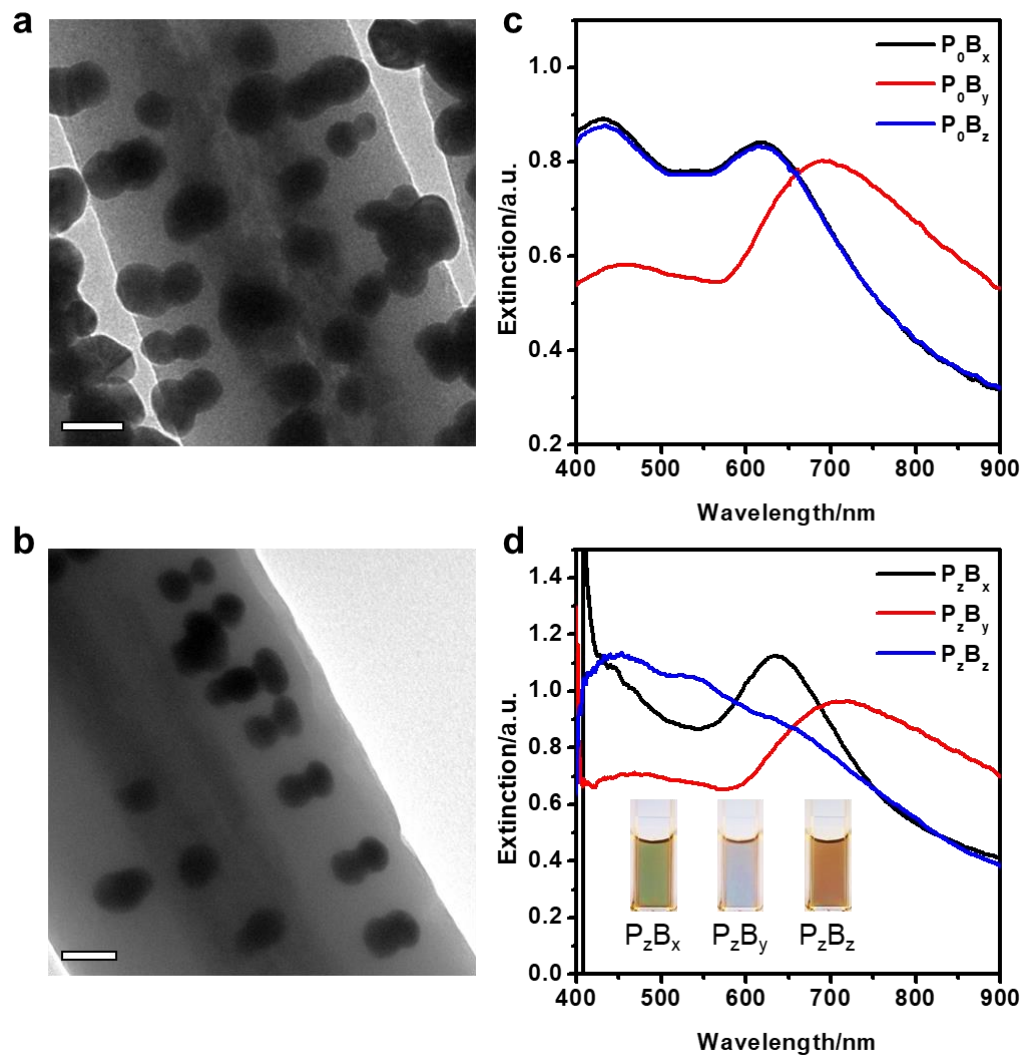


Figure 3.4 TEM image of (a) $\text{Fe}_3\text{O}_4@\text{SiO}_2/\text{Au-Ag}$ and (b) nanocomposites coated with another layer of SiO_2 . UV-vis spectra of $\text{Fe}_3\text{O}_4@\text{SiO}_2/\text{Au-Ag}$ under (c) unpolarized light and (d) z-polarized light.

Due to the magnetically tunable plasmonic excitation of the plasmonic/magnetic nanocomposites, we fabricated a polarization-dependent color-switching display by fixing the nanocomposites in a thin solvocal film. Here, we use the $\text{Fe}_3\text{O}_4@\text{SiO}_2/\text{Au-Au}$ nanocomposites as an example to demonstrate the fabrication of the thin film. The polyacrylamide hydrogel was chosen as the medium of the film because the nanocomposites can be dispersed very well in the hydrogel precursor. In addition, the polymerization of acrylamide can be initiated by UV light, which provided a convenient approach to create patterns on the films. As shown in Figure 3.5a, the polyacrylamide hydrogel precursor containing the nanocomposites was sandwiched between two glass slides. To control the thickness of the film, a cover glass was used as a spacer. An ink-jet printed pattern was applied atop the glass slide as a mask to block the UV light. The sample was subjected to the UV radiation for 30 s with the magnetic field applied in the desired direction to cure the exposed area, and the orientation of the nanocomposites was fixed in the applied magnetic field direction. Then the mask was removed, and the whole film was subjected to another UV radiation for 30 s with the magnetic field applied in other directions to fix the nanocomposites' orientation in the rest of the film. As shown in Figure 3.5b and c, the orientation of the nanocomposites in the left part of the film was horizontal while the nanocomposites were aligned vertically in the right part of the film. Under natural light, the film showed a uniform reddish-purple color, while under horizontally polarized light, the film showed red and purple colors on the left and right, respectively. When the polarization of the incident light changed from horizontal to vertical, the left side turns from red to purple when the right part did the opposite. In another case, where the

nanocomposites aligned horizontally on the left but perpendicular to the plane on the right (Figure 3.5d and e), under polarized light, the left side was insensitive to the polarization change while the right part switched between red and purple when the polarization direction changed from horizontal to vertical. It is worth noticing that although the color difference between the two regions, in this case, was distinctive under the microscope, which used a strong tungsten light source, under normal lighting conditions, the color difference in the film is hard to notice.

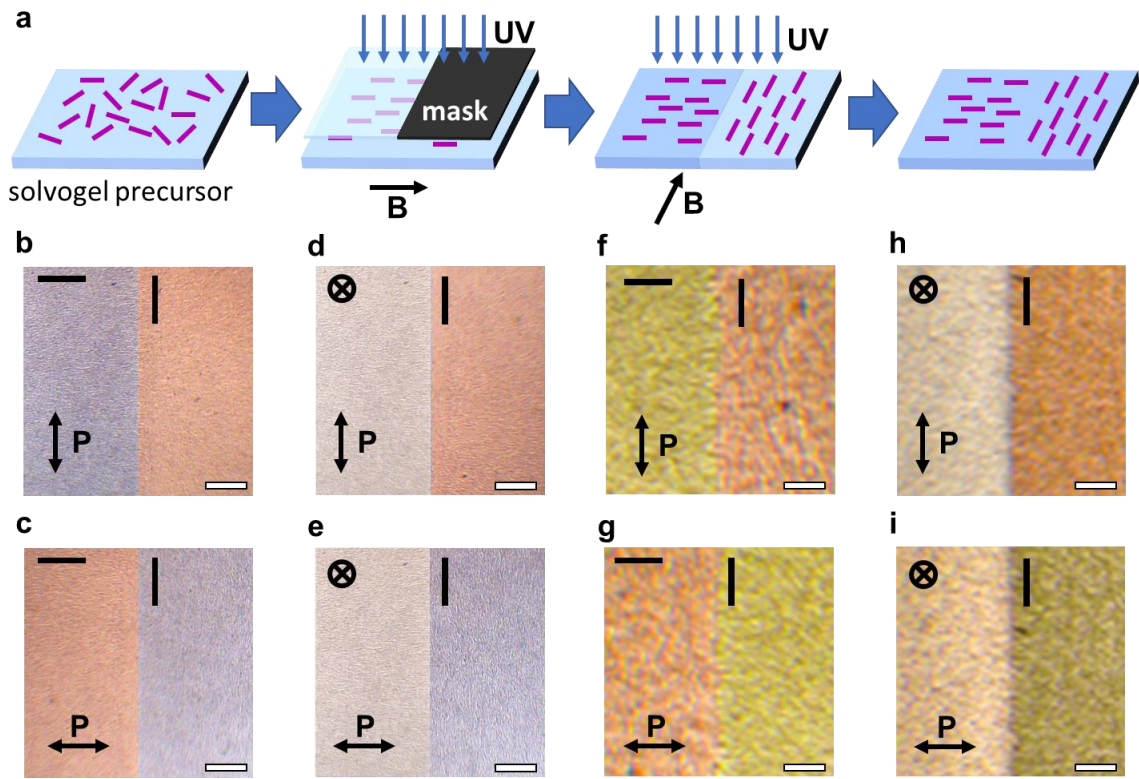


Figure 3.5 (a) Schematics showing the fabrication of the nanocomposite/solvogel film with different alignment in the two regions. (b-i) Polarized optical microscope image of solvogel films with (b-e) $\text{Fe}_3\text{O}_4@SiO_2/Au-Au$ and (f-i) $\text{Fe}_3\text{O}_4@SiO_2/Au-Ag$ nanocomposites with nanocomposite alignment indicated at the top of the images and polarization of incident light indicated at the bottom of the images. Scale bars are 200 μm .

Utilizing the color switching behaviors of the three orientations of the nanocomposites, we designed a more complicated pattern for anti-counterfeiting devices. As shown in Figure 3.6a, the pattern was divided into three regions, Region I with nanocomposites aligned perpendicular to the film, Region II, with nanocomposites aligned horizontally, and Region III with nanocomposites vertically aligned. Under unpolarized light, the pattern was barely visible (Figure 3.6b). When the polarized light was used (Figure 3.6c and d), the color of the paddles would switch with polarization change while Region I remained the same color, and the regions visible would change according to the polarization.

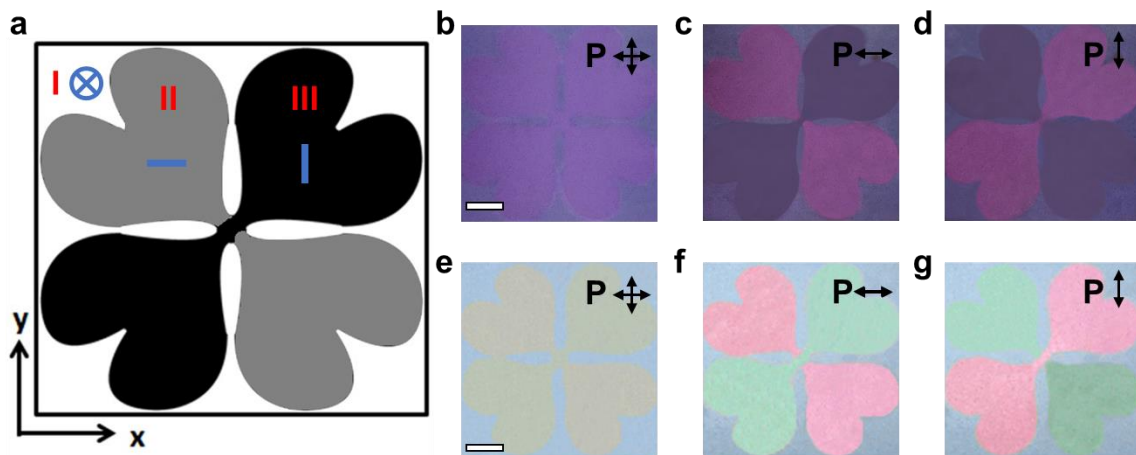


Figure 3.6 (a) Schematics showing the alignment of nanocomposites in different regions. (b-g) Optical images of solvocal films with (b-d) Fe₃O₄@SiO₂/Au-Au and (e-g) Fe₃O₄@SiO₂/Au-Ag nanocomposites under (b, e) unpolarized light, (c, f) x-polarized and (d, g) y-polarized light. Scale bars are 1.5 mm.

When the $\text{Fe}_3\text{O}_4@\text{SiO}_2/\text{Au-Ag}$ nanocomposites were used instead, the color switch became more distinctive since the human eyes are more sensitive to the color contrast between green, red, and blue. Similar to the composites with Au-Au dimers, the film showed a homogeneous yellowish-green color under unpolarized light. When the horizontally polarized light was used (Figure 3.5f and g), the film was split into a green region (left) and a red region (right), representing the alignment of nanocomposite in the vertical and horizontal directions, respectively. When the alignment of the nanocomposite on the left side was changed to perpendicular to the plane (Figure 3.5h and i), the right part of the film showed a blue color and was insensitive to the polarization change, while the left side switched between red and green with polarization changed. When the $\text{Fe}_3\text{O}_4@\text{SiO}_2/\text{Au-Ag}$ nanocomposites were used to create the three-region patterns (Figure 3.6 e-g), the flower pattern is always visible regardless of the polarization, which was different from the patterns created with the $\text{Fe}_3\text{O}_4@\text{SiO}_2/\text{Au-Au}$ nanocomposites. When the polarization switched between horizontal and vertical directions, the color of the paddles switched between green and red correspondingly. Since the blue color originated from the anisotropic scattering of the large-sized $\text{Fe}_3\text{O}_4@\text{SiO}_2$ nanorods, the magnetic nanorods could be substituted with 400-nm nanorods if we wanted to achieve the switchable visibility of the patterns similar to $\text{Fe}_3\text{O}_4@\text{SiO}_2/\text{Au-Au}$ nanocomposites.

3.1.4 Conclusion

In summary, the unique partial surface passivation strategy allowed the synthesis of Au-Au and Au-Ag dimers that were readily aligned perpendicularly to the substrate. A nanocomposite containing self-aligned Au dimers and the magnetically responsive nanorods were conveniently synthesized. The magnetic tuning of the plasmonic excitation of the longitudinal resonance mode was achieved. In addition, due to the stability of the nanocomposites, it can be easily incorporated into hydrogel films to create patterned films with different nanocomposite orientations in each region utilizing lithography methods. The prepared film showed both polarization-insensitive color and polarization-sensitive color-switching by changing the relative orientation of the nanocomposite orientation and the propagation and polarization directions of the incident light, broadening possibilities for the fabrication of visible anticounterfeiting devices.

3.2 Synthesis and Magnetic Manipulation of Au@Fe₃O₄ and Ag@Fe₃O₄ Nanostructures

3.2.1 Introduction

In the previous section, a method to achieve the dynamic magnetic tuning of the optical properties of anisotropic plasmonic nanostructures was demonstrated. However, this method still failed to solve the problem of the limited choice of morphologies for plasmonic nanoparticles. A more straightforward way to achieve this goal was to directly coat the magnetic materials on the plasmonic nanoparticles. In this way, the plasmonic nanostructures with desired optical properties could be pre-synthesized then subjected to magnetic coating, making the optical properties of the nanocomposites more predictable.

However, the direct coating of the Fe_3O_4 on plasmonic nanoparticles, for example, AuNPs was hard to achieve due to the large lattice mismatch between the Au and Fe_3O_4 .¹²⁻¹⁴ However, the solvothermal synthesis of $\text{Ag}@\text{Fe}_3\text{O}_4$ core-shell nanoparticles indicated that the heterogenous nucleation of Fe_3O_4 was still preferred with the presence of Au or Ag NPs as seeds.¹⁵⁻¹⁶ The key to the successful coating of Fe_3O_4 on plasmonic nanoparticle surface is (1) to lower the self-nucleation rate of the Fe_3O_4 in the synthesis and (2) to decrease the Fe_3O_4 crystal grain size to reduce the crystal strain induced by lattice mismatch. Previously, our group reported the synthesis of Fe_3O_4 colloidal nanocrystals (CNCs), and a main feature of the CNCs was that the cluster consists of ultrafine Fe_3O_4 nanocrystals with grain size ~ 6 nm, which was suitable for the purpose of the formation of the magnetic coating on plasmonic nanoparticles.¹⁷

In this work, we demonstrated the coating of Fe_3O_4 on Au and Ag nanostructures and the magnetic tuning of these nanostructures. In this section, we also demonstrated the fabrication of a smart display device using $\text{Ag}@\text{Fe}_3\text{O}_4$ nanoplates.

3.2.2 Experimental

3.2.2.1 Chemicals

Poly(vinylpyrrolidone) (PVP, $M_w=10,000$), diethylene glycol (DEG), ethylene glycol (EG), potassium iodide (KI), L-ascorbic acid (AA), sodium borohydride (NaBH_4 , 99%), sodium hydroxide (NaOH), chloroauric acid (HAuCl_4), polyacrylic acid (PAA, average $M.W.=1800$), polyacrylic acid sodium salt (PAASS), and trisodium citrate (TSC) were purchased from Sigma-Aldrich. Ammonium hydroxide ($\text{NH}_3 \cdot \text{H}_2\text{O}$, 28% by weight in water) and hydrochloric acid (HCl, 37%) were purchased from Fisher Scientific. Silver

nitrate (AgNO_3 , 99.9+%), copper (II) chloride (CuCl_2), and iron (III) chloride anhydrous (FeCl_3 , 98%) were purchased from Alfa Aesar. Ethanol (200 proof) was purchased from Decon Laboratories Inc. All chemicals were directly used without further purification.

3.2.2.2 Synthesis of Au Nanoparticles (AuNPs)

The Au nanoparticles were synthesized using the same method as in Section 3.1.2.3.

3.2.2.3 Synthesis of Ag Nanowires (AgNWs)

The synthesis of Ag nanowires was carried out following the method published by Younan Xia.¹⁸ For a typical synthesis, 50 mL of EG was added to a three-neck flask and was heated at 150 °C under N_2 protection for 1 h to eliminate oxygen dissolved in the solvent. After heating for 1 h, 0.4 mL of CuCl_2 (4 mM) solution in EG was added and heated for another 15 min. Into the mixture, 15 mL of PVP (0.147 M, calculated in terms of repeating unit) solution in EG was injected, followed by the addition of 15 mL of AgNO_3 (0.094 M) solution in EG. The reaction was carried out at 150 °C for an additional 1.5 h, and the color of the solution turned from clear to yellow, then green, and finally opaque gray, indicating a successful synthesis of AgNWs. The products were separated by centrifugation at 3000 rpm for 3 min.

3.2.2.4 Synthesis of Ag Nanoplates (AgPLTs)

The Ag nanoplates were synthesized with a previously reported method.¹⁹ In a typical synthesis, a seed solution was first prepared. Into a 125-mL flask, 25 mL of AgNO_3 (0.1 mM), 0.3 mL of TSC (30 mM), 1.5 mL of PVP (3.5 mM, calculated in terms of repeating unit), and 60 μL of H_2O_2 were added under vigorous stirring. The reaction was

initiated by injecting 250 μL of freshly prepared NaBH_4 (0.1 M) into the mixture. The mixture was stirred for 30 min for the production of seeds.

The free PVP molecules were removed by centrifuging 25 mL of the solution at 11000 rpm for 8 min and redispersing into 20 mL of deionized water. The Ag nanoplates were washed three times and redispersed in 40 mL of H_2O . For the seed-mediated growth of Ag nanoplates, 0.375 mL of AA (0.1 M) and 0.125 mL of TSC (0.075 M) were added into 10 mL of the seed solution under magnetic stirring. A growth solution was prepared separately by combining 20 mL of AgNO_3 (1 mM), 0.125 mL of CA (0.1 M), and 0.1 mL of TSC (1.5 mM). The growth solution was added into the seed solution through a syringe pump with an injection rate of 0.2 mL/min until the volume added reached 5 mL. The Ag nanoplates were separated by centrifugation at 3000 rpm for 3 min.

3.2.2.5 Synthesis of Plasmonic@ Fe_3O_4 Core-Shell Nanoparticles

The AuNPs were centrifuged and redispersed in 1 mL of DEG to be used as seeds. For Fe_3O_4 coating, two stock solutions were first prepared. A FeCl_3/DEG stock solution was prepared by dissolving 16 mmol anhydrous FeCl_3 in 40 mL DEG to make the FeCl_3 concentration 0.4 M. The solution was heated for 80 $^\circ\text{C}$ for 1 h under N_2 protection. The solution was then stored at temperature. Another NaOH/DEG solution was prepared by dissolving 0.1 mol NaOH in 40 mL DEG to make the NaOH concentration 2.5 M. The solution was heated at 120 $^\circ\text{C}$ under N_2 protection for 1 h and turned brown after heating. The solution was cooled down and stored at 70 $^\circ\text{C}$ before using. In a three-neck flask, 4 mmol PAA (calculated in terms of repeating unit) was dissolved in 15 mL of DEG. Into the flask, 1 mL of FeCl_3/DEG stock solution was added. The mixture was heated at 220 $^\circ\text{C}$

under N₂ protection for 30 min until the color of the solution turned light yellow. At this point, 1 mL of AuNPs/DEG solution and 1.75 mL of NaOH/DEG stock solution were rapidly injected into the flask simultaneously under vigorous stirring. The mixture was heated for another 1 h under N₂ protection and cooled down to room temperature. The products were diluted with 30 mL of ethanol and centrifuged at 9000 rpm for 5 min. The products were then washed with water three times and redispersed in water.

The Fe₃O₄ coating on Ag microstructures (AgNWs and AgPLTs) was carried out in the same process.

3.2.2.8 Characterization

Transmission electron microscopy (TEM) images were taken with a Philips Tecnai 12 transmission electron microscope operating at 120 kV. The samples for TEM observation were prepared by drop-casting a solution on a carbon film supported on a copper grid. UV-vis spectra were measured by using an Ocean Optics HR 2000CG-UV-NIR spectrometer. Optical microscopy was performed using a Zeiss Axio Imager A1m. Digital images were taken by using Canon EOS Rebel T2i 18.0 MP Digital SLR Camera.

3.2.3 Results and Conclusion

The typical synthesis of Fe₃O₄ colloidal nanocrystal clusters (CNCs) was carried out by first reducing FeCl₃ with DEG to obtain a mixture of FeCl₃ and FeCl₂, to which NaOH was injected to induce the hydrolysis of Fe³⁺ and Fe²⁺. The produced hydroxides were then dehydrated to form Fe₃O₄ nanocrystals. The AuNPs were introduced along with the injection of NaOH during the typical CNC synthesis to serve as cores for the deposition of Fe₃O₄. As shown in Figure 3.7a, when PVP-capped AuNPs were directly used as seeds,

the Fe_3O_4 tended to self-nucleate instead of coating on the AuNPs surface. This can be attributed to the fact that the AuNPs surface was well-capped by PVP; as a result, the surface energy of the AuNPs was relatively low, and heterogenous nucleation of Fe_3O_4 , in this case, was not favored. To confirm our hypothesis, we used AuNPs aged in the growth solution for different times as seeds to perform the Fe_3O_4 coating. As shown in Figure 3.7b-d, the longer AuNPs were aged in the growth solution, the better the PVP can cap the Au surface. As a result, with freshly prepared AuNPs, Fe_3O_4 can be successfully coated, and with increasing aging time, a lower population of AuNPs would be coated with Fe_3O_4 . When the AuNPs were aged for 1 h, Fe_3O_4 would self-nucleate, as shown in Figure 3.7d, and the AuNPs tend to aggregate due to the high ionic strength in the solution. To further prove our theory, PVP-capped AuNPs were bubbled with air for 1 h. PVP would be oxidized during the bubbling process and partially removed from the Au surface. As a result, the AuNPs with air bubbling treatment could also be uniformly coated with Fe_3O_4 , and as shown in Figure 3.7e, the composites could be easily separated with a magnet (Figure 3.7f).

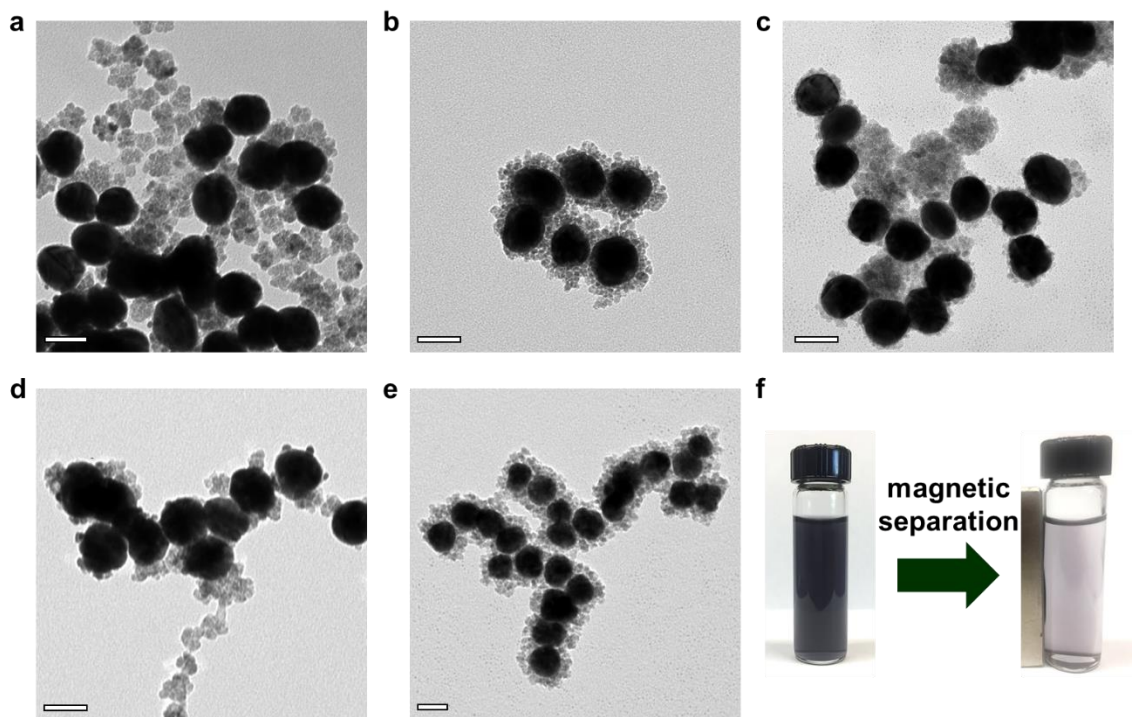


Figure 3.7 TEM images of Au@Fe₃O₄ core-shell composites synthesized with AuNPs aged in growth solution for (a) 2h, (b) 0 min, (c) 30 min, and (d) 1 h after synthesis, and (e) AuNPs bubbled with air for 1h. Scale bars are 50 nm. (f) Digital image showing the magnetic separation of the nanocomposites.

Due to the lattice mismatch between Au and Fe₃O₄, the crystal strain would quickly build up with increasing Fe₃O₄ crystal grain size. When the NaOH concentration during the synthesis was changed, the crystal size of the Fe₃O₄ nanocrystals could be affected since the formation of Fe(OH)₃ and Fe(OH)₂ was the first step of the reaction that produced precursors for Fe₃O₄ nanocrystals. In the standard synthesis procedure, 1.75 mL of NaOH was added, making the NaOH concentration in the final solution about 0.25 M. The typical crystal sizes were around 7 nm (Figure 3.8b). As shown in Figure 3.8a, with less NaOH added, the Fe₃O₄ crystal size would be smaller, with an average crystal size around 4 nm. In this case, a thin and uniform coating of Fe₃O₄ can be found on the Au surface. However, due to the small crystal size and low Fe₃O₄ amount, the magnetic properties of the composites were relatively weak, and under a magnetic field, not all the nanoparticles can be aligned. When the amount of NaOH was increased to 2.7 mL (Figure 3.8c), making the concentration of NaOH in the final solution 0.36 M, the crystal size of Fe₃O₄ increased to 12 nm. Although the magnetic nanoparticles could still be coated on Au surface, the coating became less uniform, and self-nucleation of Fe₃O₄ can be observed.

The surfactant PAA could also be used to control the crystal size of Fe₃O₄ nanocrystals. Typically, 0.288 g PAA (4 mmol) was dissolved in DEG during the synthesis. When the PAA concentration was reduced to half of the standard protocol, the crystal size increased to 14 nm. As demonstrated in Figure 3.8d, the Fe₃O₄ was not able to form a uniform coating on the Au surface, and severe self-nucleation of Fe₃O₄ could be observed. On the other hand, when the PAA concentration was doubled (Figure 3.8e), a dramatic decrease in the Fe₃O₄ crystal size could be observed, and a uniform thin coating of Fe₃O₄

(<2 nm) could be formed on the Au surface. We hypothesize that the tuning ability of PAA should be attributed to the acidity of the carboxyl groups of PAA. Since the concentrations of PAA and NaOH were at a similar scale (0.225 M vs. 0.25 M), the change in the PAA concentration could dramatically change the acidity of the solution, which influenced the formation of $\text{Fe}(\text{OH})_3$ and $\text{Fe}(\text{OH})_2$. To confirm our theory, another Fe_3O_4 coating was carried out with the addition of 4 mmol PAA and 4 mmol poly(acrylic acid sodium salt) (PAASS). In this way, the concentration of the carboxyl groups was increased, while the acidity of the solution remained roughly the same. As a result, the plasmonic/magnetic nanocomposites were similar to the products synthesized without additional PAASS (Figure 3.8f), except the time for the reduction was shortened and the light-yellow color appeared at 15 min instead of 30 min.

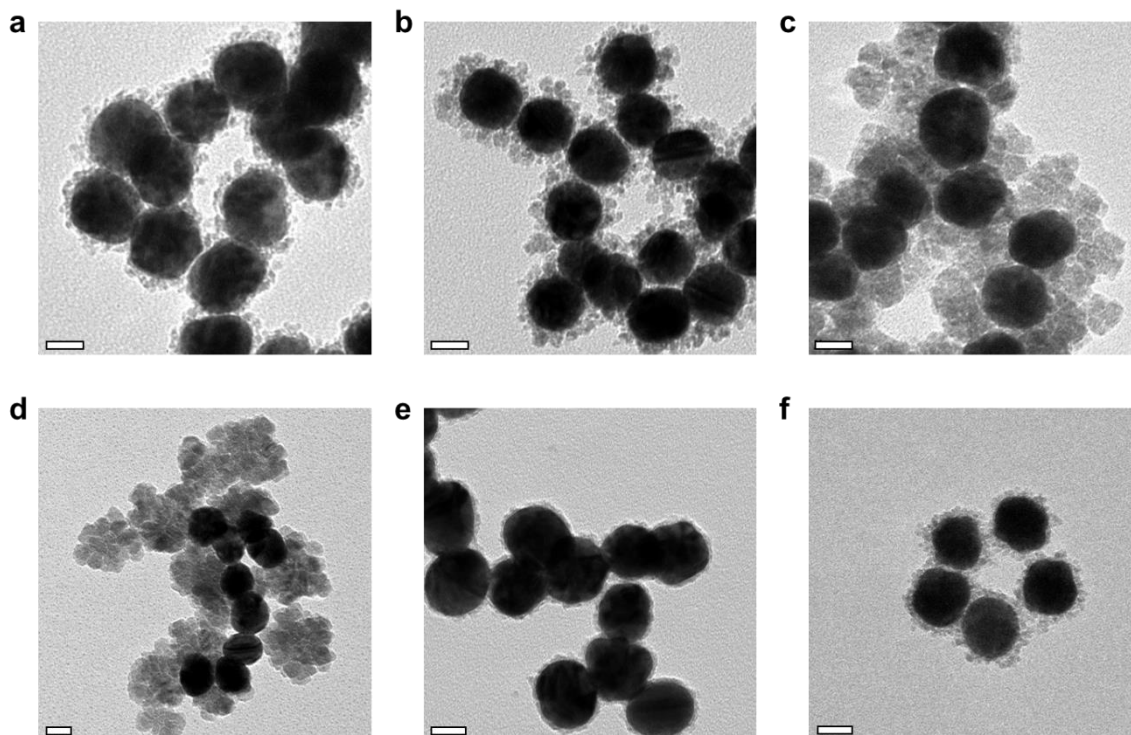


Figure 3.8 TEM images of Au@Fe₃O₄ synthesized at various conditions. The volume of 2.5 M NaOH/DEG solution in (a), (b) and (c) were 1.5 mL, 1.75 mL and 2.7 mL, respectively. The amount of PAA added in the system in (d), (b), and (e) were 2 mmol, 4 mmol, and 8 mmol, respectively. A mixture of 4 mmol PAA and 4 mmol PAASS were added in (f) during synthesis. Scale bars are 20 nm.

As shown in Figure 3.9a-d, by changing the Au/Fe ratio during the synthesis, the thickness of Fe₃O₄ coated on the AuNPs. Since the hydrolysis of the Fe³⁺ and Fe²⁺ were controlled by NaOH and PAA, changing the concentration of FeCl₃ added in the reaction was not approachable. However, the concentration of the Au nanoparticles could be easily changed. With decreasing Au concentration, the Fe₃O₄ thickness gradually increased. It is worth noting that the size of the Fe₃O₄ nanocrystals did not change significantly. The increase in the Fe₃O₄ thickness came from the increased layers of Fe₃O₄ nanocrystals deposited on the Au nanoparticles. The unique “layer-by-layer” deposition growth behavior of the Fe₃O₄ nanocrystals allowed the increase of Fe₃O₄ thickness without inducing large crystal strain that led to self-nucleation. As shown in Figure 3.9e, a linear relationship can be drawn between one over the volume of AuNPs added and the volume of individual core-shell nanoparticles, confirming the “layer-by-layer” depositing mode of the Fe₃O₄ nanocrystals.

As can be seen in the results, the AuNPs were not individually coated with Fe₃O₄. Instead, the AuNPs formed assembly structures during the coating process. As shown in both the TEM images (Figure 3.9g) and the UV-vis spectra (Figure 3.9j), the distance between AuNPs was close throughout the assembly structure, and a distinctive coupling peak of AuNPs was observed at 820 nm. The controlled assembly of the AuNPs should be attributed to the high concentration of Fe³⁺ and Fe²⁺ ions in the system, lowering the solubility of the AuNPs. When different sized AuNPs were added to the system, we saw a clear decreasing trend of the number of particles and increasing interparticle distance in the assembly structures formed during the Fe₃O₄ coating process (Figure 3.9g-i). When 20 nm

AuNPs were used, the AuNPs severely aggregated due to the high specific surface area, and only a broad peak could be seen in the UV-vis spectrum. When the AuNPs size increased to 45 nm, compared to the case where 33-nm AuNPs were used, the coupling peak was much weaker, and the resonance wavelength of the coupling peak blueshifted, indicating an increase in the interparticle distance between AuNPs in the assemblies. When the size of AuNPs was further increased, although small-scale assemblies could still be seen in the TEM image (Figure 3.9i), the UV-vis spectra showed no obvious plasmonic peaks corresponding to the coupling of AuNPs, which suggested that the interparticle distance was larger enough to prevent the interfering of plasmonic resonance from neighboring particles.

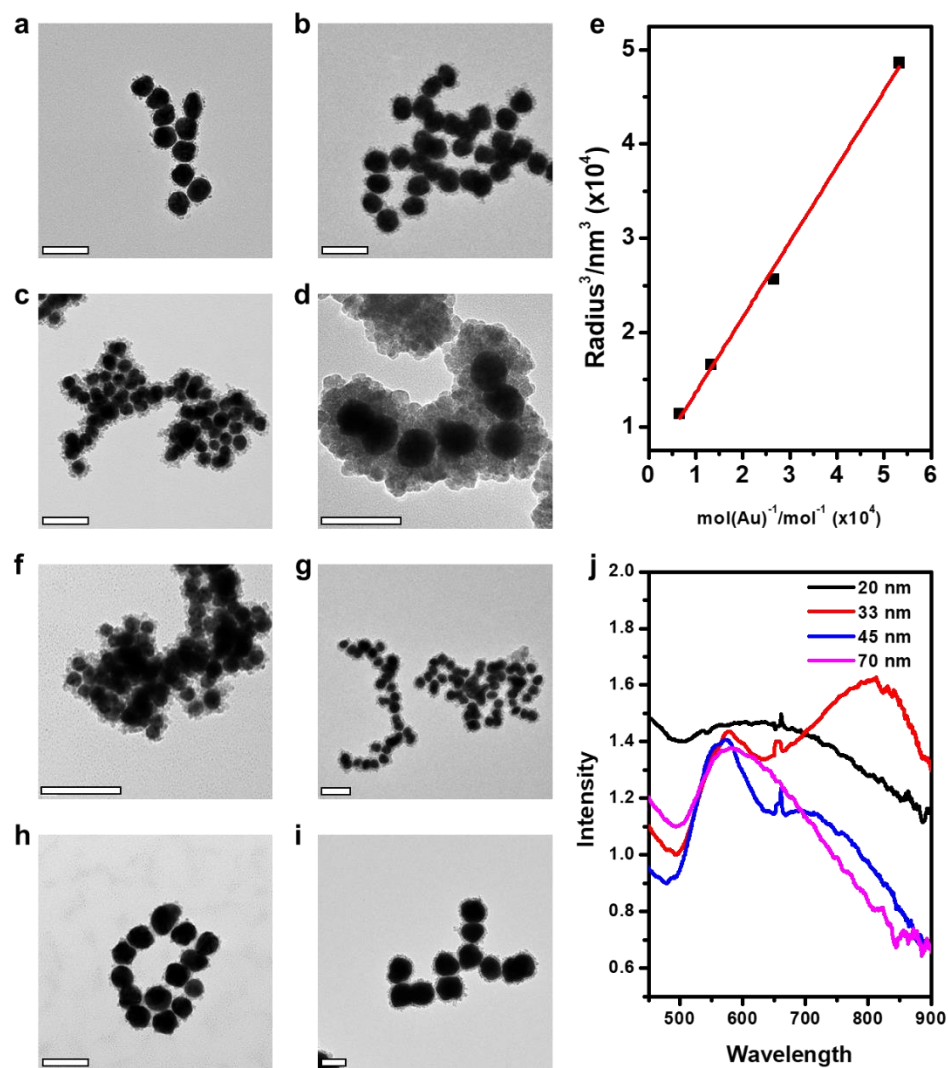


Figure 3.9 TEM images of Au@Fe₃O₄ core-shell particles synthesized with different **(a-d)** AuNPs concentration and **(f-j)** AuNPs sizes. The final concentration of AuNPs in **(a)**, **(b)**, **(c)** and **(d)** were 15 μM, 7.5 μM, 3.75 μM and 1.88 μM, respectively. The AuNPs sizes in **(f)**, **(g)**, **(h)**, and **(i)** were 20 nm, 33 nm, 45 nm and 70 nm, respectively. Scale bars are 100 nm. **(e)** The evolution of radius³ with respect to 1/mol(Au). **(j)** UV-vis spectra with Au@Fe₃O₄ synthesized with different AuNPs sizes.

When micro-sized structures were subjected to the Fe_3O_4 coating process, the aggregation could be prevented. As shown in Figure 3.10 a and b, both Ag nanowires (AgNWs) and Ag nanoplates (AgPLTs) can be coated with Fe_3O_4 with the proposed procedure. The thickness of Fe_3O_4 coated on the nanostructures can also be tuned by adjusting the amount of seeds added. The orientation of $\text{Ag@Fe}_3\text{O}_4$ NWs and $\text{Ag@Fe}_3\text{O}_4$ PLTs can be tuned with the external magnetic field. As shown in the UV-vis spectra (Figure 3.10d), the orientation tuning of the chains formed by $\text{Ag@Fe}_3\text{O}_4$ PLTs showed very different transmittance when the magnetic field was applied along or perpendicular to the propagation direction of the incident light. As illustrated in Figure 3.10c, when the magnetic field was applied along with the light propagation direction, both the absorption and scattering cross-section were minimized, while when the magnetic field was applied perpendicular to the incident light, a portion of the $\text{Ag@Fe}_3\text{O}_4$ PLTs were facing the incident light, and the large physical cross-section greatly increased both the absorption and scattering of light (Figure 3.10c). Based on this phenomenon, we fabricated a smart window and a smart display device to feature the magnetically controlled transmittance change and scattering change, respectively.

As shown in Figure 3.10d, the transmission of the $\text{Ag@Fe}_3\text{O}_4$ PLT gradually decreased with increasing Fe_3O_4 thickness. In addition, when the Ag/Fe ratio was lower than 0.25, the transmittance difference decreased with decreasing Ag/Fe ratio, as the ultrafine Fe_3O_4 nanocrystals increased the overall absorption and had no angular dependence in the absorption cross-section. When the Ag/Fe ratio went beyond 0.25, the magnetic response of the nanocomposites was too weak to efficiently change the

orientation of the AgPLTs. We chose an Ag/Fe ratio of 0.25 and sealed the solution in a homemade glass box with an inner thickness of 3 mm. As shown in Figure 3.10e, when the magnetic field was applied in the horizontal direction, the solution became opaque, and the text underneath could not be seen. When the direction of the magnetic field applied changed to out-of-plane, the transmittance of the solution was greatly increased, and the text underneath could be clearly seen. Figure 3.10f and g showed the smart display device fabricated with the Ag@Fe₃O₄PLTs nanocomposites. Similar to the smart window, the solution was sealed in a homemade glass box with an inner thickness of 3 mm. The letter UCR with three different colors were projected by a projector. When the magnetic field was applied parallel to the incident light, the display device would be close to transparent; only a faint reflection from the glass cover could be seen (Figure 3.10f). When the magnetic field was changed to perpendicular to the incident light, the reflection of the device was greatly enhanced, and the three letters could be clearly seen (Figure 3.10g). Since Ag nanoplate has a consistent scattering throughout the visible region, the colors of the patterns projected onto the device can be well preserved.

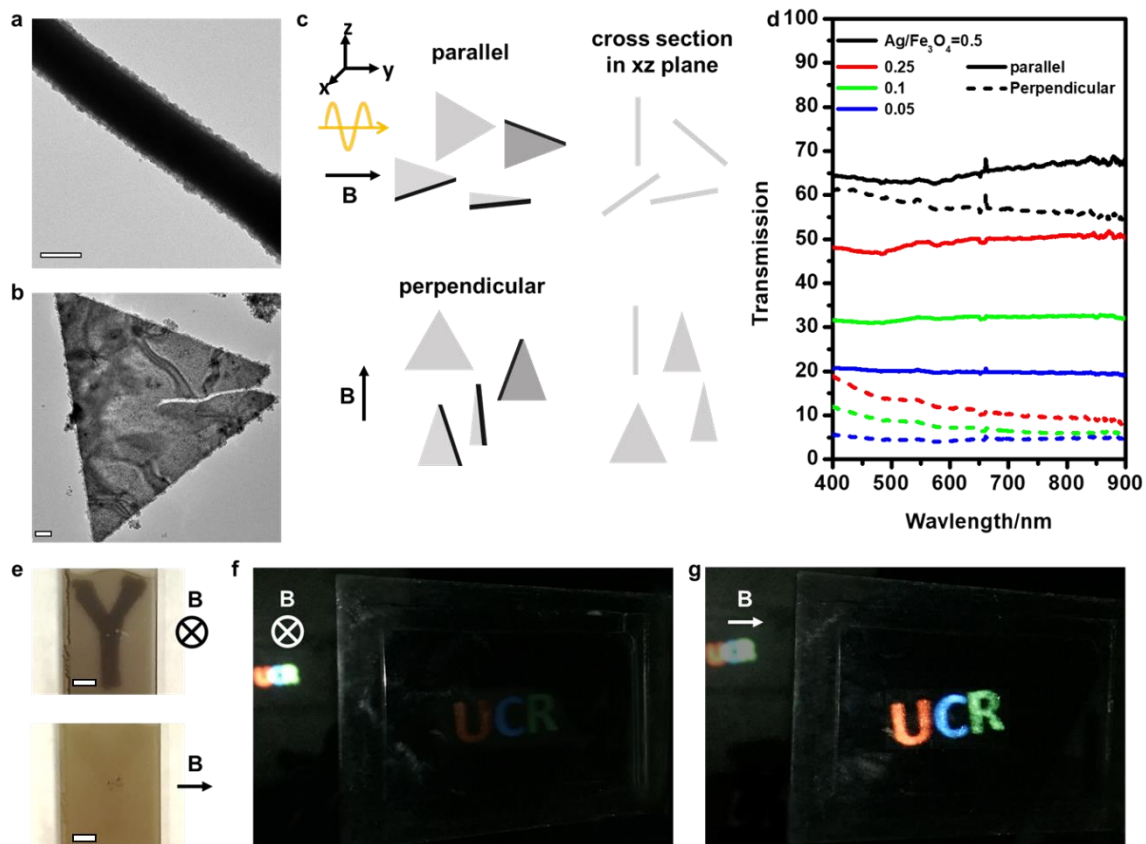


Figure 3.10 TEM images of (a) Ag@Fe₃O₄NWs and (b) Ag@Fe₃O₄PLTs. (c) Schematics showing the magnetic tuning and the cross-section difference of Ag@Fe₃O₄PLTs. (d) UV-vis spectra of Ag@Fe₃O₄PLTs with a magnetic field applied parallel and perpendicular to the incident light propagation direction. Digital images of (e) smart window above a letter “Y”, with a magnetic field applied in (top) out-of-plane and (bottom) horizontal direction and smart display device with a magnetic field applied (f) parallel and (g) perpendicular to incident light.

3.2.4 Conclusion

In summary, taking advantage of our previously reported CNC synthesis, we achieved the coating of Fe₃O₄ nanocrystals on pre-synthesized plasmonic nanostructures. Thanks to the small crystal size of the Fe₃O₄ nanocrystals, the crystal strain induced by the lattice mismatch could be minimized, and the self-nucleation of Fe₃O₄ could be avoided. The thickness of the Fe₃O₄ coating on the plasmonic nanoparticles could be tuned by changing the Au/Fe or Ag/Fe ratio in the synthesis. Due to the high surface energy of AuNPs, the nanoparticles formed assembly structures with uniform interparticle distance. Although the assembly structures were not expected, this could be a promising platform for SERS measurements. Since the structural strength of the assemblies was enforced by the Fe₃O₄ coating, the 3D assembly structures can provide a higher population of hot spots compared to a 2D array of AuNPs. In addition, the nanocomposites can be pulled to one side of the droplet during the drying process, which can serve as nucleation sites of the analytes, further enhancing the SERS signal of analytes in the dry state. When microstructures such as AgNWs and AgPLTs were subjected to the Fe₃O₄ coating process, the aggregation could be avoided. The magnetic tuning of the transmittance and scattering of AgPLTs was demonstrated, and a smart window and a smart display device were fabricated respectively to feature the dynamic tuning of the two optical properties. The performance of the smart window and the display could be improved with further optimization of device fabrication techniques. In addition, due to the micrometer size of the Ag@Fe₃O₄PLTs, the reflection difference could extend to the IR region; therefore, the smart window had potentials for magnetically controlled thermal management.

3.3 Reference

1. Zijlstra, P.; Chon, J. W. M.; Gu, M., Five-dimensional optical recording mediated by surface plasmons in gold nanorods. *Nature* **2009**, *459* (7245), 410-413.
2. Zhang, C.; Wu, Z.; Chen, Z.; Pan, L.; Li, J.; Xiao, M.; Wang, L.; Li, H.; Huang, Z.; Xu, A.-B.; Li, C.; He, L., Photonic nanostructures of nanodiscs with multiple magneto-optical properties. *Journal of Materials Chemistry C* **2020**, *8* (45), 16067-16072.
3. Zhang, H.; Zhang, J.; Tong, X.; Ma, D.; Zhao, Y., Light Polarization-Controlled Shape-Memory Polymer/Gold Nanorod Composite. *Macromolecular Rapid Communications* **2013**, *34* (19), 1575-1579.
4. Jung, I.; Yoo, H.; Jang, H.-J.; Cho, S.; Lee, K.; Hong, S.; Park, S., Fourier Transform Surface Plasmon Resonance (FTSPR) with Gyromagnetic Plasmonic Nanorods. *Angewandte Chemie International Edition* **2018**, *57* (7), 1841-1845.
5. Wang, M.; Gao, C.; He, L.; Lu, Q.; Zhang, J.; Tang, C.; Zorba, S.; Yin, Y., Magnetic Tuning of Plasmonic Excitation of Gold Nanorods. *Journal of the American Chemical Society* **2013**, *135* (41), 15302-15305.
6. Li, Z.; Jin, J.; Yang, F.; Song, N.; Yin, Y., Coupling magnetic and plasmonic anisotropy in hybrid nanorods for mechanochromic responses. *Nature Communications* **2020**, *11* (1), 2883.
7. Brulot, W.; Valev, V. K.; Verbiest, T., Magnetic-plasmonic nanoparticles for the life sciences: calculated optical properties of hybrid structures. *Nanomedicine: Nanotechnology, Biology and Medicine* **2012**, *8* (5), 559-568.
8. Wang, X.; Feng, J.; Yu, H.; Jin, Y.; Davidson, A.; Li, Z.; Yin, Y., Anisotropically Shaped Magnetic/Plasmonic Nanocomposites for Information Encryption and Magnetic-Field-Direction Sensing. *Research* **2018**, *2018*, 7527825.
9. Halas, N. J.; Lal, S.; Chang, W.-S.; Link, S.; Nordlander, P., Plasmons in Strongly Coupled Metallic Nanostructures. *Chemical Reviews* **2011**, *111* (6), 3913-3961.
10. Wang, M.; He, L.; Zorba, S.; Yin, Y., Magnetically Actuated Liquid Crystals. *Nano Letters* **2014**, *14* (7), 3966-3971.
11. Gao, C.; Vuong, J.; Zhang, Q.; Liu, Y.; Yin, Y., One-step seeded growth of Au nanoparticles with widely tunable sizes. *Nanoscale* **2012**, *4* (9), 2875-2878.
12. Chandra, S.; Frey Huls, N. A.; Phan, M. H.; Srinath, S.; Garcia, M. A.; Lee, Y.; Wang, C.; Sun, S.; Iglesias, Ò.; Srikanth, H., Exchange bias effect in Au-Fe₃O₄nanocomposites. *Nanotechnology* **2014**, *25* (5), 055702.

13. Sheng, Y.; Xue, J., Synthesis and properties of Au–Fe₃O₄ heterostructured nanoparticles. *Journal of Colloid and Interface Science* **2012**, *374* (1), 96-101.
14. Yu, H.; Chen, M.; Rice, P. M.; Wang, S. X.; White, R. L.; Sun, S., Dumbbell-like Bifunctional Au–Fe₃O₄ Nanoparticles. *Nano Letters* **2005**, *5* (2), 379-382.
15. Brollo, M. E. F.; López-Ruiz, R.; Muraca, D.; Figueroa, S. J. A.; Pirota, K. R.; Knobel, M., Compact Ag@Fe₃O₄ Core-shell Nanoparticles by Means of Single-step Thermal Decomposition Reaction. *Scientific Reports* **2014**, *4* (1), 6839.
16. Liu, B.; Zhou, J.; Zhang, B.; Qu, J., Synthesis of Ag@Fe₃O₄ Nanoparticles for Photothermal Treatment of Ovarian Cancer. *Journal of Nanomaterials* **2019**, *2019*, 6457968.
17. Ge, J.; Hu, Y.; Biasini, M.; Beyermann, W. P.; Yin, Y., Superparamagnetic Magnetite Colloidal Nanocrystal Clusters. *Angewandte Chemie International Edition* **2007**, *46* (23), 4342-4345.
18. Korte, K. E.; Skrabalak, S. E.; Xia, Y., Rapid synthesis of silver nanowires through a CuCl- or CuCl₂-mediated polyol process. *Journal of Materials Chemistry* **2008**, *18* (4), 437-441.
19. Zhang, Q.; Hu, Y.; Guo, S.; Goebel, J.; Yin, Y., Seeded Growth of Uniform Ag Nanoplates with High Aspect Ratio and Widely Tunable Surface Plasmon Bands. *Nano Letters* **2010**, *10* (12), 5037-5042.

Chapter 4 Non-Noble Metal Magneto-Plasmonic Nanoparticles For Solar Steam

Generation

4.1 Introduction

Over the past decade, more than 40% of the world's population has lived in water-stressed areas, and this number is expected to rise to two-thirds by 2025.¹ In addition, a global population increase of 80 million each year calls for new sources of freshwater. The desalination of seawater is considered an essential part of the solution to global water stress. However, despite considerable efforts to improve pre-existing processes, seawater desalination is still highly energy consuming. Solar energy-based steam generation methods have gained increasing attention for low energy-consuming clean water generation. In this scheme, photothermal materials harvest the solar irradiation and convert it to heat, promoting the evaporation of surrounding water.²⁻⁵

In addition to the design of evaporator devices and heat isolation strategies,^{3, 6-12} the development of light absorbers is critically important in achieving high efficiency in steam generation. It is crucial to find light-absorbing materials that can make the best use of sunlight by maximizing the absorption and minimizing the reflectance of the light. Most solar steam generation strategies employ carbon as light-absorbing material because of its broadband absorption in the UV and visible region. However, due to graphite's birefringence property, light is strongly scattered when it is incident perpendicular to the cleavage planes, which limits the photothermal efficiency of graphite intrinsically. Other forms of carbon-based materials such as graphene, graphene oxide, and carbon nanotubes require considerably complicated synthesis and purification processes, although the

absorption efficiency may be improved.^{7, 13-16} On the other hand, plasmonic nanoparticles are well known for strong absorption at their plasmonic resonance wavelengths, resulting in a strong photothermal property. However, typical plasmonic particles consisting of noble metals such as Au and Ag show narrow absorption peaks in the visible region, which limit their applications in solar energy harvesting.¹⁷ Therefore, specially designed structures are required to enable the coupling between particles to broaden the absorption peak of the plasmonic particles.¹⁸⁻²¹ Although most attention was devoted to noble metals in the past studies due to their strong plasmonic properties, transition metal nanoparticles with broader plasmonic peaks are more suitable for harvesting solar energy.^{19, 22} Nickel nanoparticles, for example, exhibit plasmonic resonance peak at around 500 nm, showing great promises as a solar absorber.²³⁻²⁵ A composite material combining the high absorption ratio of small plasmonic particles with the broadband absorption of carbon is a desirable solution to designing a highly efficient solar energy harvesting material.

In this work, we report the rational design of Ni@C@SiO₂ core-shell nanoparticles that combine the broadband absorption of carbon and the plasmonic property of Ni for efficient solar thermal conversion. A solar steam generation device loaded with such nanoparticles can achieve a photothermal efficiency as high as 91.2% without additional structural design. Furthermore, the magnetic response of Ni allows the creation of surface textures on a polyvinyl alcohol (PVA) hydrogel film. The increased surface roughness and the evaporative area further enhance the performance of the solar steam generator, achieving an evaporation rate as high as 2.25 kg·m⁻²·h⁻¹. Thanks to the versatility and

stability provided by condensed SiO₂, the core-shell particles can be readily applied to various steam generation systems as needed.

4.2 Experimental

4.2.1 Chemicals

Nickel (II) nitrate hexahydrate, oleic acid (OA, 90%), sodium borohydride, resorcinol, formaldehyde (37% by weight in water), polyvinylpyrrolidone (PVP, Mw. 10000), tetraethyl orthosilicate (TEOS, 98%), polyvinyl alcohol (PVA, Mw. 31000 ~ 50000), and glutaraldehyde (50 wt.% in water) were purchased from Sigma-Aldrich. Sodium dodecyl sulfate (SDS), methanol, ammonium hydroxide (NH₃·H₂O, 28% by weight in water), diethylamine (DEA), and hydrochloric acid (HCl, 37%) were purchased from fisher scientific. Ethanol (200 proof) was purchased from Decon Laboratories Inc. All chemicals were directly used without further purification.

4.2.2 Synthesis of Ni Nanoparticles (NiNPs)

Ni NPs were synthesized following our previously reported method with modification²³. In a typical synthesis, a growth solution was prepared at room temperature by adding 20 mL of SDS (0.1 M), 2 mL of OA (0.01 M in methanol), and 20 mL of Ni(NO₃)₂ (0.01 M) into 160 mL of DI water. Fresh NaBH₄ (32 mg) was added to give a black color mixture. After 1h, Ni NPs were centrifuged (9000 rpm × 5 min) and dispersed in 10 mL of water.

4.2.3 Synthesis of Ni@C@SiO₂ NPs

For the synthesis of Ni@RF NPs, 10 mL Ni NPs dispersion was added into 18 mL of water in a round bottom flask. Then 28 μL of formaldehyde and 20 mg of resorcinol

were added, followed by 100 μL of diluted ammonia (2.8%). The mixture was heated at 50 $^{\circ}\text{C}$ for 1 h, then further heated at 100 $^{\circ}\text{C}$ for 3 h for RF condensation. The particles were centrifuged (9000 rpm \times 5 min) and washed with water twice, and dispersed in 10 mL of water.

Before SiO_2 coating, Ni @RF NPs were modified with MnO_2 by adding 200 μL of KMnO_4 (0.01 M) solution and stirred for 1 h. The modified particles were then centrifuged, washed with water twice, and dispersed in 10 mL of water. The particle dispersion was then injected into 100 mL of ethanol, mixed with 80 μL TEOS. Into the mixture, 5 mL of concentrated ammonia (28%) was injected to catalyze the reaction. The mixture was sonicated for 5 min then stirred for 40 min at room temperature, and the particles were separated through centrifugation (8000 rpm \times 5 min) and washed with ethanol twice to remove ammonia and unreacted TEOS. The particles were placed in a porcelain boat and dried under an IR lamp before they were annealed at 600 $^{\circ}\text{C}$ in N_2 for 2 h. The sample was then dispersed in 20 mL of water and boiled for 3 h to improve the dispersity. Finally, the particles were centrifuged (9000 rpm \times 5 min) and dispersed in water.

4.2.4 Synthesis of Ni@SiO₂ NPs

Ni NPs were modified by incorporating 2 mL of PVP (5 wt.%) and were vortexed for 30 min, then centrifuged and dispersed in 12 mL of water. The above Ni NPs were injected into 80 mL of ethanol, sonicated, and then 2 mL of DEA and 0.6 mL of TEOS were added quickly. After 80 min, the Ni@SiO₂ NPs were centrifuged (9000 rpm \times 5 min), washed with ethanol and water. The particles were then dried under an IR lamp and annealed at 600 $^{\circ}\text{C}$ in N_2 for 2 h. The sample was then dispersed in 20 mL of water and

boiled for 3 h to improve the dispersity. Finally, the particles were centrifuged (9000 rpm \times 5 min) and dispersed in water.

4.2.5 Synthesis of C@SiO₂ NPs

RF spheres with a radius of 80 nm were first synthesized by incorporating 14 μ L formaldehyde, 10 mg resorcinol in 28 mL of water, followed by injection of 100 μ L of diluted ammonia solution (2.8%). The mixture was stirred at room temperature for 12 h, then heated at 100 °C for 3 h for RF condensation. The particles were centrifuged (8000 rpm \times 3 min) and washed with water twice, then dispersed in 10 mL of water. The SiO₂ coating and high temperature anneal process followed the same protocol as Ni@C@SiO₂ NPs, and the final product was dispersed in water.

4.2.6 Fabrication of Ni@C@SiO₂/PVA Composite Film

Various amounts of Ni₄₀C₂₀ NPs were mixed with 0.1 g 5% PVA solution, followed by the addition of 2.5 μ L 50% glutaraldehyde solution. For initiating the gelation, 10 μ L of 1 M HCl was added to the mixture. A film was fabricated with a doctor-blade method with a magnetic field (400 mT) applied underneath the sample.

4.2.7 Solar Steam Generation Measurement

In measuring the weight change of the water during the evaporation process, a 50-mL beaker full of water was placed on a retort stand below the solar simulator with a light condenser. A piece of melamine foam was floating on the surface of the water. The nanoparticles were deposited on an MCE filter membrane (0.2 μ m pore size) then placed on top of the melamine foam. One sun irradiation (1 kW \cdot m⁻²) was employed to illuminate perpendicularly onto the filter membrane. The weight change was instantaneously recorded

as a function of time by the electronic balance. The ambient temperature was maintained at 21 °C, and the humidity was 30% RH throughout the measurement.

Before and after solar illumination, the surface temperatures were measured using an IR camera (FLIR ONE PRO). The temperature reading of the IR camera was calibrated using a thermocouple. The measurement uncertainty of the calibrated IR camera is ~1.0 °C in the studied temperature range.

4.2.8 Characterization

The sample morphology was characterized by a Tecnai 12 transmission electron microscopy (TEM). Scanning transmission electron microscopy (STEM) images and energy-dispersive X-ray spectroscopy (EDX) mapping profiles were collected on a ThermoFisher Scientific (formerly FEI/Philips) Titan Themis 300 transmission electron microscope operated at 300 kV. The morphology of the PVA/Ni40C20 composite was characterized by an FEI Nova NanoSEM 450 scanning electron microscope (SEM). X-ray diffraction (XRD) tests were performed with a Rigaku TTR III. UV-Vis spectra were measured with an Ocean Optics HR2000 CG-UV-NIR spectrometer. The reflectance spectra were measured with an Ocean Optics HR2000 CG-UV-NIR spectrometer with an integration ball.

4.2.9 Calculation of Energy Loss

The heat loss by the absorber consists of three parts: (i) radiation, (ii) convection, and (iii) conduction.

Radiation It is assumed that the emissivity of the absorbers is 1. For radiation loss to the ambient, the radiation loss was calculated by Stefan–Boltzmann law,

$$P = \varepsilon A \sigma (T_1^4 - T_2^4), \quad (4.1)$$

where P denotes heat flux, ε is emissivity, A is surface area, σ is the Stefan–Boltzmann constant, T_1 is the average temperature of the absorber, and T_2 is the ambient temperature.

Convection The convection loss was calculated by Newton’s law of cooling,

$$Q = hA\Delta T, \quad (4.2)$$

where Q denotes the heat, h is the convection heat transfer coefficient, A is surface area, and ΔT is the difference between the absorber and ambient temperature. The convection heat transfer coefficient is estimated, according to W. H. McAdams’ method²⁶.

Conduction The solar steam generator was put in a Dewar container under one-sun irradiation to calculate the conduction loss. The conduction loss was calculated based on

$$Q = Cm\Delta T, \quad (4.3)$$

where Q denotes the heat, C is the specific heat capacity of water ($4.2 \text{ J} \cdot \text{g}^{-1} \cdot \text{K}^{-1}$), t is the irradiation time, m is the mass of water, and ΔT is the elevated water temperature within t seconds. Based on the experiment, $t = 3600 \text{ s}$, $m = 50 \text{ g}$.

4.2.10 Calculation of Photothermal Efficiency of Nanoparticles in Solution

The photothermal conversion efficiency (η) of nanoparticles was calculated according to the previously reported methods,²⁷ detailed measurements as following:

In a small beaker, 10 g of Ni40C20 dispersion in water (10 $\mu\text{g}/\text{mL}$) was added. At this concentration, the transmissions of all solutions were 0% to ensure all light has been absorbed by the solution. The solutions were illuminated with a solar simulator, and the

temperature changes were monitored with a thermal couple sensor. The solutions were illuminated under a solar simulator for 4500 s to achieve equilibrium temperature, after which the light was turned off, and the cooling behavior of solutions was recorded.

During the photothermal heating process, the total energy balance for the system can be expressed as:

$$\sum_i m_i C_{p,i} \frac{d\Delta T}{dt} = Q_{NF} + Q_S - Q_{Loss} \quad (4.4)$$

Where m (g) represents the mass of the solution (m_s) and beaker (m_b), C (J/(g·°C)) includes the constant-pressure heat capacity of solution (C_s) and beaker (C_b), ΔT (°C) is the difference between the solution temperature T at time t and the starting solution temperature T_0 , Q_{NF} (W) is determined as the energy arising from the nanoparticles, and Q_{Loss} (W) is the thermal energy lost to the surrounding environment. In addition, Q_S (W) is the energy input by the beaker and the solvent (pure DI water). For Q_{NF} , Equation 4.5 can be given as:

$$Q_{NF} = IA\eta \quad (4.5)$$

Where $I = 1000 \text{ W/m}^2$ is the input light power density of the solar simulator, $A = 0.00491 \text{ m}^2$ is the illuminated area, and η is known as the photothermal conversion efficiency. Furthermore, energy dissipation mainly occurs through heat conduction and thermal radiation. Q_{Loss} is linear with temperature for the outgoing thermal energy, then take the form of Equation 4.6:

$$Q_{Loss} = hS\Delta T = hS(T - T_{Surr}) \quad (4.6)$$

Where h (W/(m² · °C)) is heat transfer coefficient, S (m²) is the surface area of the container, ΔT is the temperature change which is defined as $T - T_{Surr}$, T (°C) is the water

temperature, and T_{Surr} ($^{\circ}\text{C}$) is the ambient temperature of the surrounding environment. When the temperature rises to equilibrium temperature T_{Max} ($^{\circ}\text{C}$), the heat input is equal to heat output, and the left side of Equation 4.4 becomes zero. So we then obtain

$$Q_{NF} + Q_S = Q_{Loss} = hS(T_{Max} - T_{Surr}) \quad (4.7)$$

Then η can be determined by combining Equation 4.4-4.7 and rearranging:

$$\eta = \frac{hS(T_{Max}-T_{Surr})-Q_S}{IA} \quad (4.8)$$

Where Q_S is measured independently to be 0.102 W, the $(T_{Max}-T_{Surr})$ is 14.7 $^{\circ}\text{C}$. Thus, in Equation 4.8, only the hS remains an unknown parameter for calculating η . In order to solve hS , the following notation θ is used herein, which is defined as the ratio of $(T-T_{Surr})$ to $(T_{Max}-T_{Surr})$:

$$\theta = \frac{T-T_{Surr}}{T_{Max}-T_{Surr}} \quad (4.9)$$

And a sample system time constant τ_s (s) is introduced:

$$\tau_s = \frac{\sum_i m_i C_{p,i}}{hS} \quad (4.10)$$

Substituting Equations 4.9 and 4.10 into Equation 4.4 and rearranging to obtain:

$$\frac{d\theta}{dt} = \frac{1}{\tau_s} \left[\frac{Q_{NF}+Q_S}{hS(T_{Max}-T_{Surr})} - \theta \right] \quad (4.11)$$

When at the cooling stage of nanoparticle dispersion, the light source has been turned off (**Figure 3b**), so the $Q_{NF} + Q_S = 0$. Under this condition, Equation 4.11 becomes:

$$dt = -\tau_s(d\theta/\theta) \quad (4.12)$$

After integration Equation 4.12, the equation expresses as:

$$t = -\tau_s \ln(\theta) \quad (4.13)$$

Therefore, the time constant for heat transfer from the system is determined to be $\tau_s = 818$ s by applying the linear time data from the cooling period vs. $-\ln\theta$ (Figure S1). Thus, according to Equation 4.10, the hS is calculated to be 0.051 W/°C. Substituting $hS = 0.051$ W/°C into Equation 4.8, the result photothermal conversion efficiency (η) of Ni40C20 can be calculated to be 94.3%.

The photothermal efficiency of other samples was calculated with the same method.

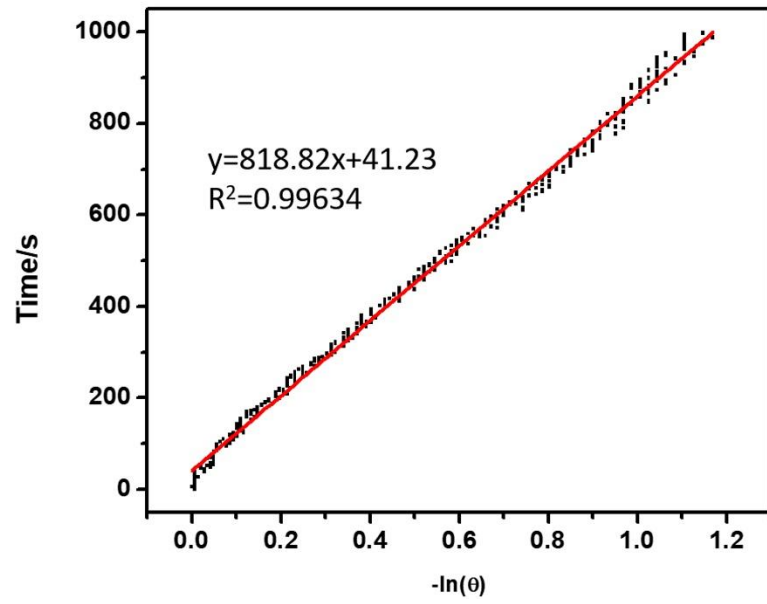


Figure 4.1 Linear time date vs. $-\ln(\theta)$ obtained from the cooling period of Ni40C20.

4.2.11 Calculation of Equivalent Vaporization Enthalpy

To obtain the effective evaporation enthalpy of water in PVA hydrogels, we used previously reported methods with slight modification.¹² In detail, pure water and PVA hydrogels having the same surface area were stored in a closed vessel with a humidity of 45% RH and a temperature of 25 °C. To avoid interference by sensible heat, it is necessary to control the experimental humidity at a high level, thereby suppressing the temperature changes caused by rapid evaporation.

The equivalent evaporation enthalpy of MPF-water can be calculated as follows:

$$E_{in} = \Delta H_{vap}m_0 = \Delta H_{equ}m_g \quad (4.14)$$

where ΔH_{vap} and m_0 are the evaporation enthalpy and mass change of pure water; m_g is the mass change of water in PVA. ΔH_{equ} is the real evaporation enthalpy and can be estimated by vaporizing the water with identical power input E_{in} . During the same evaporation period, the evaporation rate of water in 5% PVA is 1.21 times that of pure water, indicating that water in 5% PVA hydrogel has an evaporation enthalpy of 1884 J/g. Equivalent vaporization enthalpy of PVA hydrogels with different PVA content was calculated and summarized in Figure 4.19a.

4.3 Results and Conclusion

4.3.1 Synthesis of Ni@C@SiO₂ NPs and the Optimization of the Photothermal Performance

The Ni@C@SiO₂ particles were prepared via an indirect multi-step approach. The Ni nanoparticles were prepared by reducing Ni(NO₃)₂ with NaBH₄ and then coated with resorcinol formaldehyde (RF) and SiO₂ sequentially. Annealing at high temperatures in N₂ converted the RF into carbon. Amid the thermal treatment, the SiO₂ shell became more condensed, significantly enhancing the chemical stability of the particles. As shown in Figure 4.2a, the thickness of the carbon layer can be controlled by that of the RF layer, which can be well-tuned by adjusting the amount of resorcinol and formaldehyde precursors added into the system. Before being coated with silica, the Ni@RF particles were treated with KMnO₄ to generate a transitional layer to increase the affinity between the RF surface and silica.²⁸ The SiO₂ layer formed via the Stöber method was found to maintain the core-shell structure during the annealing process. As shown in Figure 4.2b-f, the Ni particles were stable throughout the synthesis, and the particle size and carbon thickness were very uniform. The high-angle annular dark-field (HAADF) image (Figure 4.2g) and EDX elemental mapping (Figure 4.2h) of the Ni@RF@SiO₂ nanoparticles confirmed our proposed core-shell structure. The XRD pattern of Ni@RF core-shell nanoparticles (Figure 4.3) showed a broad peak corresponding to Ni due to the low crystallinity of borohydride reduced Ni and contamination of boride species, which is consistent with previously reported results.²³ It is interesting to note that the RF layer can efficiently protect Ni particles from oxidation by strong oxidizing agents such as KMnO₄.

When excessive KMnO_4 was added, and RF was completely consumed, Ni nanoparticles will be oxidized and etched, leaving a hollow MnO_2 shell, as shown in Figure 4.4. While no gap between Ni and RF layer or shrinkage of Ni core in size could be observed at a low loading of MnO_2 , the Ni core remained intact after modification. After KMnO_4 treatment, a thin layer of MnO_2 could be observed in TEM (Figure 4.2d). Due to its small amount and low crystallinity, the MnO_2 layer showed no distinct peaks in the XRD pattern (Figure 4.3). However, the presence of Mn in the form of a thin layer can be confirmed in the EDX elemental mapping image (Figure 4.2h). Thanks to the surface modification of MnO_2 , a smooth and uniform silica coating was obtained (Figure 4.2e), and the particles underwent minimal morphology change during the thermal treatment (Figure 4.2f). Without the MnO_2 transitional layer, however, silica coating could be challenging as free SiO_2 nanoparticles formed dominantly instead (Figure 4.5). Before thermal treatment, the Ni NPs typically contain boride species and have poor crystallinity, thus showing almost no magnetic property. After annealing, the borides decomposed, and the crystallinity of the particles was significantly improved, exhibiting a much stronger magnetic response.²⁹ The XRD pattern of Ni@C@SiO_2 nanoparticles (Figure 4.3) showed a strong peak of Ni, confirming the enhanced crystallinity of Ni after the annealing process.

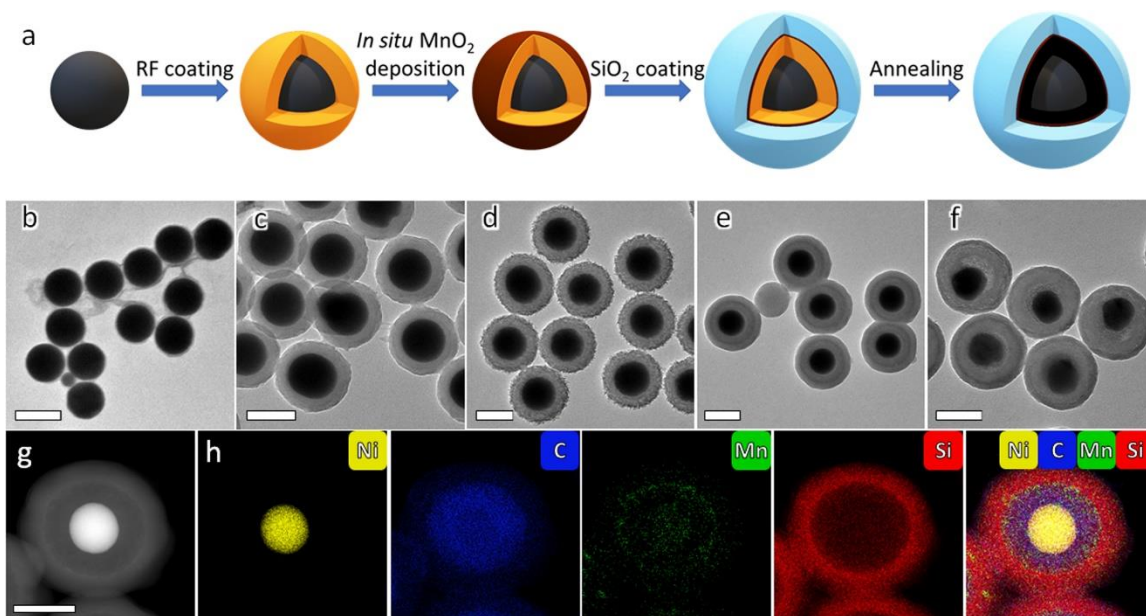


Figure 4.2 (a) Synthetic scheme of Ni@C@SiO₂ core-shell nanoparticles and (b-f) corresponding TEM images of the particles at each stage. (g) HADDF-STEM image and (h) EDX elemental mapping of Ni@RF@SiO₂ core-shell nanoparticles. Scale bars are 100 nm.

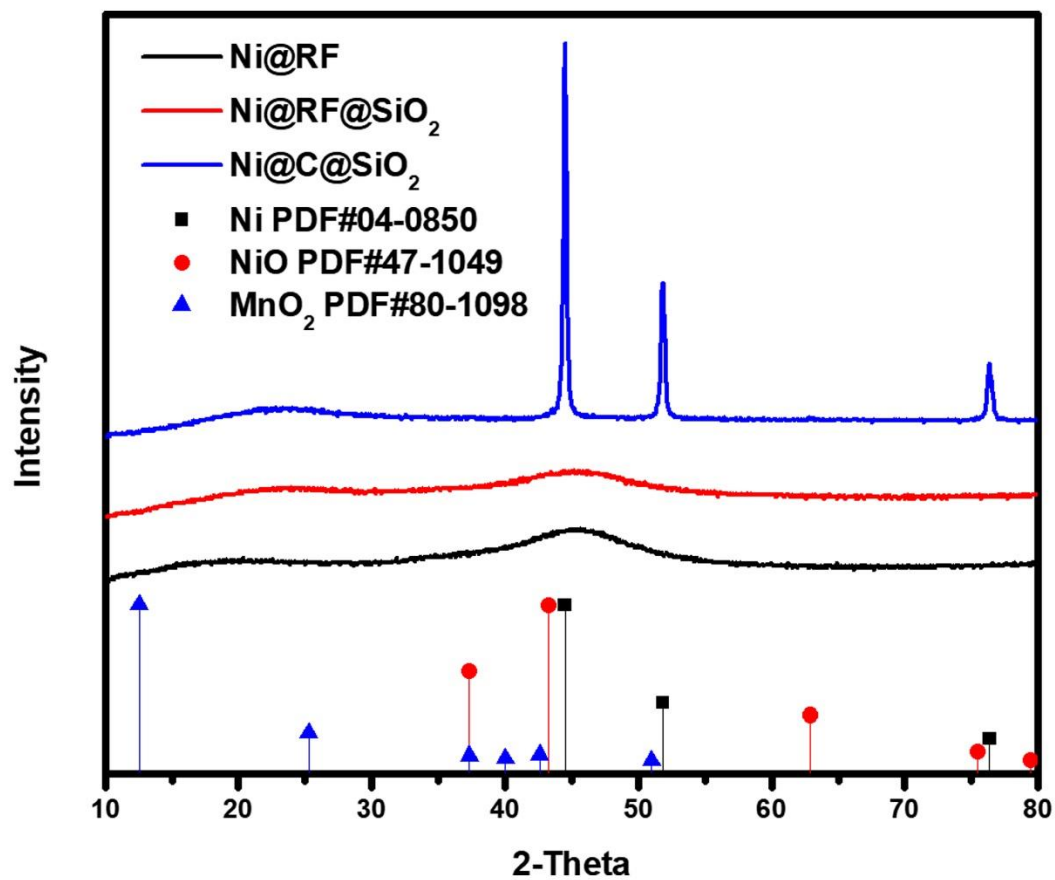


Figure 4.3 XRD pattern of Ni@RF, Ni@RF@SiO₂ and Ni@C@SiO₂.

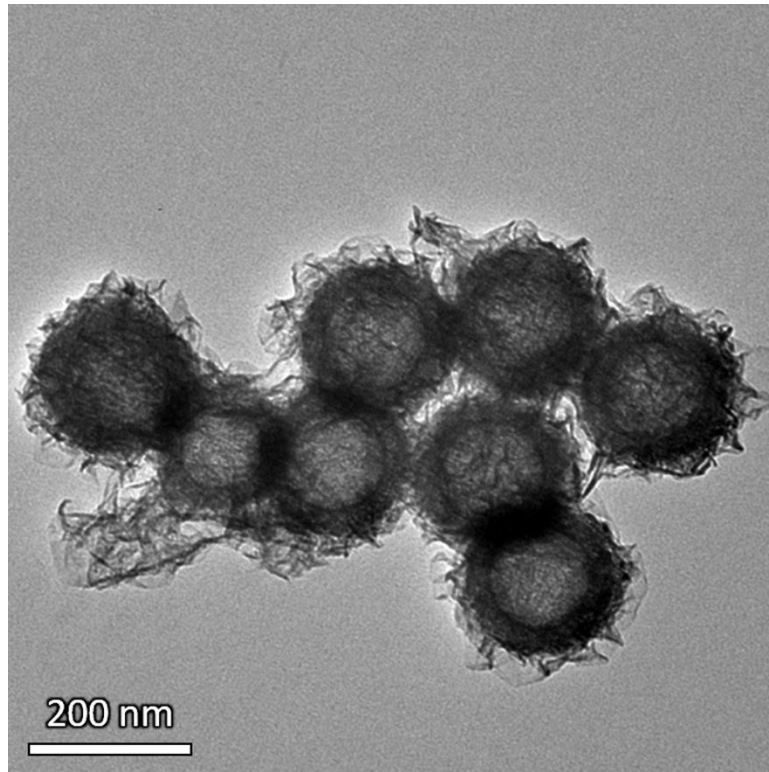


Figure 4.4 TEM of Ni@RF nanoparticles treated with excessive KMnO_4 .

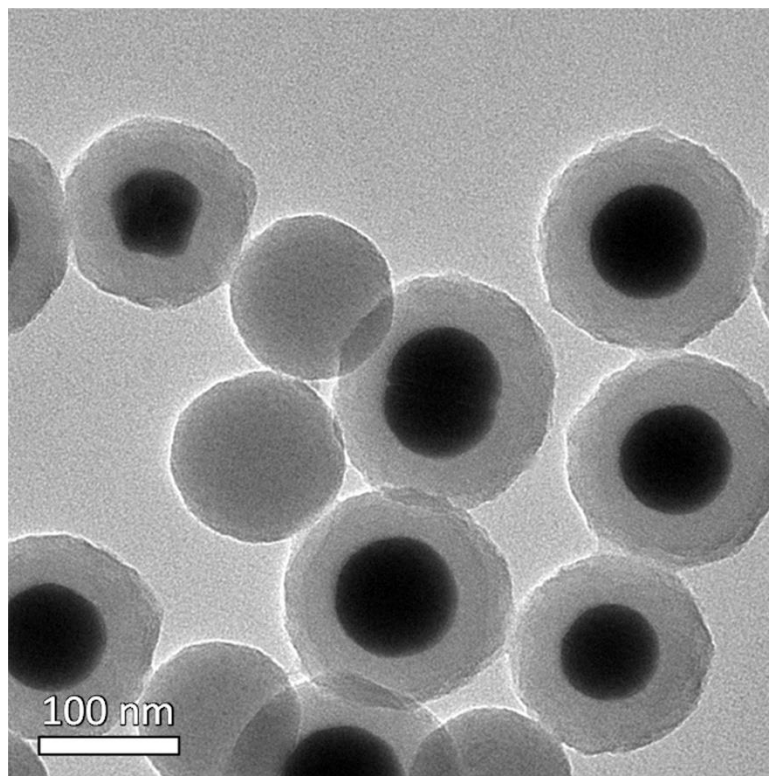


Figure 4.5 TEM of Ni@RF@SiO₂ nanoparticles without KMnO₄ treatment.

The optical properties of the core-shell nanoparticles were first simulated to optimize the radius of the Ni core and the thickness of the carbon shell. Figure 4.6a shows the simulated spectra of Ni@C core-shell nanoparticles with a core radius of 40 nm and various carbon thickness. The absorption spectrum of the carbon sphere was simulated as well for comparison. With the presence of Ni core, the absorption of the particle is greatly enhanced at around 550 nm, which matches the maximum peak of the solar irradiation spectrum. An absorption spectrum that overlaps with the energy distribution of the solar irradiation is of great importance since it maximizes the utilization of energy where solar energy is most concentrated. On the other hand, the carbon shell broadens the absorption peak of the particles and increases the absorption at longer wavelengths, expanding the range of energy that can be converted into heat. According to simulation, the absorption spectra can overlap with the solar irradiation spectrum very well when shell thickness is 20 nm. Beyond this point, increasing the shell thickness does not obviously increase the absorption at longer wavelengths, but the enhancement at 550 nm brought by Ni dramatically decreases. The ratio of absorption cross-section to extinction cross-section of each particle was calculated and shown in Figure 4.6b. All core-shell particles showed a higher absorption ratio when compared with pure carbon spheres. Since the photothermal properties only convert the energy that has been absorbed by the material, a higher absorption cross-section ratio enables a higher energy utilization efficiency. With the same Ni core radius, the absorption cross-section ratio gradually decreases with increasing carbon thickness (Figure 4.6b). It is interesting to find that compared with bare Ni nanospheres, Ni₄₀C₁₀ with 10 nm of carbon shell showed a higher absorption cross-

section ratio. The optimal carbon thickness is determined to be 20 nm since it allows a high overlapping degree of the absorption spectrum and the distribution of solar energy without severely compromising the absorption cross-section ratio. We further optimize the size of the Ni core by fixing carbon thickness at 20 nm. It is well known that the LSPR properties of plasmonic particles are dependent on their dimensions. As shown in Figure 4.6c, when the core size increases, the absorption peak redshifts, and the spectra can overlap well with the solar irradiation spectrum when the core radius is 40 nm. Although the absorption cross-section ratio goes down with increasing core size, as illustrated in Figure 4.6d, the influence of core size in the absorption ratio is much less dramatic than carbon shell thickness. Based on the simulation results, core-shell nanoparticles with a core radius of 40 nm and a carbon thickness of 20 nm (denoted as Ni40C20) were determined to be the optimal condition. For comparison, we also synthesized Ni@SiO₂ NPs with Ni radius of 40 nm, Ni@C@SiO₂ NPs with Ni radius of 20 nm and carbon thickness of 20 nm, Ni@C@SiO₂ NPs with Ni radius of 40 nm and carbon thickness of 40 nm, and C@SiO₂ NPs with carbon radius of 80 nm (denoted as Ni40, Ni20C20, Ni40C40, C80 respectively) via similar synthesis routes, and the morphologies were shown in Figure 4.7. As shown in the UV-vis spectra of prepared samples (Figure 4.6e), the extinction spectra of Ni40C20 overlaps with the solar spectra the best among all samples, which agrees well with the prediction of the simulated results. As indicated in the reflectance spectra of the samples in Figure 4.8, the carbon particles showed a relatively high reflection of ~14% throughout the whole visible region, while Ni40, Ni40C20, and Ni20C20 exhibited much lower reflectance (~5%).

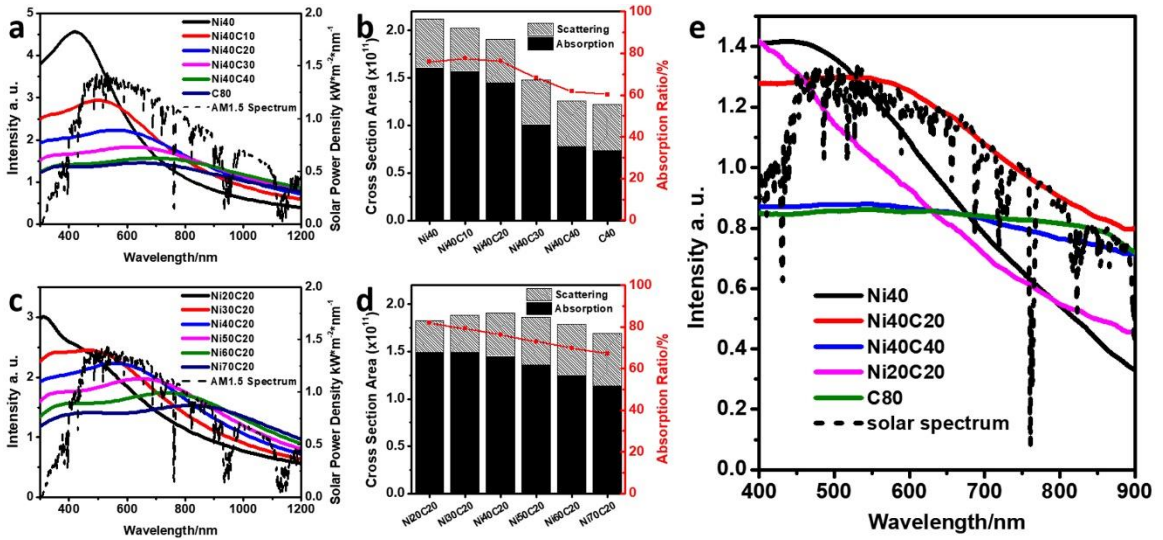


Figure 4.6 (a, c) Simulated spectra of Ni@C core-shell particles with (a) varying shell thickness and (c) core size, normalized by the number of moles of the substance. (b, d) Cross-section area and absorption ratio of particles corresponding to (a) and (c). (e) Extinction spectra of prepared samples with various Ni core size and carbon thickness in comparison to solar irradiation spectrum.

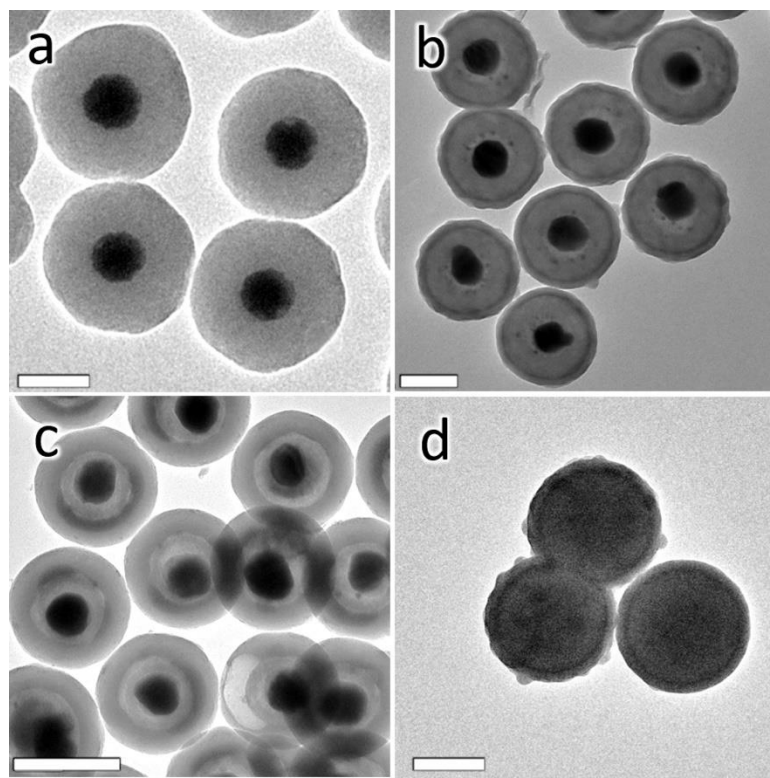


Figure 4.7 TEM images of (a) Ni₄₀, (b) Ni₄₀C₄₀, (c) Ni₂₀C₂₀, and (d) C₈₀ nanoparticles. Scale bars are all 100 nm.

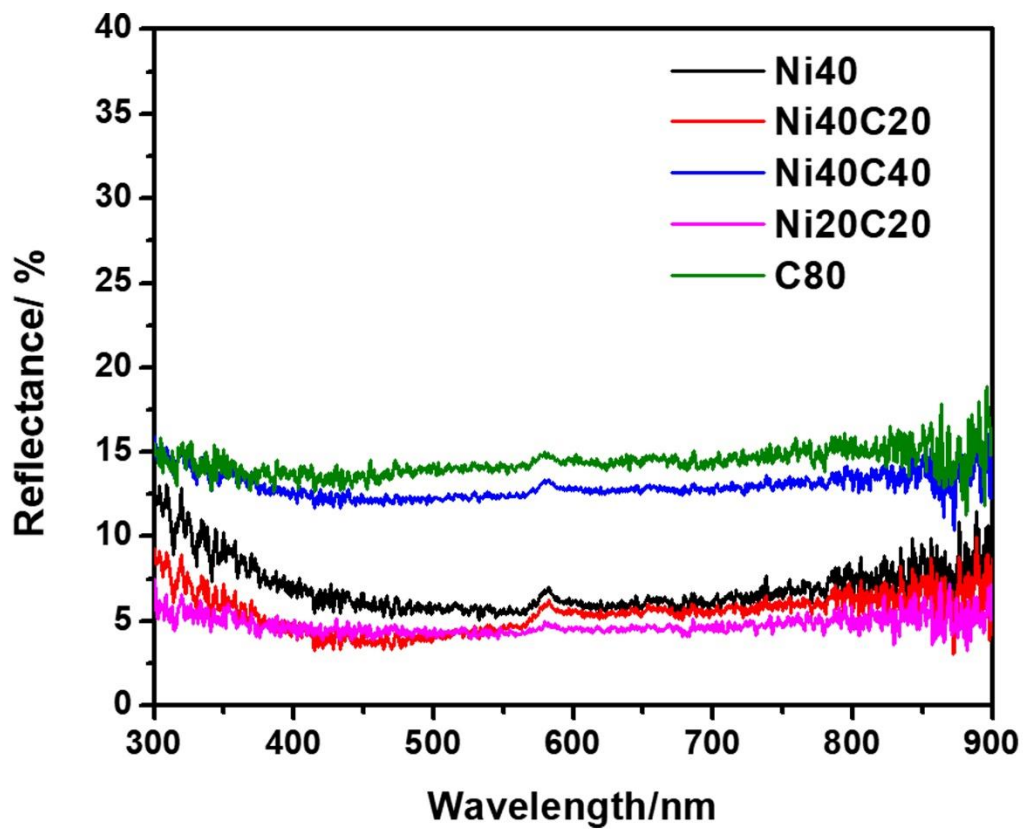


Figure 4.8 Reflectance spectra of the prepared samples.

For the prepared materials to be used in solar-driven steam generation devices, the photothermal property is one of the essential indicators of the effectiveness of a light absorber. The photothermal properties of prepared samples were characterized by a solar simulator. Each sample was deposited onto a mixed cellulose ester (MCE) membrane filter via vacuum filtration. The samples were then illuminated with one sun irradiation ($1 \text{ kW} \cdot \text{m}^{-2}$) to test the photothermal properties. The temperature change of each sample under light irradiation was monitored with an infrared camera, and the temperature profile was plotted in Figure 4.9a. Ni40C20 showed the highest temperature rising rate and reached the highest equilibrium temperature at $70.1 \text{ }^\circ\text{C}$ within 2 min of irradiation, while the same amount of C80 particles exhibits the lowest equilibrium temperature at $41.8 \text{ }^\circ\text{C}$. The significant difference clearly shows the advantage of the core-shell nanoparticles in solar absorption. Despite similarly low reflectance, Ni40 showed a much lower equilibrium temperature than Ni40C20. It can be observed from the extinction spectra (Figure 4.6e) that the peak of Ni40 is relatively narrow, so Ni40 is not able to utilize the energy in longer wavelengths. In comparison, the carbon layer in Ni40C20 not only broadened the absorption peak and increased absorption in longer wavelengths but makes the plasmonic peak of Ni red-shifted as well due to its high refractive index so that the absorption spectrum can better overlap with the solar irradiation spectrum. The importance of spectral selectivity can also be observed in the Ni20C20 sample. Although the Ni20C20 sample showed a slightly lower reflectance in the visible region, its maximum absorption peak was located at shorter wavelengths, which limited its photothermal performance. As a result, Ni20C20 also showed a lower equilibrium temperature under light illumination compared with Ni40C20.

The photothermal performance and spectra profiles of Ni40C40 particles were very similar to C80 sample because with a thick enough carbon shell, the optical properties of carbon dominate the profile, and the enhancement brought by Ni is minimal.

The samples were then dispersed in solution to quantify the photothermal efficiency. The dispersion was illuminated under a solar simulator until the temperature reaches equilibrium. The temperature change during both heating (light on) and cooling (light off) processes was monitored with a thermal couple sensor, as shown in Figure 4.9b. The photothermal efficiencies of the prepared nanoparticles were further calculated and summarized in Figure 4.9c. Samples dispersed in water showed the same trend as the dry samples, where Ni40C20 exhibited the highest temperature elevation, and C80 showed the lowest. When the temperature of the solutions reaches equilibrium, the heat produced through the photothermal effect equals the heat dissipated into the surroundings. Therefore, the photothermal efficiency η can be calculated by the equation:

$$\eta = \frac{hS(T_{max}-T_0)-Q_{in,water}}{IA} \quad (4.15)$$

where h is the heat transfer coefficient, S is the surface area, T_{max} is the equilibrium temperature of the solution, T_0 is the ambient temperature, $Q_{in, water}$ is the heat produced by water without particles, I is the input power density of solar simulator, and A is the illuminated area. The photothermal efficiency of the Ni40C20 sample was calculated to be 94.3%, while the pure carbon sample only raised the temperature of water by 7.0 °C, giving a photothermal efficiency of 58.7%.

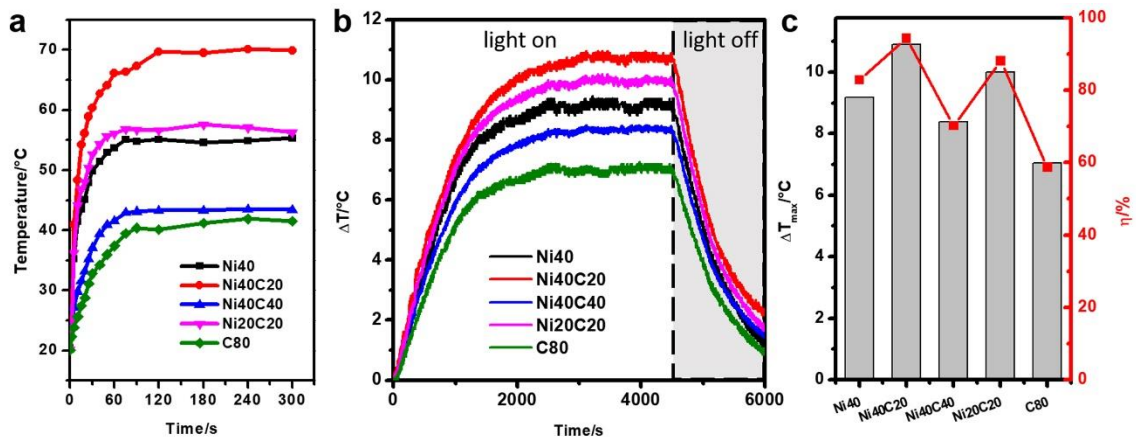


Figure 4.9 (a) Temperature change over time when different films were subjected to the illumination of the solar simulator. (b) Temperature variation over time of the nanostructure dispersion (1 $\mu\text{g}/\text{mL}$) in response to light irradiation. The light was turned off after 75 min of irradiation. (c) Maximum temperature elevation at equilibrium and photothermal efficiency of the prepared nanoparticles.

We applied the as-prepared particles to a membrane-filter-based steam generator to assess the performance of each sample. As demonstrated in the scheme (Figure 4.10a), the steam generator consists of melamine foam as the support and a membrane filter loaded with different particles as a light absorber. The melamine foam was chosen to be the support due to its porous structure and high hydrophilicity, which guaranteed an efficient water supply. In the meantime, it localized the heat on the top region by blocking thermal radiation and slowing down convection through “tortuosity effect”.^{12, 30} The optical image of the steam generator is shown in Figure 4.10b. The diameter of the evaporator was 5 cm, which was mainly limited by the size of the membrane filter. In principle, a larger evaporator can be prepared if a larger membrane is available. As shown in Figure 4.10c, after 15 min of illumination, the heat was well confined on the top region, and the bulk water remains the same temperature as the ambient. The steam generation performances of the particles were evaluated by plotting the mass change against the illumination time under the solar simulator. As shown in Figure 4.10d, the Ni40C20 sample showed the steepest slope and exhibited the best performance of $1.67 \text{ kg}\cdot\text{m}^{-2}\cdot\text{h}^{-1}$. After eliminating the contribution of water evaporation without light irradiation, the mass change of water and photothermal efficiency after 1 h of illumination under a solar simulator was summarized in Figure 4.10e. The apparent energy conversion efficiency of Ni40C20 reaches 91.2%. As predicted, the Ni40 and Ni20C20 showed lower efficiency while Ni40C40 and C80 ranked the lowest.

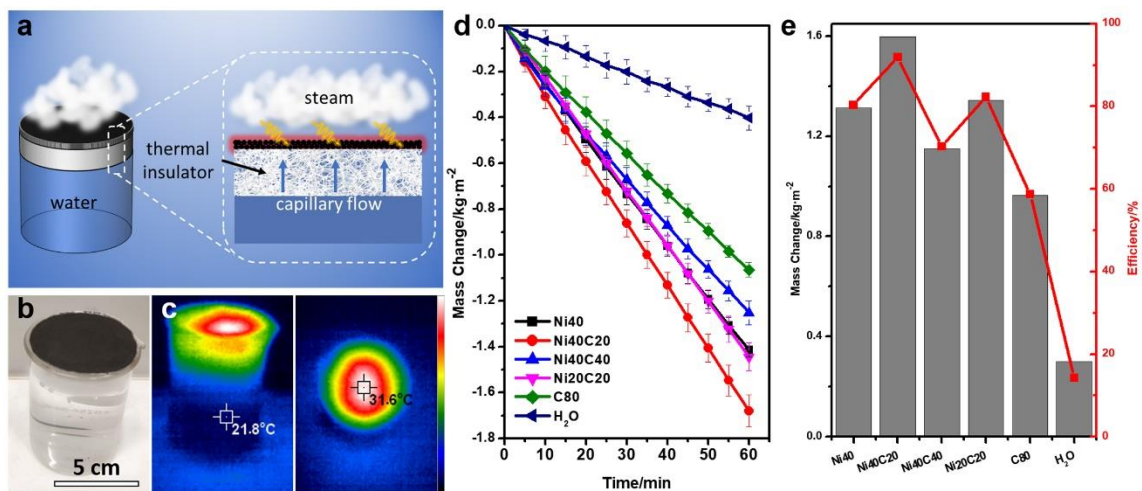


Figure 4.10 (a) Schematic illustration of the solar steam generation process. (b) Digital photo of the solar evaporator. (c) Side and top view of IR thermal images of water beakers recorded by a thermal camera after being irradiated with a solar simulator for 15 min. (d) Time course of water evaporation performance with different samples. (e) Steam generation rate and efficiency of different samples.

With the protection of the densified SiO₂ layer, Ni₄₀C₂₀ stayed considerably stable; no morphology changes (Figure 4.11) nor obvious decay in steam generation performance can be observed after 6 cycles of tests in both pure water (Figure 4.12a) and artificial seawater (Figure 4.13a). The nanoparticle-based steam generator also exhibited steady performance during 8 h of continuous illumination (Figure 4.13b), and the particles' morphology remained stable in the seawater environment (Figure 4.14). It is worth noting that the SiO₂ layer improved the stability of the nanoparticles and played an essential role in the enhancement of steam generation efficiency. The hydrophilicity of the SiO₂ layer allowed water to better wet the particles, resulting in a more efficient heat exchange between particles and surrounding water. As shown in Figure 4.12b, after SiO₂ was etched away, the steam generation performance of Ni₄₀C₂₀ significantly decreased. The Ni₄₀C₂₀ without silica layer also exhibited a higher equilibrium temperature on the evaporative surface (Figure 4.12c) than the sample with the SiO₂ layer. Since SiO₂ did not contribute to the photothermal property, it can be concluded that the increased efficiency is due to the promoted heat exchange process. As shown in Figure 4.15, the water contact angle increased from 60° to 98° after SiO₂ etching, indicating the shift of Ni₄₀C₂₀ particles from hydrophilic to hydrophobic. Upon removing SiO₂, the hydrophobicity of carbon hinders the wetting of particle surfaces, and less heat can be directly absorbed by water. The elevated temperature of the light absorber resulted in a more severe energy loss via thermal radiation and facilitated the convection heat loss on the top surface.

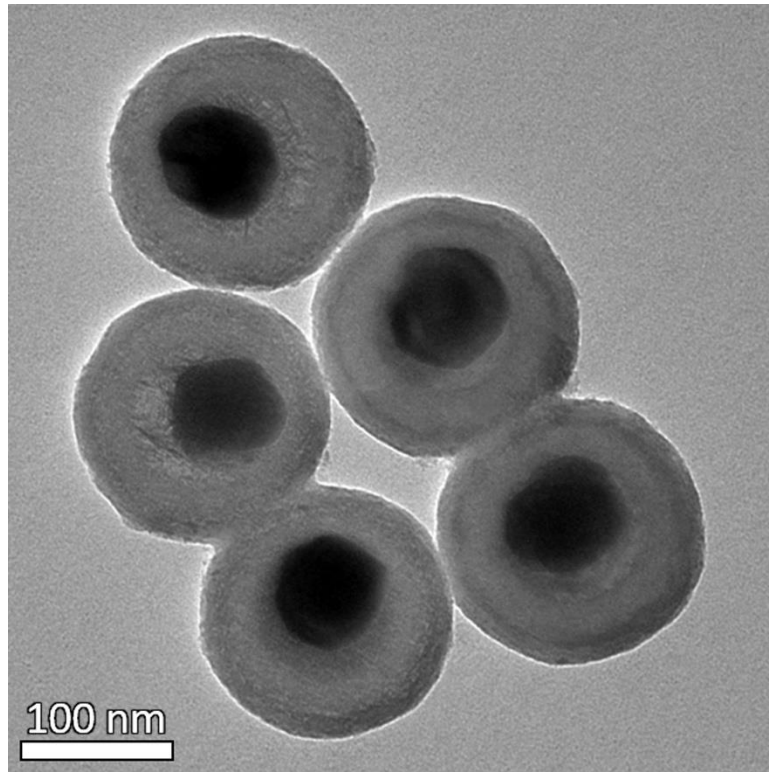


Figure 4.11 TEM image of Ni₄₀C₂₀ after 6 cycles of steam generation.

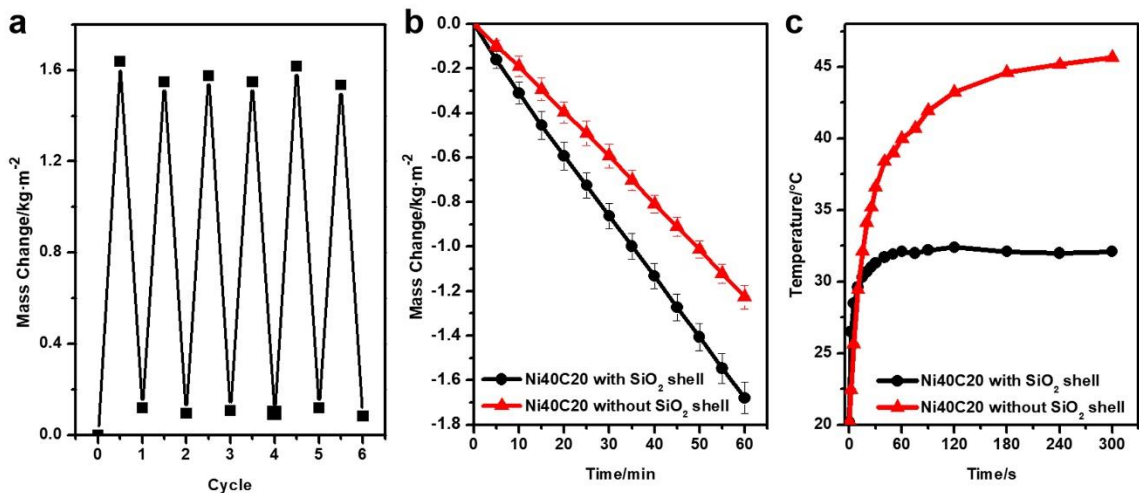


Figure 4.12 (a) Cycling performance of Ni40C20. (b) Steam generation performance of Ni40C20 with or without SiO₂ shell. (c) Change of surface temperature of Ni40C20 with or without SiO₂ shell.

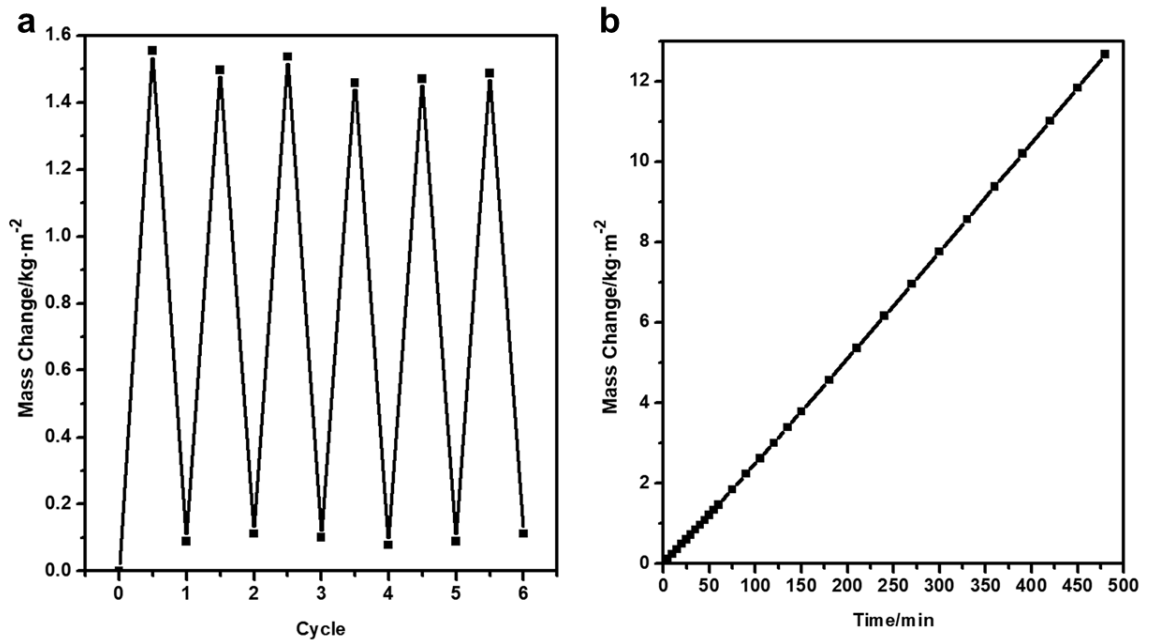


Figure 4.13 (a) Cycling performance of Ni40C20 in artificial seawater. (b) Steam generation performance of Ni40C20 in seawater under continuous solar illumination.

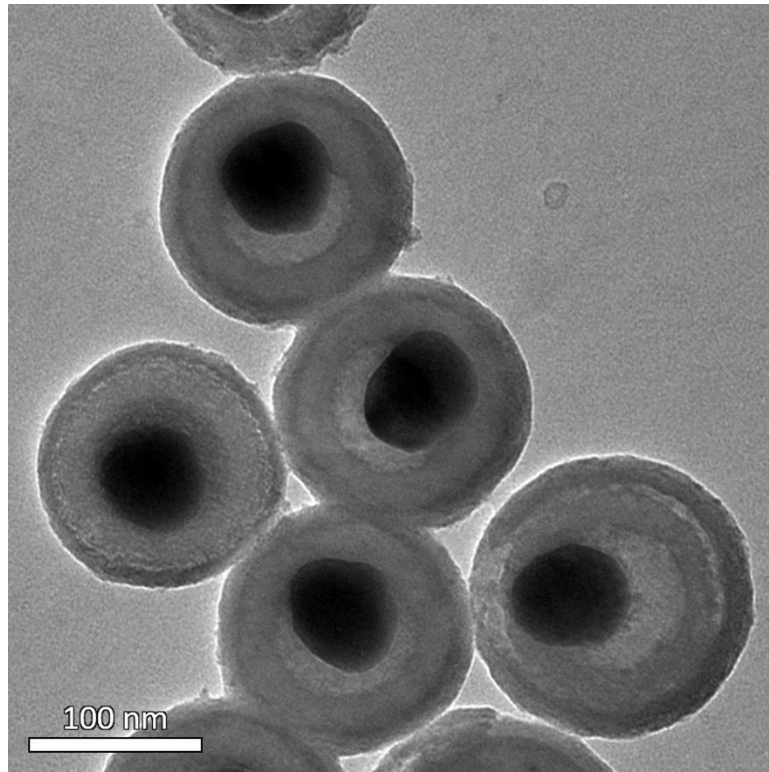


Figure 4.14 TEM image of Ni₄₀C₂₀ sample after 8 h of steam generation test in artificial seawater.

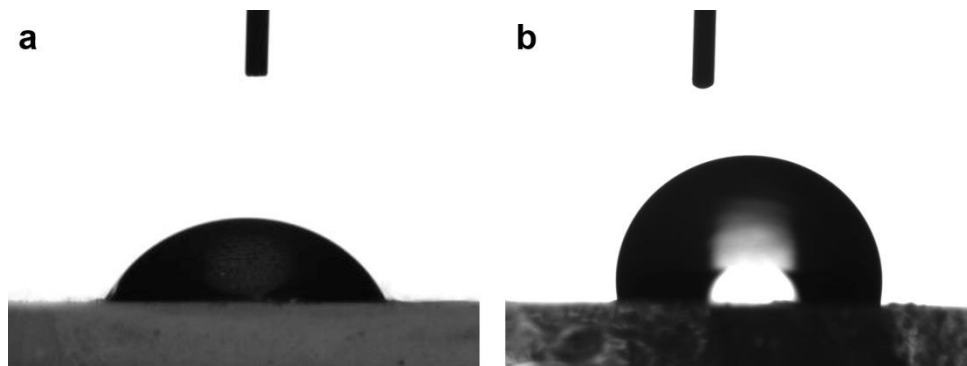


Figure 4.15 Water contact angle of Ni40C20 (a) with and (b) without SiO₂ layer.

4.3.2 Enhancing the Solar Steam Generation Performance with Magnetically Actuated Microstructures

Another essential feature that our core-shell design can offer is the magnetic property of Ni NPs. Hydrogel-based evaporators have exhibited exceptional performances in solar-driven water evaporation due to their ability to tune the evaporation enthalpy.^{8, 31-33} Thanks to the magnetic property of Ni NPs, we can easily tune the surface roughness of a hydrogel film with an external magnetic field and further promote the evaporation rate. As shown in the hysteresis loop of Ni₄₀C₂₀ (Figure 4.16), the core-shell nanoparticles exhibited relatively strong magnetic properties after annealing. The particles can also be easily collected with a magnet.

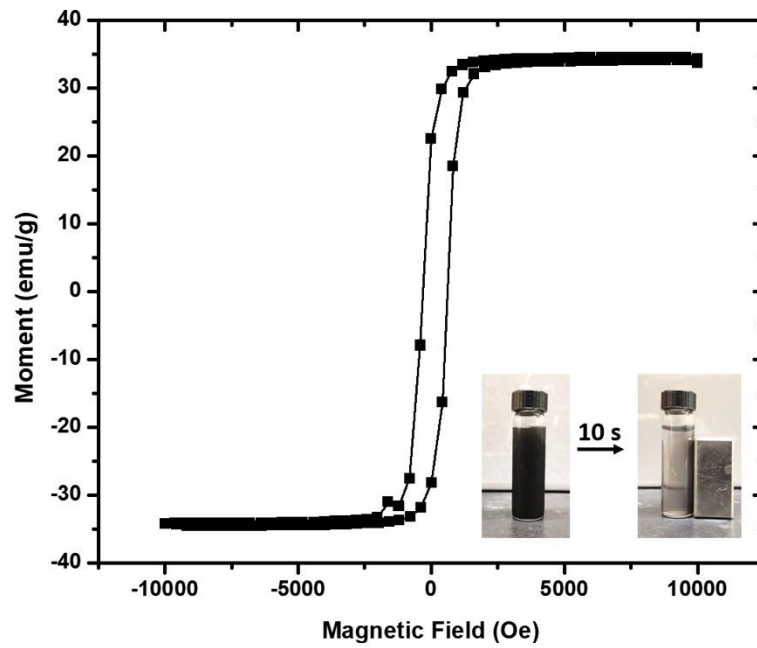


Figure 4.16 Room temperature hysteresis loop of Ni₄₀C₂₀. Inset is the optical image showing the magnetic collection of Ni₄₀C₂₀, all particles will be attracted to one side within 10 s.

Here we took PVA hydrogel as an example and incorporated the Ni40C20 nanoparticles into the PVA hydrogel substrate to make a PVA/Ni40C20 composite hydrogel film. The composite films with particle concentration of 20 wt.%, 30 wt.%, and 40 wt.% (denoted as M-20, M-30, and M-40, respectively) were prepared with a doctor-blade method with a magnetic field applied perpendicular to the film. As shown in Figure 4.17a-c, the hydrogel surface became rougher with increasing concentration of the magnetic particles. Figure 4.18 shows the SEM images of M-40 prepared under different magnetic field strengths. With increasing magnetic field strength, both the population and the height of microstructures increased. When the magnetic field was below 100 mT, the surface remained relatively flat. These results confirmed the relation between the surface microstructures and the magnetic properties of Ni40C20. The steam generation performance of the films with different particle concentration was summarized in Figure 4.17e. The steam generation rate increased with the increasing concentration of the particles, and the evaporation flux could reach as high as $2.25 \text{ kg}\cdot\text{m}^{-2}\cdot\text{h}^{-1}$ when the particle concentration was 40 wt.%. Further increasing particle concentration makes it challenging to prepare composite hydrogel films due to the dramatically increased viscosity of the nanoparticle/hydrogel precursor mixture. The photothermal efficiency of the composite films was calculated by the equation:

$$\eta = \frac{(m - m_{\text{dark}})H_{\text{vap}}}{IA} \quad (4.16)$$

where m is the mass flux of evaporated water, m_{dark} is the mass flux of evaporated water without light illumination, H_{vap} is the equivalent vaporization enthalpy of water, I is the input power density, and A is the illuminated area.

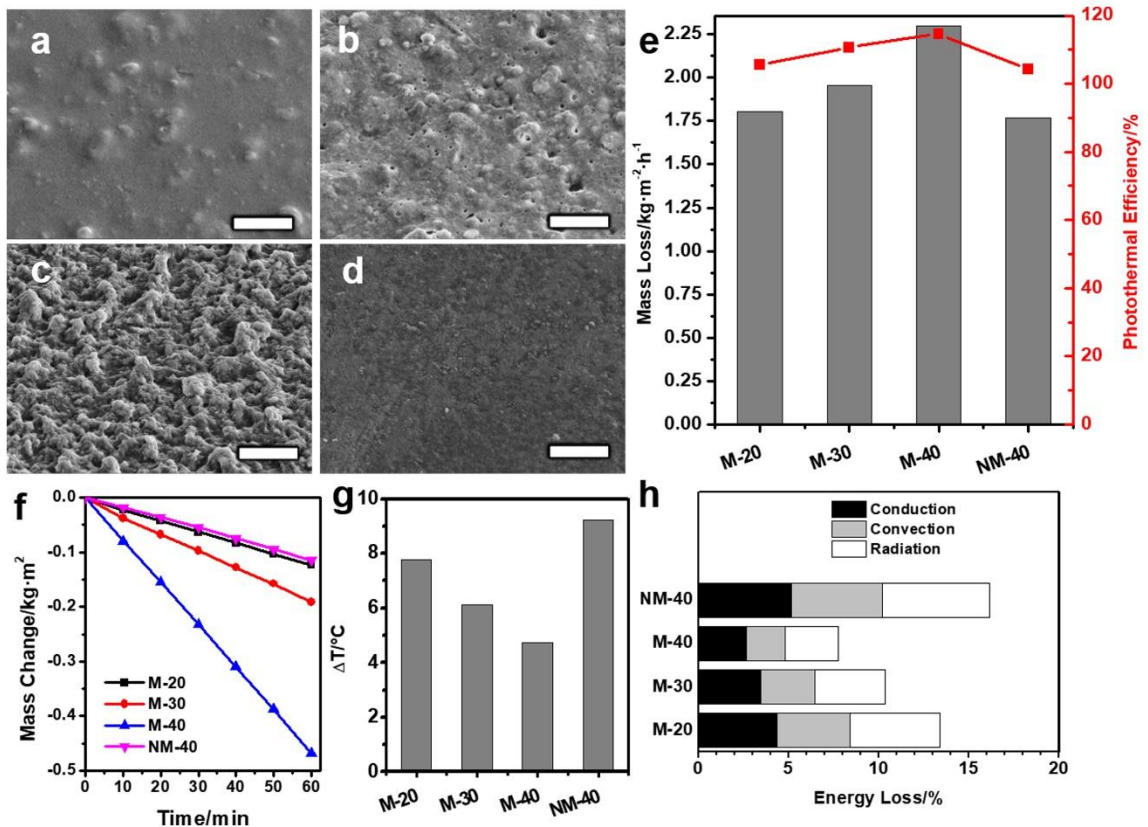


Figure 4.17 (a-d) SEM images of M-20, M-30, M-40, and NM-40 composite films. Scale bars are all 50 μm . (e) Steam generation rate and the apparent photothermal efficiency of different films. (f) Time-dependent mass change of water without light illumination at 20 $^{\circ}\text{C}$ on different films. (g) Temperature difference of film surface and ambient temperature after 1 h of light illumination. (h) Heat loss with respect to input energy during the steam generation process.

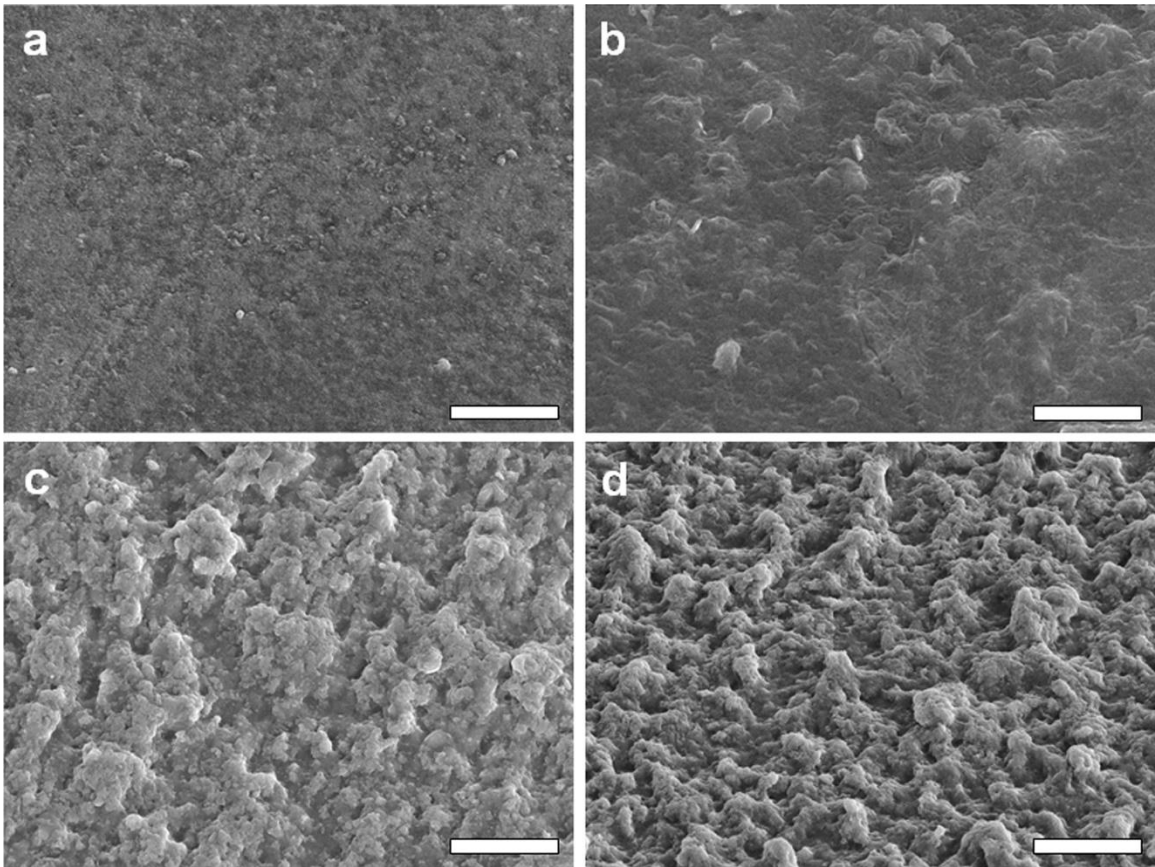


Figure 4.18 SEM images of PVA/Ni40C20 composite film (a) without magnetic field, with (b) 100 mT, (c) 200 mT, and (d) 400mT magnetic field applied during gelation process.

As shown in Figure 4.17e, the apparent photothermal efficiency exceeded 100% when vaporization enthalpy of bulk water was used in the calculation. However, the evaporation enthalpy of water changes when the substrate strongly interacts with water.³³ In this case, with 5% PVA hydrogel as the substrate, the vaporization enthalpy was calculated to be 1884 kJ·kg⁻¹ (Figure 4.19b), giving the highest photothermal efficiency of 95% for the M-40 sample. Although the loading density of particles on the surface might also contribute to the steam generation performance, without incorporating PVA hydrogel, the steam generation performance of directly deposited particles reached a plateau when loading density was higher than 20 g·m⁻², as illustrated in Figure 4.20. In the PVA/Ni40C20 composite films, the particle loading density ranged from 20 g·m⁻² to 40 g·m⁻². Therefore, the influence of loading density was neglectable. If there was no magnetic field applied during gelation (denoted as NM-40), the surface of the hydrogel remained flat, as shown in Figure 4.17d. Although the improved performance was also observed in NM-40 due to lowered vaporization enthalpy, it was far less dramatic than M-40. The significant improvement of the performance can be attributed to the increased surface roughness in M-40.

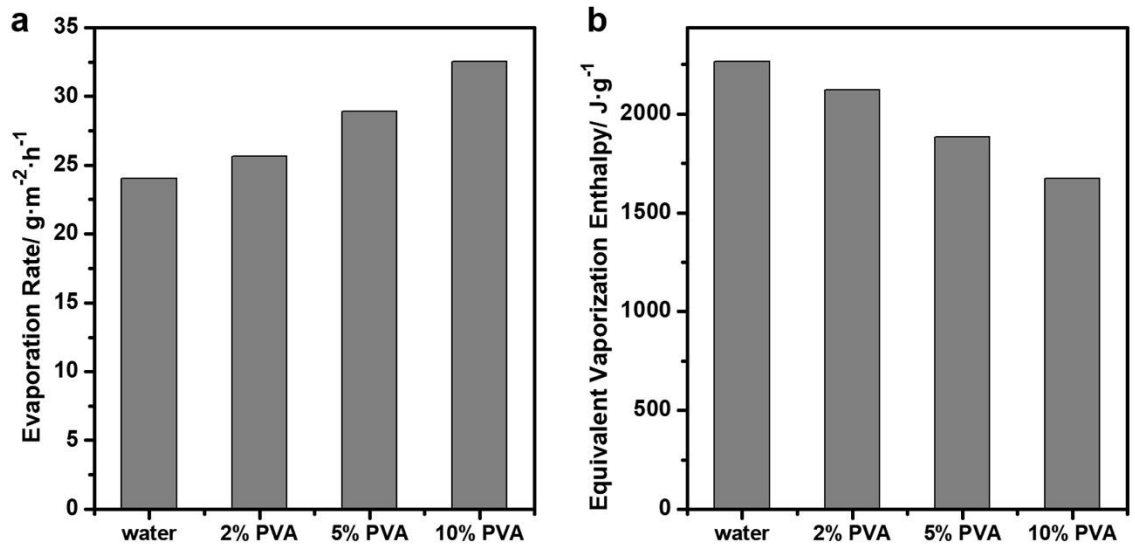


Figure 4.19 (a) Evaporation rate of water and PVA hydrogel with different PVA content. (b) Equivalent vaporization enthalpy of water in bulk water and prepared PVA hydrogels.

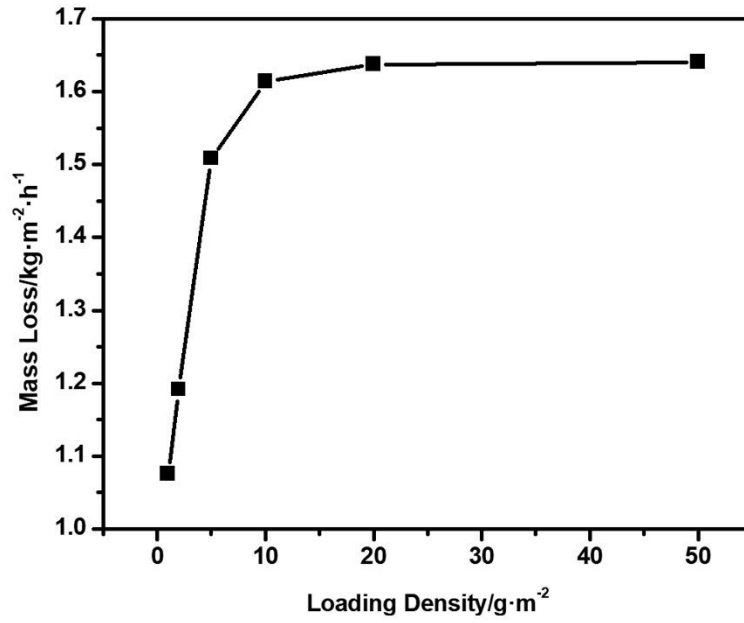


Figure 4.20 Dependence of steam generation performance on the loading density of Ni40C20.

The enhancement brought by the rough surfaces can be generally attributed to two reasons, including multiple reflections and increased active surface area. As demonstrated in Figure 4.21, on a flat surface, the light was scattered into the space above the film without being utilized. However, on a rough surface, due to the random reflection angles on different surfaces, light being scattered off one surface has a chance to be collected by another, reducing the energy loss due to the scattering of the samples. As shown in Figure 4.22, the M-40 composite film shows a slightly lower reflectance than directly deposited Ni₄₀C₂₀ particles. However, due to the low reflectance of the Ni₄₀C₂₀ sample, the benefit brought by multiple reflections should not be obvious. On the other hand, the roughness of the film surface can significantly increase the effective evaporation surface area, which is especially important in an interfacial evaporator system. This feature can only be realized by a convex textured surface because, in a typical porous material, the pores are filled with water, and the evaporation surface essentially the same as a flat surface. As evidenced by Figure 4.17f, the evaporation rate on the rough surface surpassed the flat surface at room temperature. More specifically, the evaporation rate on M-40 is three times the evaporation rate on NM-40 regardless of the same loading amount of particles and hydrogel. This phenomenon also explained our finding that M-40 had the lowest equilibrium surface temperature among all samples (Figure 4.17g). The high evaporation rate on the surface takes away the heat generated on the particles, leading to a lower average temperature. The energy loss of each sample was analyzed and summarized in Figure 4.17h. Generally, the heat loss takes place in three ways, thermal radiation of the absorber, convection between the absorber and the ambient air, and heat conduction from the surface to bulk water, all of

which are closely related to the temperature of the absorber. Thanks to the low surface temperature, the thermal radiation was much suppressed and only accounted for an energy loss of 3.0% of the input energy in M-40. In comparison, a temperature difference of 20 °C will result in an energy loss of 12.7% through radiation alone. Furthermore, the lower temperature difference between the absorber and the ambient environment also reduced the convection on the film surface. According to our calculation, the energy loss through convection only accounted for 2.2% of the input energy in M-40. The low surface temperature brought by the high evaporative rate significantly reduced the energy loss of the system, leading to a highly efficient solar evaporation system.

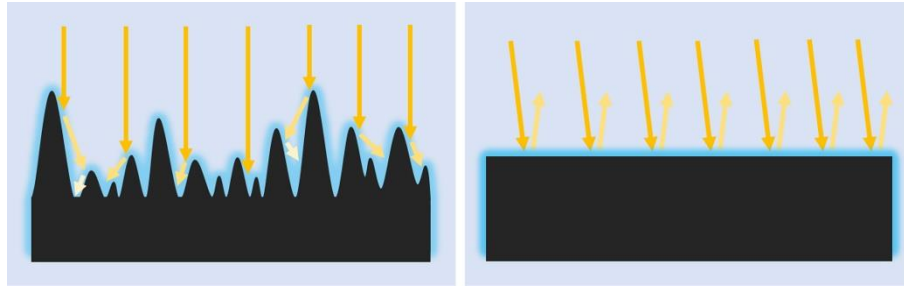


Figure 4.21 Schematic illustration of the light reflection and active surface area difference of a rough surface and a smooth surface.

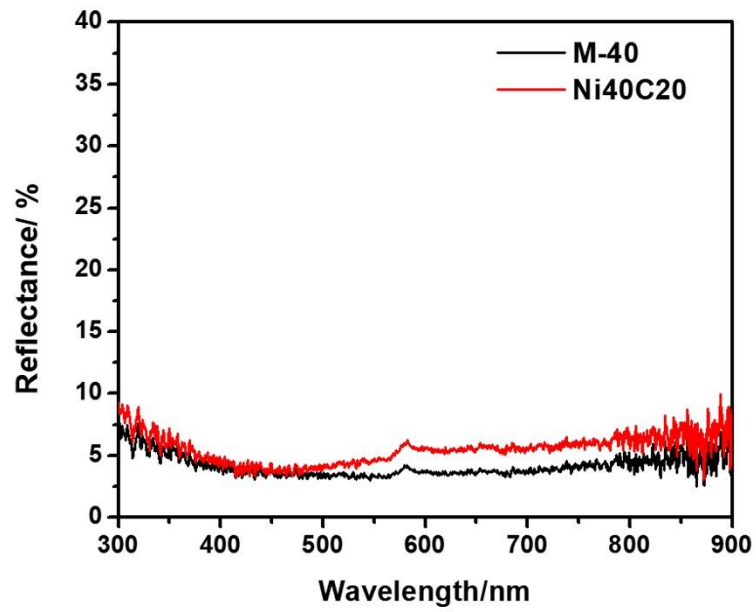


Figure 4.22 Reflectance spectra of M-40 composite film and directly deposited Ni40C20 nanoparticles.

4.4 Conclusion

In summary, we demonstrate the rational design of Ni@C@SiO₂ core-shell nanoparticles as promising light absorbers for solar-driven steam generation. The combination of the broadband absorption of carbon and plasmonic properties of Ni ensured a high energy utilization efficiency. In the meantime, the silica layer improved the robustness of the particles and provided a hydrophilic surface to facilitate the heat exchange. As a result, the core-shell particles showed superior performance, and the energy efficiency reached 91.2%. In addition to high photothermal efficiency, these nanoparticles can be incorporated into a hydrogel film so that its surface texture can be tuned by taking advantage of the magnetic response of these particles. Thanks to the increased surface roughness, the steam generation performance can be further improved by enabling multiple reflections and increasing the effective surface area, achieving an evaporation rate as high as 2.25 kg·m⁻²·h⁻¹ with a Ni40C20/PVA composite hydrogel film. The robust core-shell particles can be readily incorporated into the design of many other evaporators. More importantly, we believe that the mold-free surface texturing strategy based on magnetic particles can provide new opportunities in designing solar evaporator devices.

4.5 Reference

1. Elimelech, M.; Phillip, W. A., The Future of Seawater Desalination: Energy, Technology, and the Environment. *Science* **2011**, *333* (6043), 712.
2. Ghasemi, H.; Ni, G.; Marconnet, A. M.; Loomis, J.; Yerci, S.; Miljkovic, N.; Chen, G., Solar steam generation by heat localization. *Nature Communications* **2014**, *5* (1), 4449.
3. Zhou, J.; Gu, Y.; Liu, P.; Wang, P.; Miao, L.; Liu, J.; Wei, A.; Mu, X.; Li, J.; Zhu, J., Development and Evolution of the System Structure for Highly Efficient Solar Steam Generation from Zero to Three Dimensions. *Advanced Functional Materials* **2019**, *29* (50), 1903255.
4. Tao, P.; Ni, G.; Song, C.; Shang, W.; Wu, J.; Zhu, J.; Chen, G.; Deng, T., Solar-driven interfacial evaporation. *Nature Energy* **2018**, *3* (12), 1031-1041.
5. Wu, X.; Robson, M. E.; Phelps, J. L.; Tan, J. S.; Shao, B.; Owens, G.; Xu, H., A flexible photothermal cotton-CuS nanocage-agarose aerogel towards portable solar steam generation. *Nano Energy* **2019**, *56*, 708-715.
6. Zhang, Z.; Mu, P.; He, J.; Zhu, Z.; Sun, H.; Wei, H.; Liang, W.; Li, A., Facile and Scalable Fabrication of Surface-Modified Sponge for Efficient Solar Steam Generation. *ChemSusChem* **2019**, *12* (2), 426-433.
7. Li, X.; Xu, W.; Tang, M.; Zhou, L.; Zhu, B.; Zhu, S.; Zhu, J., Graphene oxide-based efficient and scalable solar desalination under one sun with a confined 2D water path. *Proceedings of the National Academy of Sciences* **2016**, *113* (49), 13953.
8. Guo, Y.; Zhou, X.; Zhao, F.; Bae, J.; Rosenberger, B.; Yu, G., Synergistic Energy Nanoconfinement and Water Activation in Hydrogels for Efficient Solar Water Desalination. *ACS Nano* **2019**, *13* (7), 7913-7919.
9. Wang, Y.; Wu, X.; Shao, B.; Yang, X.; Owens, G.; Xu, H., Boosting solar steam generation by structure enhanced energy management. *Science Bulletin* **2020**, *65* (16), 1380-1388.
10. Li, J.; Wang, X.; Lin, Z.; Xu, N.; Li, X.; Liang, J.; Zhao, W.; Lin, R.; Zhu, B.; Liu, G.; Zhou, L.; Zhu, S.; Zhu, J., Over 10 kg m⁻² h⁻¹ Evaporation Rate Enabled by a 3D Interconnected Porous Carbon Foam. *Joule* **2020**, *4* (4), 928-937.
11. Zhu, M.; Li, Y.; Chen, F.; Zhu, X.; Dai, J.; Li, Y.; Yang, Z.; Yan, X.; Song, J.; Wang, Y.; Hitz, E.; Luo, W.; Lu, M.; Yang, B.; Hu, L., Plasmonic Wood for High-Efficiency Solar Steam Generation. *Advanced Energy Materials* **2018**, *8* (4), 1701028.

12. Chen, J.; Li, B.; Hu, G.; Aleisa, R.; Lei, S.; Yang, F.; Liu, D.; Lyu, F.; Wang, M.; Ge, X.; Qian, F.; Zhang, Q.; Yin, Y., Integrated Evaporator for Efficient Solar-Driven Interfacial Steam Generation. *Nano Letters* **2020**.
13. Zhang, P.; Li, J.; Lv, L.; Zhao, Y.; Qu, L., Vertically Aligned Graphene Sheets Membrane for Highly Efficient Solar Thermal Generation of Clean Water. *ACS Nano* **2017**, *11* (5), 5087-5093.
14. Mu, P.; Zhang, Z.; Bai, W.; He, J.; Sun, H.; Zhu, Z.; Liang, W.; Li, A., Superwetting Monolithic Hollow-Carbon-Nanotubes Aerogels with Hierarchically Nanoporous Structure for Efficient Solar Steam Generation. *Advanced Energy Materials* **2019**, *9* (1), 1802158.
15. Yang, H.-C.; Chen, Z.; Xie, Y.; Wang, J.; Elam, J. W.; Li, W.; Darling, S. B., Chinese Ink: A Powerful Photothermal Material for Solar Steam Generation. *Advanced Materials Interfaces* **2019**, *6* (1), 1801252.
16. Fu, Y.; Wang, G.; Ming, X.; Liu, X.; Hou, B.; Mei, T.; Li, J.; Wang, J.; Wang, X., Oxygen plasma treated graphene aerogel as a solar absorber for rapid and efficient solar steam generation. *Carbon* **2018**, *130*, 250-256.
17. Hogan, N. J.; Urban, A. S.; Ayala-Orozco, C.; Pimpinelli, A.; Nordlander, P.; Halas, N. J., Nanoparticles Heat through Light Localization. *Nano Letters* **2014**, *14* (8), 4640-4645.
18. Chen, J.; Feng, J.; Li, Z.; Xu, P.; Wang, X.; Yin, W.; Wang, M.; Ge, X.; Yin, Y., Space-Confining Seeded Growth of Black Silver Nanostructures for Solar Steam Generation. *Nano Letters* **2019**, *19* (1), 400-407.
19. Zhou, L.; Tan, Y.; Wang, J.; Xu, W.; Yuan, Y.; Cai, W.; Zhu, S.; Zhu, J., 3D self-assembly of aluminium nanoparticles for plasmon-enhanced solar desalination. *Nature Photonics* **2016**, *10* (6), 393-398.
20. Zhou, L.; Tan, Y.; Ji, D.; Zhu, B.; Zhang, P.; Xu, J.; Gan, Q.; Yu, Z.; Zhu, J., Self-assembly of highly efficient, broadband plasmonic absorbers for solar steam generation. *Science Advances* **2016**, *2* (4), e1501227.
21. Halas, N. J.; Lal, S.; Chang, W.-S.; Link, S.; Nordlander, P., Plasmons in Strongly Coupled Metallic Nanostructures. *Chemical Reviews* **2011**, *111* (6), 3913-3961.
22. Kim, S.; Kim, J.-M.; Park, J.-E.; Nam, J.-M., Nonnoble-Metal-Based Plasmonic Nanomaterials: Recent Advances and Future Perspectives. *Advanced Materials* **2018**, *30* (42), 1704528.

23. Ding, D.; Liu, K.; Fan, Q.; Dong, B.; Zhang, Y.; Yin, Y.; Gao, C.; Ding, S., Nickel nanoparticles individually encapsulated in densified ceramic shells for thermally stable solar energy absorption. *Journal of Materials Chemistry A* **2019**, *7* (7), 3039-3045.
24. Halpern, A. R.; Corn, R. M., Lithographically Patterned Electrodeposition of Gold, Silver, and Nickel Nanoring Arrays with Widely Tunable Near-Infrared Plasmonic Resonances. *ACS Nano* **2013**, *7* (2), 1755-1762.
25. Shao, B.; Wang, Y.; Wu, X.; Lu, Y.; Yang, X.; Chen, G. Y.; Owens, G.; Xu, H., Stackable nickel-cobalt@polydopamine nanosheet based photothermal sponges for highly efficient solar steam generation. *Journal of Materials Chemistry A* **2020**, *8* (23), 11665-11673.
26. McAdams, W. H., *Heat transmission*. McGraw-Hill: New York, 1954.
27. Chen, J.; Feng, J.; Yang, F.; Aleisa, R.; Zhang, Q.; Yin, Y., Space-Confined Seeded Growth of Cu Nanorods with Strong Surface Plasmon Resonance for Photothermal Actuation. *Angewandte Chemie International Edition* **2019**, *58* (27), 9275-9281.
28. Bai, Y.; Yao, X.; Wang, X.; Yin, Y., Surface-Initiated Redox Route to Hollow MnO₂ Nanostructures. *ChemNanoMat* **2020**, *n/a* (n/a).
29. Sidhaye, D. S.; Bala, T.; Srinath, S.; Srikanth, H.; Poddar, P.; Sastry, M.; Prasad, B. L. V., Preparation of Nearly Monodisperse Nickel Nanoparticles by a Facile Solution Based Methodology and Their Ordered Assemblies. *The Journal of Physical Chemistry C* **2009**, *113* (9), 3426-3429.
30. Cui, Y.; Wang, Y.; Shao, Z.; Mao, A.; Gao, W.; Bai, H., Smart Sponge for Fast Liquid Absorption and Thermal Responsive Self-Squeezing. *Advanced Materials* **2020**, *32* (14), 1908249.
31. Zhao, F.; Zhou, X.; Shi, Y.; Qian, X.; Alexander, M.; Zhao, X.; Mendez, S.; Yang, R.; Qu, L.; Yu, G., Highly efficient solar vapour generation via hierarchically nanostructured gels. *Nature Nanotechnology* **2018**, *13* (6), 489-495.
32. Xu, W.; Xing, Y.; Liu, J.; Wu, H.; Cui, Y.; Li, D.; Guo, D.; Li, C.; Liu, A.; Bai, H., Efficient Water Transport and Solar Steam Generation via Radially, Hierarchically Structured Aerogels. *ACS Nano* **2019**, *13* (7), 7930-7938.
33. Zhou, X.; Zhao, F.; Guo, Y.; Rosenberger, B.; Yu, G., Architecting highly hydratable polymer networks to tune the water state for solar water purification. *Science Advances* **2019**, *5* (6), eaaw5484.

Chapter 5 Conclusion and Outlook

5.1 Conclusion of this Dissertation

The synthesis of plasmonic material has attracted a lot of research interests due to their unique optical properties. Exploring the tuning principles of the optical properties of the plasmonic nanoparticles not only deepened our understanding of light-matter interaction but brought new opportunities to novel optical applications, such as sensing, biomedicine, and solar-energy conversion. Understanding the design principles of the plasmonic nanoparticles allows us to tailor the nanostructures for specific application scenarios.

It is well known that the optical properties of plasmonic nanostructures are highly associated with their morphologies. With tremendous efforts put in the synthetic protocols, especially in the crystal growth mechanism in seed-mediated growth methods, nanoparticles with well-defined geometries can be prepared with high reproducibility. Recent researches have turned to the unconventional seed-mediated growth methods, where the facet directed epitaxial growth was avoided. The novel structures that deviated from the traditional facet guided crystal growth brought more complexity to both the morphology and the optical properties. In Chapter 2, we demonstrated the optical tuning of plasmonic nanoparticles through morphology control, more specifically, site-selective island growth on anisotropic Au nanostructures. Although the synthesis of similar structures has been reported before, we established a surface strain template that offers the systematic tuning of the structural features of the islands, including the number, size, distance, wetting degree of islands grown on the Au nanostructures. Using Au nanorods as

an example system, we established a relationship between the optical properties and the structural features of the products and achieved a multi-stage fine-tuning of the longitudinal LSPR peak of the Au nanodumbbells obtained from the tip island growth. The Au nanodumbbells exhibited an LSPR peak in the NIR-II window for photothermal treatments while maintaining a relatively small size, which was difficult to achieve in a typical Au nanorod case. The fine-tuning of the LSPR peak shown in this work marked an important step of the Au nanodumbbells for practical applications.

In addition to the permanent change in optical properties, the dynamic and reversible control can bring more flexibility in optical tuning and is important for the fabrication of responsive materials and smart devices. Magnetic manipulation of the plasmonic nanostructures proved to be an ideal approach to achieve dynamic optical tuning, as it offers large scale, contactless control without interfering with the surrounding media, all of which are important in the design and fabrication of smart devices. In Chapter 3, we demonstrated two magnetic tuning strategies that approached the synthesis of plasmonic/magnetic composites from two directions, building plasmonic nanostructures based on the magnetic nanoparticles and coating magnetic materials on plasmonic nanoparticles. In the first part, we utilized the self-aligned nature of Au-Au and Au-Ag dimers synthesized with partial surface passivation method and fabricated $\text{Fe}_3\text{O}_4@\text{SiO}_2/\text{Au-Au}$ and $\text{Fe}_3\text{O}_4@\text{SiO}_2/\text{Au-Ag}$ nanocomposites with Au-Au and Au-Ag dimers aligned perpendicular to the surface of $\text{Fe}_3\text{O}_4@\text{SiO}_2$ nanorods. This allowed us to achieve a large-scale oriental control of the plasmonic dimers and selective elimination of the longitudinal mode of the dimers. Taking advantage of the lithography methods, we

fabricated patterned nanocomposite/solvogel film with nanocomposites aligned in different regions and showed the polarization-dependent color-switching that can be used for anti-counterfeiting purposes. In the second part, we attempted the direct coating of Fe_3O_4 on Au and Ag nanostructures. This strategy provides a more straightforward way to achieve magnetic manipulation of plasmonic nanostructures and potentially broaden the choice of plasmonic nanoparticles to any pre-synthesized particles. Due to the lattice mismatch between Au and Fe_3O_4 , Fe_3O_4 has a tenancy to self-nucleate instead of coating on Au surface. Taking advantage of our previously reported synthetic strategy of CNCs, which consisted of ultra-fine Fe_3O_4 nanocrystals, we successfully coat the Au and Ag nanostructure with Fe_3O_4 . Although AuNPs tend to form assemblies during the Fe_3O_4 coating, it can be avoided by using microstructures, such as AgNWs and AgPLTs. We also demonstrated the magnetic manipulation of $\text{Ag}@Fe_3O_4$ PLTs and the fabrication of a smart window and a smart display device featuring magnetically controlled transmission and reflection, respectively.

In Chapter 4, we further explored the alternative plasmonic nanomaterials and demonstrated that Ni could be a promising candidate for solar energy harvesting. Ni intrinsically exhibits a relatively broad plasmonic peak at about 500 nm. By combining a layer of carbon coating, the plasmonic peak of NiNPs can be redshifted to better match the solar radiation spectrum, while carbon itself allows the absorption in longer wavelengths. The $\text{Ni}@C@SiO_2$ core-shell nanocomposites showed excellent solar-thermal performance and proved to be efficient light absorbers in solar-steam-generation devices. In addition, the magnetic properties of Ni gave the nanocomposites magnetic responses, which, when

incorporated in a PVA hydrogel film, can produce surface microstructure on the surface of the films. The microstructures greatly enhanced the evaporation of water on the device surface and proposed new possibilities in the design of solar-evaporator devices.

5.2 Outlook and Future Work

There is still room for the optical tuning of the plasmonic nanoparticles. In this section, we proposed future research directions in several aspects.

First, as shown in Chapter 2, the site-selective island growth of Au can occur on Au nanostructures capped with CTAB or CTAC. As observed in the site-selective island growth on nanostructures other than AuNRs, islands can sometimes be grown on the edges of the nanostructures. As the edges have a different surface property from both the faces and the tips, the site selectivity between the three regions should be explored, and more complex feature selecting principles should be involved to obtain a finer control of the island growth locations.

In the second part of Chapter 3, the Au assemblies fixed by the Fe₃O₄ nanocrystals could be a promising platform for SERS enhancement for dried samples. Drying samples is a common method to enhance the SERS signal of analytes. However, due to the uneven distribution of solutes during the drying process, the SERS signal of dried samples has a relatively low reproducibility, limiting the quantitative analysis of the samples. The hot spots within the Au assemblies can greatly enhance the SERS signal, and Fe₃O₄ fixation improves the structural stability during the drying process. By magnetically separating the Au@Fe₃O₄ nanocomposites in the droplets, the nanocomposites can serve as a nucleation site for the analytes, and the analytes can be enriched around the composites. This not only

improves the reproducibility of the SERS analysis but ensures the enrichment of analytes around the plasmonic nanoparticles, further enhancing the SERS signals.

In a word, there's still plenty of room at the bottom. We look forward to exploring the beauty of the nano-world and contributing more to the development of nanotechnology.